

EDITORIAL BOARD

Editor-in-Chief

I.V. Krivtsun E.O. Paton Electric Welding Institute, Kyiv, Ukraine

Deputy Editor-in-Chief

S.V. Akhonin E.O. Paton Electric Welding Institute, Kyiv, Ukraine

Deputy Editor-in-Chief

L.M. Lobanov E.O. Paton Electric Welding Institute, Kyiv, Ukraine

Editorial Board Members

O.M. Berdnikova E.O. Paton Electric Welding Institute, Kyiv, Ukraine
Chang Yunlong School of Materials Science and Engineering, Shenyang University of Technology, Shenyang, China
V.V. Dmitrik NTUU «Kharkiv Polytechnic Institute», Kharkiv, Ukraine
Dong Chunlin China-Ukraine Institute of Welding of Guangdong Academy of Sciences, Guangzhou, China
M. Gasik Aalto University Foundation, Finland
A. Gumenyuk Bundesanstalt für Materialforschung und –prüfung (BAM), Berlin, Germany
V.V. Knysh E.O. Paton Electric Welding Institute, Kyiv, Ukraine
V.M. Korzhyk E.O. Paton Electric Welding Institute, Kyiv, Ukraine
V.V. Kvasnytskyi NTUU «Igor Sikorsky Kyiv Polytechnic Institute», Kyiv, Ukraine
Yu.M. Lankin E.O. Paton Electric Welding Institute, Kyiv, Ukraine
S.Yu. Maksymov E.O. Paton Electric Welding Institute, Kyiv, Ukraine
Yupiter HP Manurung Smart Manufacturing Research Institute, Universiti Teknologi MARA, Shah Alam, Malaysia
M.O. Pashchin E.O. Paton Electric Welding Institute, Kyiv, Ukraine
Ya. Pilarczyk Welding Institute, Gliwice, Poland
V.D. Poznyakov E.O. Paton Electric Welding Institute, Kyiv, Ukraine
U. Reisingen Welding and Joining Institute, Aachen, Germany
I.O. Ryabtsev E.O. Paton Electric Welding Institute, Kyiv, Ukraine
V.M. Uchanin Karpenko Physico-Mechanical Institute, Lviv, Ukraine
Yang Yongqiang South China University of Technology, Guangzhou, China

Managing Editor

O.T. Zelnichenko International Association «Welding», Kyiv, Ukraine

Address of Editorial Board

E.O. Paton Electric Welding Institute, 11 Kazymyr Malevych Str. (former Bozhenko), 03150, Kyiv, Ukraine
Tel./Fax: (38044) 205 23 90, E-mail: journal@paton.kiev.ua
<https://patonpublishinghouse.com/eng/journals/tpwj>

State Registration Certificate 24933-14873 ПП from 13.08.2021

ISSN 0957-798X, DOI: <http://dx.doi.org/10.37434/tpwj>

Subscriptions, 12 issues per year:

\$384 — annual subscription for the printed (hard copy) version, air postage and packaging included;

\$312 — annual subscription for the electronic version (sending issues in pdf format or providing access to IP addresses).

Representative Office of «The Paton Welding Journal» in China:

China-Ukraine Institute of Welding, Guangdong Academy of Sciences
Address: Room 210, No. 363 Changxing Road, Tianhe, Guangzhou, 510650, China.
Zhang Yupeng, Tel: +86-20-61086791, E-mail: patonjournal@gwi.gd.cn

The content of the journal includes articles received from authors from around the world in the field of welding, metallurgy, material science and selectively includes translations into English of articles from the following journals, published by PWI in Ukrainian:

- Automatic Welding (<https://patonpublishinghouse.com/eng/journals/as>);
- Technical Diagnostics & Nondestructive Testing (<https://patonpublishinghouse.com/eng/journals/tdnk>);
- Electrometallurgy Today (<https://patonpublishinghouse.com/eng/journals/sem>).

CONTENTS

ORIGINAL ARTICLES

L.M. Lobanov, V.M. Korzhyk, M.O. Pashchyn, O.L. Mikhodui, A.A. Grynyuk, E.V. Ilyashenko, P.V. Goncharov, P.R. Ustymenko DEFORMATION-FREE TIG WELDING OF AMg6 ALLOY WITH APPLICATION OF ELECTRODYNAMIC TREATMENT OF WELD METAL*	3
V.Yu. Skulskyi, M.O. Nimko, A.R. Gavryk, I.G. Osypenko, O.V. Vavilov, O.G. Kantor, L.P. Rubashka PECULIARITIES OF WELDING COMBINED JOINTS OF 15Kh2M2FBS (P3) AND X10CrMoVNb91 (P91) STEELS*	9
O.P. Voronchuk, O.P. Zhudra, T.V. Kaida, O. V. Petrov, L.M. Kapitanchuk, I.L. Bogaichuk INFLUENCE OF THE COMPOSITION OF CHARGE COMPONENTS OF FLUX-CORED STRIPS OF C-Fe-Cr-Nb ALLOYING SYSTEM ON CHEMICAL COMPOSITION AND STRUCTURE OF THE DEPOSITED METAL*	18
Yu.S. Borysov, A.L. Borysova, O.P. Gryshchenko, T.V. Tsymbalista, M.A. Vasylykivska INVESTIGATION OF HEAT RESISTANCE OF PLASMA COATINGS FROM TiAl INTERMETALLIC WITH APPLICATION OF PARAMETRIC OXIDATION DIAGRAM*	25
O.M. Sabadash, S.V. Maksymova REACTIVE-FLUX BRAZING OF ALUMINIUM TO TITANIUM*	32
K.Yu. Yakovchuk, G.P. Myalnytsya, A.V. Mykytchyk, Yu.E. Rudoy, R.O. Tkach DEVELOPMENT OF THE CoCrAlY/ZrO ₂ -8 % Y ₂ O ₃ TYPE THERMAL BARRIER COATING BY SURFACE DOPING OF THE METAL LAYER WITH ALUMINIUM**	39
O.V. Makhnenko, S.M. Kandala EVALUATION OF BRITTLE FRACTURE RESISTANCE OF WWER-1000 REACTOR BAFFLE DURING LONG-TERM SERVICE, TAKING INTO ACCOUNT THE RESIDUAL TECHNOLOGICAL STRESSES***	46
INFORMATION	
DESIGN AND REPAIR OF VERTICAL CYLINDRICAL ABOVE GROUND WELDED STEEL TANKS	55

*Translated Article(s) from «Automatic Welding», No. 8, 2022.

**Translated Article(s) from «Electrometallurgy Today», No. 3, 2022.

***Translated Article(s) from «Technical Diagnostics & Nondestructive Testing», No. 3, 2022.

DOI: <https://doi.org/10.37434/tpwj2022.08.01>

DEFORMATION-FREE TIG WELDING OF AMg6 ALLOY WITH APPLICATION OF ELECTRODYNAMIC TREATMENT OF WELD METAL

L.M. Lobanov¹, V.M. Korzhyk¹, M.O. Pashchyn¹, O.L. Mikhodui¹, A.A. Grynyuk¹, E.V. Ilyashenko¹, P.V. Goncharov¹, P.R. Ustymenko²

¹E.O. Paton Electric Welding Institute of the NASU
11 Kazymyr Malevych Str., 03150, Kyiv, Ukraine

²National Technical University of Ukraine «Igor Sikorsky Kyiv Polytechnic Institute»
37 Peremohy Prosp., 03056, Kyiv, Ukraine

ABSTRACT

Application of electrodynamic treatment (EDT), taking into account the welding process peculiarities, is a new trend in engineering practice, enhancing the process capabilities. At the same time, a necessary condition for realization of fusion welding process, is heating of the weld metal with its further cooling to room temperature. Realization of EDT technology during welding promotes more intensive relaxation of welding stresses as a result of EDT, compared to weld metal treatment at room temperature. Proceeding from investigation results, it was found that EDT of butt welded joint samples leads to transition of residual tensile welding stresses into compressive stresses. Experimental verification of the residual stress-strain state with application of the method of electron speckle interferometry confirmed the results of mathematical modeling, namely lowering of tensile stresses and increase of compressive stresses in the weld after EDT at temperature $T = 150$ °C, compared to EDT at $T = 20$ °C. It was proved that EDT of samples of butt joints from AMg6 alloy during TIG welding improves their production accuracy that is characterized by lowering of the level of their residual longitudinal distortion, compared to postweld EDT.

KEYWORDS: electrodynamic treatment, electrode device, residual welding stresses, aluminium alloy, electric current pulse, impact interaction, indenter-electrode, membrane stresses, nonconsumable electrode welding

INTRODUCTION

Residual welding stresses have a negative impact on the fatigue life, corrosion resistance and residual deformations of sheet structures from aluminium-based alloys. In recent years, growth in fabrication of such structures is observed in the world practice so that the problem of reduction of residual tensile stresses becomes particularly urgent. Traditional methods of optimization of the residual stressed states, which involve application of metal-intensive equipment and (or) considerable energy consumption, do not meet the requirements of modern engineering practice [1, 2].

Development of high-technology industries stimulates introduction of energy-saving technologies of deformation-free welding of aluminium-based alloys. Application of pulsed electromagnetic fields (PEMF) for optimization of residual stress-strain states and mechanical characteristics of welded joints is the current trend in modern practice of replacement of the traditional metal processing technologies by advanced and energy-efficient methods [3, 4].

RESEARCH RELEVANCE

One of the novel approaches to optimization of the residual stressed states of sheet structures is electrodynamic treatment (EDT) of welded joints, which is based on electroplasticity effect (EPE) which arises at

passage of electric current pulses (ECP) of more than 1 kA/mm^2 density through the item metal [5–7]. EPE impact results in appearance of plastic deformations in the metal, initiating the mechanisms of relaxation of residual welding stresses.

In works [8, 9] it was proved that accompanying heating of the zone of electric pulse impact promotes relaxation of tensile stresses. It stimulates investigations of new EDT capabilities, one of which is its application during fusion welding.

It should be noted that no assessment of the influence of thermal cycle of welding on the features of residual stressed state regulation under EDT impact has not been performed up to now.

In view of the above-said, the objective of the work is development of scientific fundamentals of welding technology with EDT application for regulation of the residual stress-strain states of aluminium alloy welded joints.

Considering the data of work [9], it can be noted that EDT under the conditions of weld metal heating is more effective (compared to EDT without heating) for lowering of residual stresses in aluminium alloy welded plates. Here, as noted above, the source of such heating can be the heat of the cooling welded joint.

Hardware support of the method is reduced to organizing synchronous movement of the welding torch

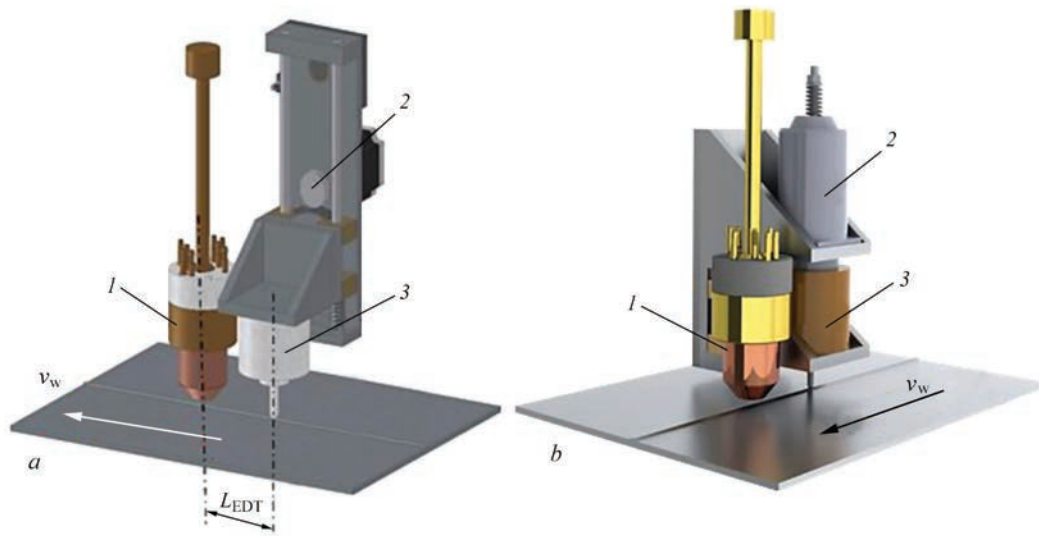


Figure 1. Variants of design schemes of EDT during welding with monoblock layout of the end effectors: *a* — EDT ED pressing to the weld metal with application of eccentric 2; *b* — EDT ED pressing to the weld metal with application of linear displacement solenoid 2 (v_w — welding direction; 1 — WT; 3 — EDT ED)

(WT) and electrode device for EDT (EDT ED) that are designed as a monoblock with a device recording their relative position. Figure 1 shows the design variants of portal type schemes of EDT ED and WT with monoblock layout. Design variants of electrode movement ensure reliable electric contact of the electrode with weld metal at the moment of electrodynamic impact. Contact interaction of EDT ED with the weld metal can be performed on the base of a mechanical drive, using an eccentric (Figure 1, *a*) or electric drive, using linear displacement solenoid (Figure 1, *b*). Each of the schemes in Figure 1 has its advantages and disadvantages, discussion of which goes beyond the scope of this work.

Application of these schemes allows ensuring optimum distance L_{EDT} between EDT ED and WT. The monoblock includes EDT ED — 3 and WT — 1,



Figure 2. Hardware complex for automatic TIG welding which is compatible with weld EDT: 1 — system for filler wire feeding; 2 — welding torch; 3 — electrode device; 4 — linear displacement solenoid of EDT electrode

which are installed along the welded joint at distance L_{EDT} between 1 and 3 (Figure 1, *a*). Value L_{EDT} sets the heating temperature T_{EDT} of treatment zone under the conditions of impact of thermal cycle of welding. Power networks for welding and EDT are formed independently one from the other.

Searching for optimal EDT mode under the welding conditions involves experimental evaluation of the electrophysical and mechanical characteristics of the treated material. An alternative solution of the problem is mathematical modeling of EDT process, which allows assessment of the evolution of stress-strain states of the welded joints as a result of EDT. In keeping with modeling results, optimal T_{EDT} value at EDT of AMg6 alloy is 150 °C [10–13].

PROCEDURE AND RESULTS OF EXPERIMENTAL STUDIES OF THE INFLUENCE OF WELDING THERMAL CYCLE ON THE RESIDUAL STRESS-STRAIN STATES

A hardware complex for automatic TIG welding of aluminium alloys, which is compatible with EDT process, was made for implementation of the technology of EDT during welding (Figure 2). The complex components are designed as a monoblock.

In order to assess the effectiveness of EDT during welding, the method of electron speckle-interferometry was used [14] to conduct comparative studies of residual stress-strain states of welded joints from AMg61 alloy made with EDT application after and during welding, i.e. at T values of 20 and 150 °C, respectively. Experimental evaluation of the longitudinal (along the weld line) component σ_x (Figure 3, *a*) of residual welding stresses and deflections f_x of lon-

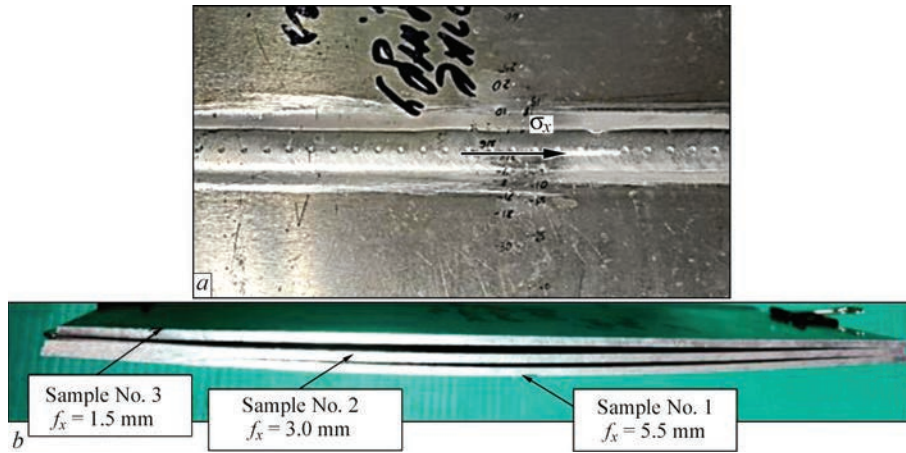


Figure 3. Appearance of samples Nos 1–3: *a* — sample No.2; where EDT point zones are located on the weld; arrow shows the direction of action of stress component σ_x ; *b* — longitudinal deflections f_x of the edge of samples Nos 1–3

Table 1. Mode of TIG welding of welded joint sample from AMg61

Arc voltage U_{arc} , V	Arc current I_{arc} , A	Welding speed v_w , mm/s	Wire feed rate v_f , mm/s	Argon flow rate v_{Ar} , l/min	Filler wire diameter d , mm
16.2	160	3.3	23.3	15	1.2

gitudinal edges of the samples was performed using calipers and planed ruler [5].

Samples of butt welded joints from AMg61 alloy plates of $450 \times 200 \times 3$ mm size were prepared, in order to study the thermal impact of EDT (Figure 3). Samples were welded from two plates of $450 \times 100 \times 3$ mm size by TIG process in argon in the mode given in Table 1, under the conditions of resting on a rigid foundation. Wire of ER5356 grade was used as filler material.

Sample No. 1 was produced without EDT application. Sample No. 2 (Figure 3, *a*) was welded without treatment and was subjected to EDT after welding at $T = 20$ °C. On sample No. 3 EDT was performed during welding at $T = 150$ °C. EDT of samples 2 and 3 was performed at similar values of treatment mode parameters that ensures the energy of single electrodynamic action at the level of 1 kJ.

Depth h of point zone (pits) of EDT impact and weld reinforcement height were equal to 0.2 and 0.6 mm, respectively. Thus, depth h of the pits was not higher than weld reinforcement height, i.e. it did not reduce the area of welded joint working section. It causes a negative impact of the pits on the mechanical characteristics of welded joints [5, 6]. Distance between the point zones of EDT action was 5.0 mm (Figure 3, *a*).

Figure 3, *b* shows the comparison of residual deflections f_x of longitudinal edges of samples Nos 1–3. One can see that EDT after and during welding reduces f_x value 1.8 and 3.7 times, respectively. This fact can be explained both by relaxation of residual stresses as a result of EDT, and by “rigid” fixation of

the plates. It eliminated their vertical displacement during welding and promoted formation of residual tensile plastic deformations in the weld. Interaction of the latter with residual compressive deformations from welding resulted in reduction of deflections f_x .

Figures 4–6 give the distributions of residual stresses σ_x in samples Nos 1–3, which are characterized by some common features. So, in the initial state, σ_x values in the weld center are smaller than on the outer side of the plate (curve 1 — top), compared with the sample reverse side (curve 3 — bottom). This is attributable to more intensive heat removal from the open outer surface of the sample, compared to the reverse surface, which contacts the absolutely rigid base — the welding table, which is the heat shield. Half-width of the zone of peak values of residual tensile σ_x in samples Nos 1–3 did not exceed 15 mm. Considering the fact that EDT was performed along the weld center in all the experiments, further com-

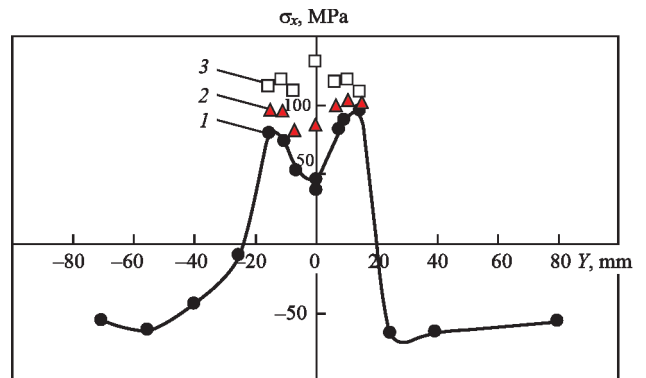


Figure 4. Distribution of stresses σ_x in the central cross-section of sample No. 1: curve 1 — top; 2 — membrane stresses; 3 — bottom

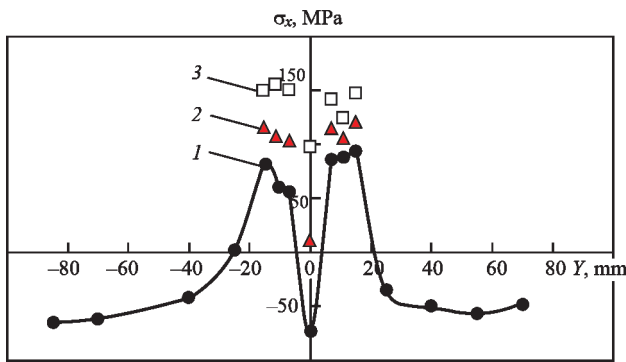


Figure 5. Distribution of stresses σ_x in the central cross-section of sample No. 2: curve 1 — top; 2 — membrane stresses; 3 — bottom

parative evaluation of the stressed states of the treated zone was performed in the samples.

In the initial state tensile σ_x values in the weld center in sample No.1 reached 50 and 130 MPa, respectively, on the outer (curve 1 — top) and reverse (curve 3 — bottom) sides of the plate (Figure 4). Evaluation of membrane stresses $\langle \sigma_x \rangle$ was performed without allowing for the out-of-plane bending component (curve 2). Values $\langle \sigma_x \rangle$ were calculated as an average between experimentally determined σ_x on curves 1 and 2. Values $\langle \sigma_x \rangle$ in the weld center were not higher than 90 MPa.

After EDT at $T = 20^\circ\text{C}$, σ_x values in the center of the weld of sample No. 2 reached -75 and 100 MPa, respectively on the outer (curve 1 — top) and reverse (curve 3 — bottom) sides of the plate (Figure 5). Thus, after EDT tensile stresses σ_x in the contact zone were transformed into compressive stresses, but on the plate reverse side tensile stresses σ_x decreased by 20 %. Tensile membrane stresses $\langle \sigma_x \rangle$ in the weld center did not exceed 12 MPa, i.e. they decreased to 90 %. Analyzing the data in Figure 5, one can see that EDT at $T = 20^\circ\text{C}$ has a dominant influence on the stressed state of the plate contact surface and a much weaker one — on σ_x values on the reverse side of sample No. 2.

After EDT at $T = 150^\circ\text{C}$, σ_x values in the center of the weld of sample No. 2 reached -100 and 10 MPa, respectively on the outer (curve 1 — top) and reverse (curve 3 — bottom) sides of the plate. Thus, after EDT tensile σ_x stresses in the contact zone transformed into compressive stresses, and on the reverse side tensile σ_x decreased by more than 90 %. Compressive membrane

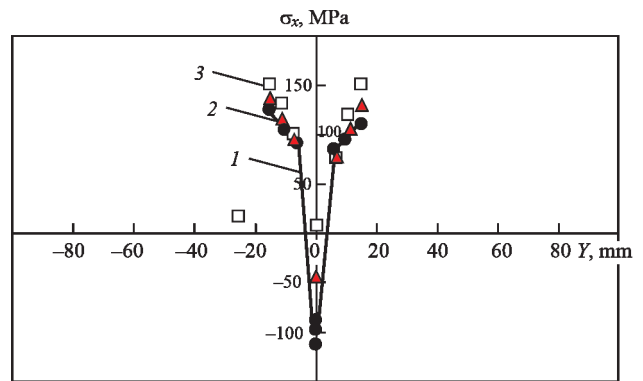


Figure 6. Distribution of stresses σ_x in the central cross-section of sample No. 3: curve 1 — top; 2 — membrane stresses; 3 — bottom

stresses $\langle \sigma_x \rangle$ in the weld center reached -50 MPa, i.e. after EDT they changed their sign. Analyzing the data in Figure 6, one can see that EDT at $T = 150^\circ\text{C}$ makes a significant influence on the stressed state of the contact and reverse surfaces of sample No. 3.

Results of modeling [10] and experimental studies of residual stresses σ_x in samples Nos 1–3 are generalized in the comparative Table 2. It should be noted that in terms of quality the experimental data confirm the results of mathematical modeling of the residual states of plates from AMg61 alloy after EDT at temperatures $T = 20$ and 150°C .

Experimental results of assessment of stresses σ_x in sample No.1 (row 1) with those of samples No. 2 (row 2) and No. 3 (row 4) were compared. Note that EDT promotes transition of tensile stresses into compressive stresses in the contact zone, and thermal impact promotes increase of σ_x values.

EDT at $T = 20^\circ\text{C}$ promotes transformation of tensile stresses σ_x in the contact zone into compressive stresses (column 3), which is visible at comparison of rows 1 and 2. Thermal influence intensifies the relaxation mechanisms, activated by EDT that promotes formation of greater values of compressive stresses σ_x (comparison of rows 2 and 4).

EDT at $T = 20^\circ\text{C}$ promotes lowering of tensile stresses of AMg61 near the rigid base (column 4) which can be seen from comparison of rows 1 and 2. Thermal impact intensifies the relaxation mechanisms activated by EDT (comparison of rows 2 and 4).

Table 2. Results of experimental studies of residual welding stresses σ_x in samples Nos 1–3

Number	Sample characteristic		σ_x , MPa, top	σ_x , MPa, bottom	$\langle \sigma_x \rangle$, MPa
1	2		3	4	5
1	Sample No. 1 without EDT	Experiment (Figure 4)	50	130	90
2	Sample No. 2	Experiment (Figure 5)	-75	100	12
3	EDT at $T = 20^\circ\text{C}$	Modeling	-132	-109	-156
4	Sample No. 3	Experiment (Figure 6)	-100	10	-45
5	EDT at $T = 150^\circ\text{C}$	Modeling	-142	-127	-155

At the respective comparison of rows 2 and 3 and 4 and 5 one can see that modeling yields greater values of stresses after EDT than does the experiment. This is attributable to ignoring (at modeling) the convective heat removal from the sample surfaces which may lower the characteristics of accompanying heating of the plates that promotes reduction (relative to calculated values) of EDT effectiveness. In the contact zone (column 3) calculated σ_x are 1.4–1.7 times higher than the experimental values. It is true for both the calculated and experimental compressive σ_x values. While at modeling the thermal impact increases the compressive σ_x values up to 8 % (comparison of rows 3 and 5), in the experiment it is up to 30 % (rows 2 and 4) at smaller absolute values of the latter.

The nature of σ_x distribution near the plate resting on the rigid base (column 4) is different. While in the experiments σ_x stresses after EDT are tensile (rows 2 and 4), in the calculation they are compressive (rows 3 and 5). Therefore, based on comparison of the experimental data, the effectiveness of EDT as a method of controlling σ_x on the reverse side is lower — bottom, compared to the outer side — top. However, the influence of the thermal impact on the Bottom side increases essentially, which leads to lowering of tensile σ_x values by 70 % after EDT at $T = 150$ °C, compared to $T = 20$ °C (comparison of rows 4 and 2, respectively).

Thus, essential lowering of $\langle \sigma_x \rangle$ (column 5) under the impact of heating is determined by relaxation of stresses near the rigid base — bottom (comparison of rows 2 and 4). At modeling σ_x lowering is only up to 16 % (comparison of rows 3 and 5), which is explained by ignoring the convective heat removal which was proved above.

Considering the results in Figures 4–6 and Table 2 one can conclude that the thermal impact, accompanying EDT, is an effective regulator of the influence on stressed-strained states of welded joints from aluminium-based alloys with the purpose of their optimization.

Residual compressive stresses decelerate propagation of fatigue fracture of welded joint metal [5, 6]. Proceeding from the above data, EDT during welding should be regarded as a promising method to optimize the stress-strain states and increase the accuracy of sheet welded structures from aluminium alloys. This technology can be used under industrial conditions for deformation-free welding of thin-walled shell and panel structures in aerospace engineering, where stringent requirements are traditionally made of their aerodynamic characteristics and stressed states. EDT application during welding will promote shortening of the time of item manufacturing and extension of their life.

CONCLUSIONS

1. It was proved that application of electrodynamic treatment (EDT) of weld metal which is performed as one process in synchronism with arc welding, is more effective, compared to separate EDT after welding, which is expressed in a more optimal residual stress-strain state of the finished welded joint.

2. Experimental check of the residual stress-strain state with application of the method of electron speckle-interferometry confirmed the results of mathematical modeling, namely lowering of the tensile stresses and increase of compressive stresses in the weld after EDT at temperature $T = 150$ °C, compared to EDT at $T = 20$ °C.

3. It was proved that EDT of butt joint samples from AMg61 alloy during welding improves their manufacturing accuracy which is characterized by lowering of the level of their residual longitudinal distortion, compared to EDT after welding.

4. It was found that EDT of butt joint samples from AMg6 (1561) alloy during nonconsumable electrode arc welding promotes optimization of their stressed states, which is characterized by lowering of residual tensile welding stresses in the weld up to 70 %, compared to EDT after welding.

REFERENCES

- Madi, Y., Besson, J. (2014) *Effect of residual stresses on brittle fracture*. Mat. ECRS-9. UTT, Troyes, France.
- Masubuchi, K. (1980) *Analysis of welded structures*. Pergamon Press, Oxford, United Kingdom.
- Shao, Quan, Kang, Jiajie, Xing, Zhiguo et al. (2019) Effect of pulsed magnetic field treatment on the residual stress of 20Cr₂Ni₄A steel. *J. of Magnetism and Magnetic Materials*, **476**, 218–224.
- Stepanov, G.V., Babutskii, A.I., Mameev, I.A., et al. (2011) Redistribution of residual welding stresses in pulsed electro-magnetic treatment. *Strength of Materials*, **43**(3), 326–331. DOI: <https://doi.org/10.1007/s11223-011-9300-2>
- Lobanov, L.M., Pashchyn, N.A., Kondratenko, I.P. et al. (2018) Development of post-weld electrodynamic treatment using electric current pulses for control of stress-strain states and improvement of life of welded structures. *Mater. Performance and Characterization*, **7**, 4. DOI: <https://doi.org/10.1520/MPC20170092>
- Lobanov, L.M., Pashchyn, M.O., Tymoshenko, O.M. et al. (2020) Increase in the life of welded joints of AMg6 aluminium alloy. *The Paton Welding J.*, **4**, 2–8. DOI: <https://doi.org/10.37434/as2020.04.01>
- Conrad, H., Sprecher, A. (1989) *The electroplastic effect in metals*. Elsevier Sci. Publishers B.V., Dislocations in Solids Ed. by F.R.N. Nabarro.
- Stepanov, G.V., Babutskii, A.I., Mameev, I.A. (2004) High-density pulse current-induced unsteady stress-strain state in a long rod. *Strength of Materials*, **36**, 377–381. DOI: <https://doi.org/10.1023/B:STOM.0000041538.10830.34>
- Lobanov, L.M., Pashchyn, M.O., Mikhodui, O.L. et al. (2022) Electrodynamic treatment of welded joints of aluminium AMg6 alloy in the process of heating the weld metal. *The Paton Welding J.*, **4**, 3–7. DOI: <https://doi.org/10.37434/as2022.04.01>

10. Lobanov, L.M., Pashchyn, M.O., Mikhodui, O.L., Sydorenko, Yu.M. (2017) Effect of the indenting electrode impact on the stress-strain state of an AMg6 alloy on electrodynamic treatment. *Strength of Materials*, 49(3), 369–380. DOI: <https://doi.org/10.1007/s11223-017-9877-1>
11. Sydorenko, Y.M., Pashchyn, M.O., Mikhodui, O.L. et al. (2020) Effect of pulse current on residual stresses in AMg6 aluminum alloy in electrodynamic treatment. *Strength of Materials*, 52(5), 731–737. DOI: <https://10.1007/s11223-020-00226-2>
12. Lobanov, L.M., Pashchyn, M.O., Mikhodui, O.L., Sydorenko Yu.M. (2018) Electric pulse component effect on the stress state of AMg6 aluminum alloy welded joints under electrodynamic treatment. *Strength of Materials*, 50(2), 246–253. DOI: <https://10.1007/s11223-017-9862-8>
13. Lobanov, L.M., Pashchyn, M.O., Mikhodui, O.L., Sydorenko Yu.M. (2022) Calculated evaluation of stress-strain states of welded joints of aluminium AMg61 alloy under the action of electrodynamic treatment of weld metal in the process of fusion welding. *The Paton Welding J.*, 7, 3–8. DOI: <https://doi.org/10.37434/as2022.07.01>
14. Lobanov, L.M., Pashchyn, M.O., Mikhoduj, O.L., Khokhlova, J.A. (2016) Investigation of residual stresses in welded joints of heat-resistant magnesium alloy ML10 after electrodynamic treatment. *J. of Magnesium and Alloys*, 4(2), 77–82. DOI: <https://10.1016/j.jma.2016.04.005>

ORCID

L.M. Lobanov: 0000-0001-9296-2335,
V.M. Korzhyk: 0000-0001-9106-8593,
M.O. Pashchyn: 0000-0002-2201-5137,
O.L. Mikhodui: 0000-0001-6660-7540,
E.V. Ilyashenko: 0000-0001-9876-0320

CONFLICT OF INTEREST

The Authors declare no conflict of interest

CORRESPONDING AUTHOR

M.O. Pashchyn
E.O. Paton Electric Welding Institute of the NASU
11 Kazymyr Malevych Str., 03150, Kyiv, Ukraine.
E-mail: svarka2000@ukr.net

SUGGESTED CITATION

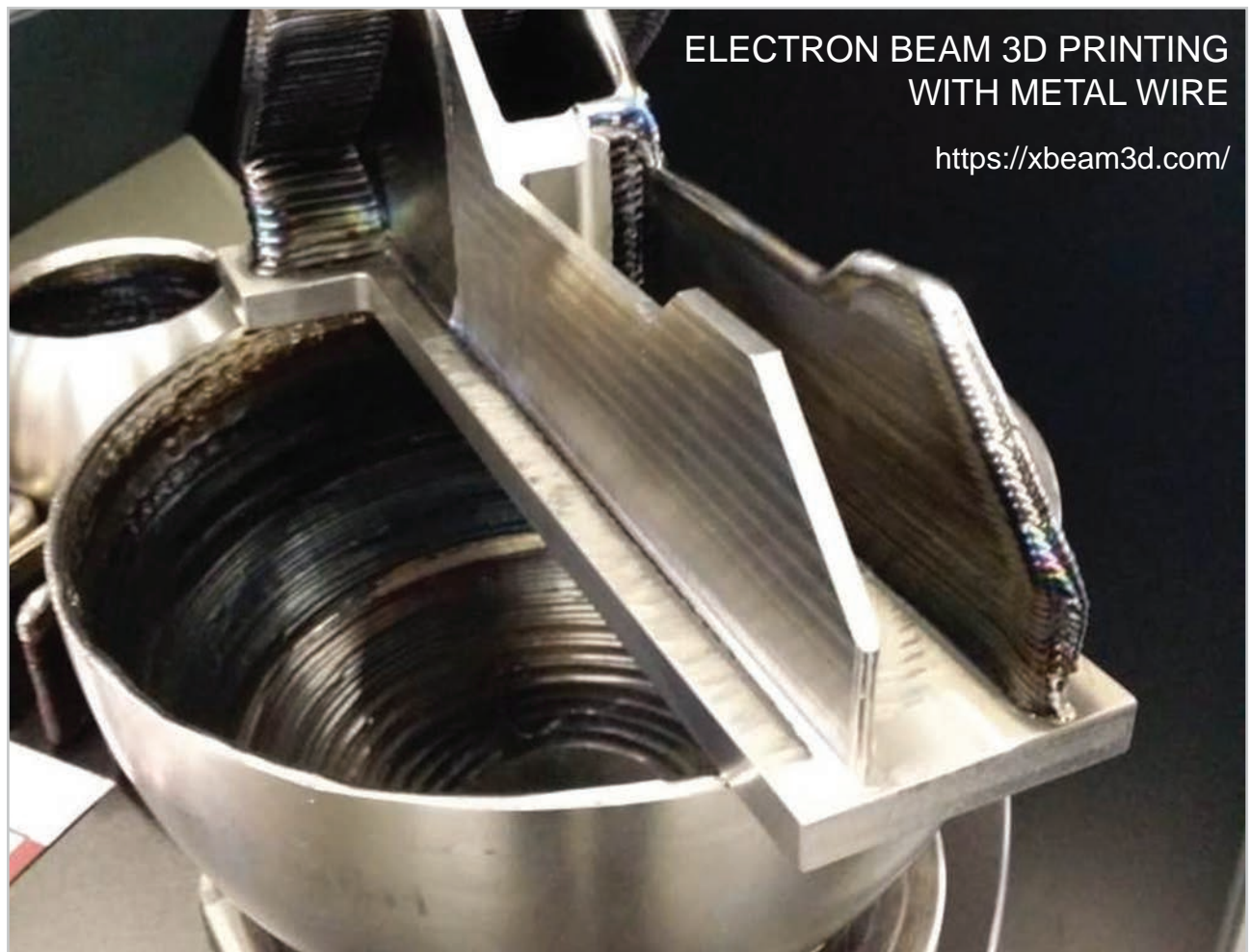
L.M. Lobanov, V.M. Korzhyk, M.O. Pashchyn, O.L. Mikhodui, A.A. Grynyuk, E.V. Ilyashenko, P.V. Goncharov, P.R. Ustymenko (2022) Deformation-free TIG welding of AMg6 alloy with application of electrodynamic treatment of weld metal. *The Paton Welding J.*, 8, 3–8.

JOURNAL HOME PAGE

<https://pwj.com.ua/en>

Received: 21.06.2022

Accepted: 17.10.2022



**ELECTRON BEAM 3D PRINTING
WITH METAL WIRE**

<https://xbeam3d.com/>

PECULIARITIES OF WELDING COMBINED JOINTS OF 15Kh2M2FBS (P3) AND X10CrMoVNb91 (P91) STEELS

V.Yu. Skulskiy¹, M.O. Nimko¹, A.R. Gavryk¹, I.G. Osypenko¹,
O.V. Vavilov², O.G. Kantor², L.P. Rubashka²

¹E.O. Paton Electric Welding Institute of the NASU
11 Kazymyr Malevych Str., 03150, Kyiv, Ukraine

²JSC “Ukrenergymachines”

199 Heroyiv Kharkova Prosp., 61037, Kharkiv, Ukraine

ABSTRACT

Within the framework of currently urgent problem of reconstruction and restoration of equipment of thermal power units of TPP, work has been performed on development of basic technology of welding body elements of a steam turbine from low-alloyed 15Kh2M2FBS (P3) steel to branchpipes from high-chromium martensitic X10CrMoVNb91 steel with 9 % Cr (P91). The paper gives the results of determination of the thermal mode of welding such combined joints to prevent delayed fracture. Proceeding from study of the influence of different modes of high-temperature tempering on impact toughness of weld metal and hardness of welded joint areas hardened during welding, heat treatment modes were selected, depending on electrode material type. It is shown that the resultant mechanical properties of welded joints correspond to the requirements, specified during work performance.

KEYWORDS: heat-resistant steels, low-alloyed steel, high-chromium martensitic steel, combined welded joints, cold cracks, high-temperature tempering, mechanical properties

INTRODUCTION

As shown by information sources, at present boiler equipment of TPP power units is in an unsatisfactory condition. Its general characteristics include moral obsolescence of project technologies, considerable wear of the equipment (for instance, exceeding the “physical wear limit of 200 thou h” approximately in 80% of power units), limiting the working parameters of the heat carrier for the reason of insufficient heat-resistance of steels, problems of cleaning from pollutant emissions, in particular meeting the current requirements to greenhouse gas emissions, etc. [1].

Considering the current problems in the energy sector [1, 2] and economic capabilities of Ukraine, it is rational, alongside construction of new power sources, to conduct timely repairs and reconstruction of the equipment, using advanced technological solutions and improved structural materials. As regards components, exposed to high temperatures and pressures in service, new modifications of high-chromium steels can be used, having higher long-term strength and corrosion resistance under the working conditions, than the traditional low-alloyed steels. At the present stage, steel with 9 % Cr of P91 (X10CrMoVNb91) type can be the most probable candidate material for work on reconstruction of boiler units. This steel, as well as its new modifications are being studied and are becoming widely applied in the world practice in manufacture of high-temperature components of ther-

mal power units [3, 4]. The advantages of application of such steels is the possibility of raising the working parameters of the heat carrier (up to the temperature of 600–620 °C, pressure up to 31 MPa), reduction of the structure weight, while ensuring their higher reliability in service.

In the proposed work the results of development of the technology of welding tubular elements (branchpipes) from P91 steel to the steam turbine body from low-alloyed steel P3 (15KhM2FBS) are given as an example of upgrading the power equipment. The work was performed in cooperation with JSC “Ukrenergymachines” (former JSC “Turboatom”).

MATERIALS AND METHODS OF INVESTIGATION

Chemical composition of the used steels is given in Table 1. For welding their combined joint, electrodes with deposited metal alloying close to the composition of each steel were selected (Table 2). Before application, the electrodes were baked by the mode, recommended by the manufacturer (Böhler Thyssen Schweisstechnik), at 300–350 °C, 2 h. Quantity of diffusible hydrogen H_{dif} was determined by alcohol analysis, using “pencil” samples of electrode metal, deposited into a copper chill mould [5]. For Thermanit Chromo 9V electrodes, H_{dif} was equal to 0.117–0.5, for Thermanit P24 it was 0.582–1.9 cm³/100 g. Considering the susceptibility of steels to hardening, the influence of the thermal mode of welding (preheating) on prevention of delayed fracture was evaluat-

Table 1. Chemical composition of heat-resistant steels used in the work, wt.%

Steel	C	Si	Mn	S	P	Cr	Ni	Mo	V	Nb
П3	0.115	0.468	0.67	0.023	0.027	1.95	0.16	1.12	0.32	0.072
P91	0.085	0.33	0.43	0.015	0.013	8.85	0.12	1.0	0.25	0.069

Table 2. Chemical composition of electrode metal, wt.%

Electrode grade	C	Si	Mn	S	P	Cr	Ni	Mo	V	Nb	Ti
Thermanit Chromo 9V	0.12	0.1	0.55	<0.001	0.010	9.0	0.75	0.98	0.25	0.038	0.006
Thermanit P24	0.11	0.1	0.33	<0.001	0.011	2.6	0.01	0.90	0.20	0.028	0.002

ed, using traditional test methods — Implant test and welding of rigid butt joints of Tekken type with asymmetrical Y-shaped groove in the control zone (DSTU EN ISO 17642-2, DSTU EN ISO 17642-3 [6, 7]). Implant samples (of 8 mm dia) had a spiral stress raiser at the end of the working part, which is welded to the plate, having the form of a groove of V-shaped profile 0.5 mm deep with 40° opening angle and 0.1 mm rounding-off radius at the tip (in keeping with DSTU EN ISO 17642-3). Here, at Implant tests the preheating temperature was measured by the potentiometer and thermocouple of XA type (in a protective ceramic sheath), passed through an opening in the supporting plate and welded to the sample by a capacitor-discharge machine [8]. At Tekken tests and welding of control butt joints a contact thermocouple of the same type with KSP4 potentiometer was used. Mechanical properties were determined in keeping with the provisions of the current standards on static tensile testing (of weld metal and welded joints according to DSTU EN-ISO 5178:2015, DSTU EN ISO 4136:2014), impact testing of welds (DSTU EN ISO 9016:2019) and static bend testing of welded joints (DSTU EN ISO 5173:2019). Vickers hardness was measured at 5 kg load. Samples prepared in keeping DSTU ISO 204:2019 were used to assess the long-term strength (of weld metal and welded joints). Test samples were prepared from combined butt joints of steels P3–P91 20 mm thick with 30° bevel. Welding was performed with both types of studied electrodes in the following

modes: for root passes — current $I_w = 95\text{--}105$ A, voltage $U_a = 24$ V, welding speed $v_w \sim 5$ m/h; for filling passes — $I_w = 130\text{--}140$ A, $U_a = 24$ V, $v_w \sim 16\text{--}20$ m/h; preheating specified by experimental results (see further) was equal to 200–230 °C. Metallographic studies of the microstructures were conducted using light microscope Neophot-32.

RESULTS AND THEIR ANALYSIS

During work performance the main objective was to ensure both the welded joints resistance to delayed fracture (cold cracks) that is always required in welding of hardenable steels, and weld metal impact toughness not lower than 51 J/cm² (41 J [6]) at their strength not lower than that of the base metal.

Thermal mode of welding is known to be the main technological factor in counteracting the delayed fracture, alongside limiting the concentration of diffusible hydrogen, penetrating into the weld. The mode, in its turn, is controlled by preheating/accompanying heating of metal in the joint zone. Figure 1 gives the results of quantitative evaluation of the influence of preheating on the studied steel resistance to this kind of fracture, obtained by Implant test. The criterion is maximal-critical-stresses, exceeding which leads to the joint damage.

Results of testing joints of P3 steel show that preheating to approximately 100 °C does not affect the fracture resistance. Critical stresses remain on the same level, as in welding without preheating. However, at preheating up to 150 °C and higher, cracking

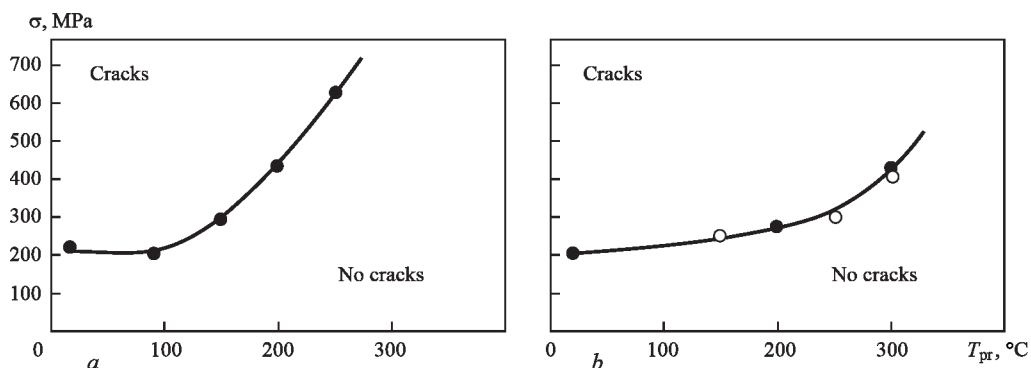


Figure 1. Influence of preheating temperature at Implant tests on critical stresses causing delayed fracture of welded joints: *a* — P3 steel; Thermanit P24 electrodes; *b* — P91 steel, ThermanitChromo 9V electrodes

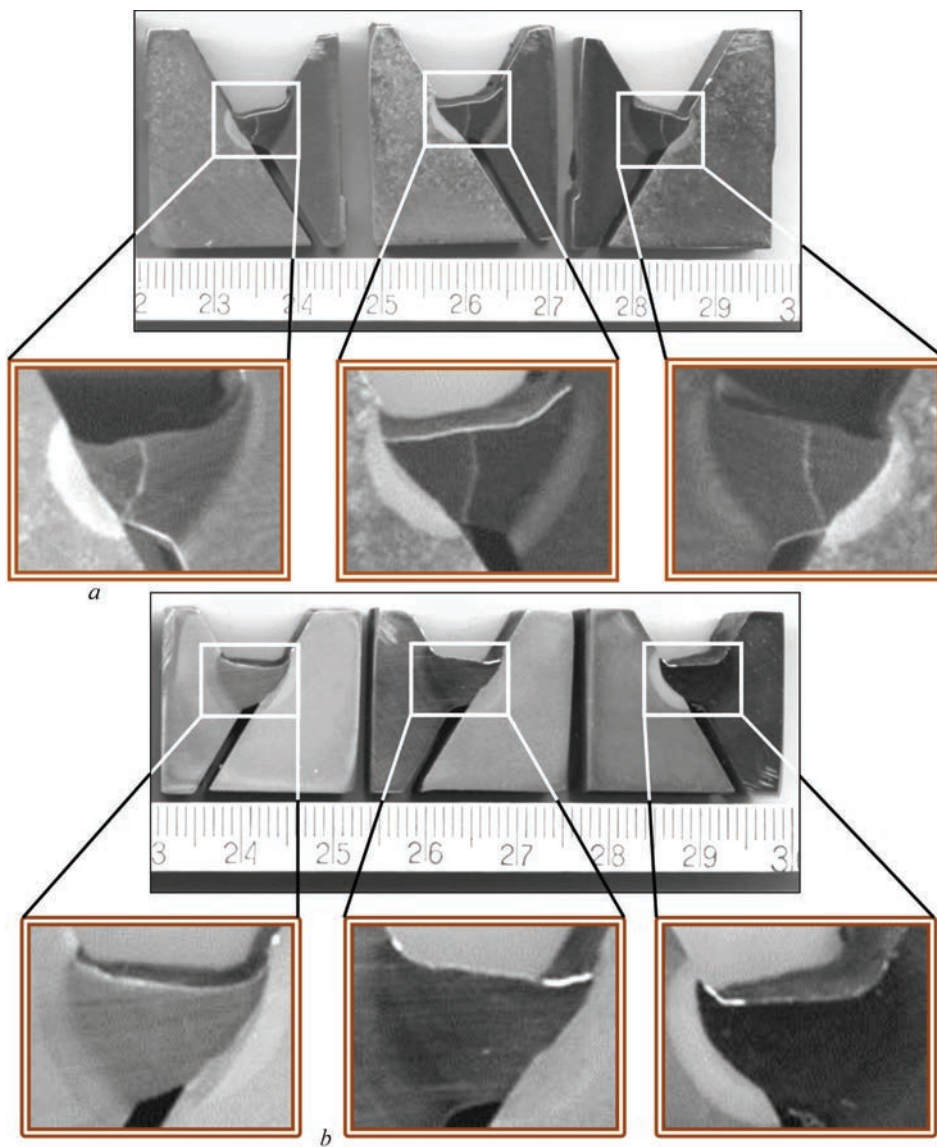


Figure 2. Transverse sections cut out of Tekken joints: *a* — Thermanit P24 electrode; $T_{pr} = 150\text{ °C}$ (cracks); *b* — Thermanit Chromo 9V electrode $T_{pr} = 150\text{ °C}$ (no cracks)

resistance rises abruptly. It confirms the rationality of welding P3 steel with preheating to more than 150 °C .

In the joints of martensitic steel P91, an increase of cracking resistance intensity is observed at the temperature above 200 °C . Under the above-mentioned conditions, however, these joints can stand lower critical stresses than P3 steel joints, i.e. the martensitic complex-alloyed chromium steel has higher delayed cracking resistance than does P3 steel. In view of this fact, when producing combined joints of both the steels, such a thermal mode should be used, which reduces the risk of cracking in welding chromium steel proper. As one can see from the results of Implant tests (Figure 1, *b*) it can be preheating to $200\text{--}250\text{ °C}$.

As Implant tests allow loading the welded joints to stresses, which may not correspond to stresses in the real joints and may be much higher, the delayed fracture resistance was checked using technological sam-

ples — Tekken butt joints. Two combined joints of P91 + P3 steels were used for each thermal mode, in which each steel had one and two bevels, (taking into account the asymmetric Y-shaped configuration of the edges in the butt). After welding the joint was kept for not less than 24 h before further testing. Presence of cracks was determined visually at examination of the butt surface and studying in the light microscope the transverse templates cut out of the joint, ground and chemically etched to reveal the macrostructure (Figure 2). The obtained data are given in Table 3.

Generalizing results of testing for technological strength, preheating up to and maintaining the interpass temperature of $175\text{--}250\text{ °C}$ can be regarded as sufficient. In welding joints of a large cross-section and under the conditions of intensive heat removal, the preheating temperature should be increased (up to $250\text{--}300\text{ °C}$) to prevent its decrease in the welding zone below the specified minimal level.

Table 3. Results of welding butt combined Tekken samples from P3 + P91 steels

Preheating temperature T_{pr} , °C	Thermanit chromo 9V weld (9 % Cr)	Thermanit P24 weld (2.5 % Cr)
	Presence of cracks	
150	Yes*	No
175	No	
200		

*Crack in the weld.

In welding hardenable steels tempering is the main technological technique of regulation of the mechanical properties, structural and stressed state. This operation, however, becomes problematic at heat treatment of combined joints of steels with considerable differences in alloying, when different modes are recommended for each of them, and particularly, in the absence of coincidences in the temperature ranges of recommended tempering. In such cases, the technology of producing the joints becomes much more complicated: it becomes necessary to use metals of intermediate composition (welded metal or inserts of other steels) and heat treatment in several stages. This topic will be considered in a separate publication.

Proceeding from literature and reference data, tempering of P3 steel can be conducted at 730–750 °C, of steel P91 — at 750–760 °C (according to [10], the range can be wider: from 740 to 780 °C). As recommended by electrode manufacturer (Böhler Thyssen), 740 °C is the most favourable for weld metal of Thermanit P24 type, and for Thermanit Chromo 9V type it is 760 °C. For all the materials in the combined joint

the range of close tempering temperatures is equal to 740–750 °C.

The final heat treatment mode needed to be precised, considering the following conditions: 1) tempering at a higher temperature gives a greater guarantee of obtaining the required properties and in a shorter time; 2) increase of tempering temperature for metal with a limited maximum heating temperature may lead to its greater softening; 3) known “inertness” of welds of P91 type as to increase of ductility and impact toughness requires application of higher temperatures, tempering at lower temperatures restrains these indices reaching the required level and may require increase of tempering duration.

In this regard, a study was carried out on the influence of heat treatment modes on impact toughness of weld metal, metal hardness in the joint zone and resulting mechanical properties. Considering prior experience and literature data, tempering was conducted with different soaking at temperatures of 740, 750 and 760 °C. Lower temperature was not used, because of the possibility of obtaining unsatisfactory results for weld of P91 type.

The primary task was to ensure the impact energy of the more problematic martensitic chromium welds below the critical value of 41 J ($KCV = 51 \text{ J/cm}^2$). Also taken into account was tempering mode influence on HAZ metal hardness becoming closer to that of the base metal, which was taken as an approximate criterion of achieving a uniform structural state and mechanical properties of the metal of near-weld zone.

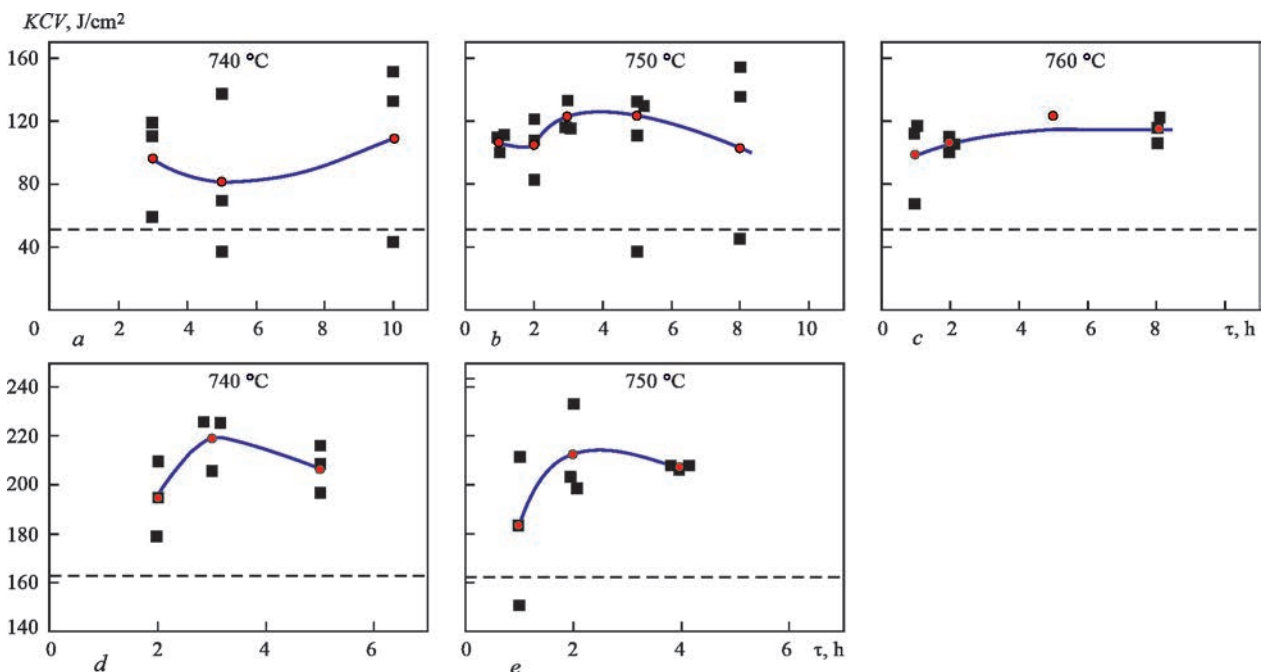


Figure 3. Influence of tempering mode on impact toughness of weld metal in P3 + P91 steel welded joints: a–c — welding with Thermanit Chromo 9V electrodes; d, e — welding with Thermanit P24 electrodes

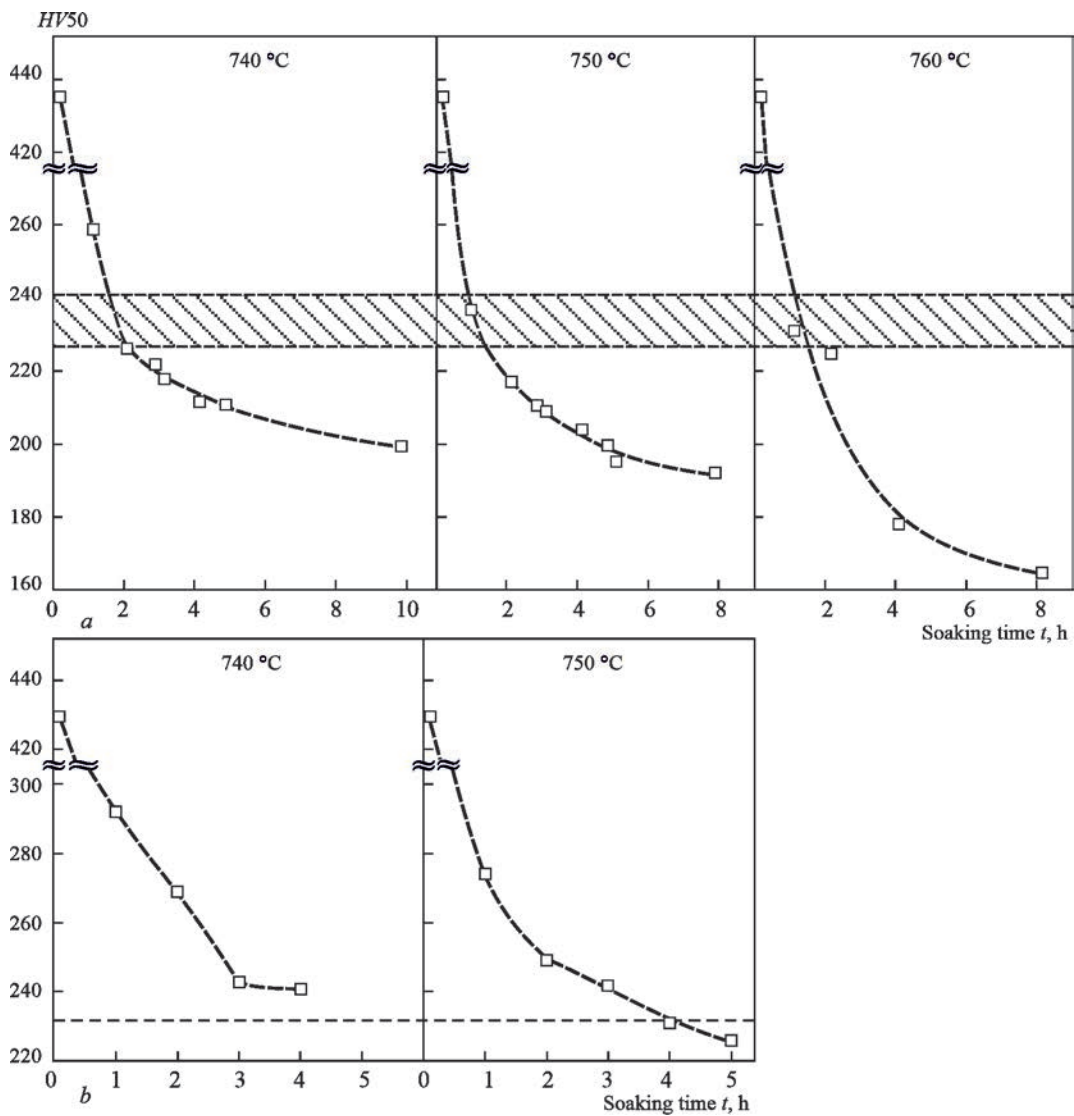


Figure 4. Influence of temperature and duration of postweld tempering on HAZ metal hardness in the area of hardening of P3 + P91 steel welded joints (welding with Thermanit Chromo 9V electrodes): *a* — metal hardness in P3 steel HAZ; *b* — metal hardness in P91 steel HAZ

Obtained test results are given in Figures 3–6. In Figure 3 dashed lines show the target levels of impact toughness: specified minimum for martensitic welds with 9 % Cr (Figure 3, *a–c*) and averaged level, which, by the data of electrode manufacturer, is usually provided by welds of P24 type (Figure 4, *d, e*).

Proceeding from the derived regularities, at the change of impact toughness the following can be regarded as favourable modes:

1) for joints made by Thermanit Chromo 9V electrodes:

- 740 °C, 2–3 h;
- 750 °C, 1–2 h;
- 760 °C, 1 h.

2) for joints made by Thermanit P24 electrodes:

- 740 °C, 2 h;
- 750 °C, 1 h.

For the above modes, the obtained average *KCV* exceed the target level for both weld types. Mean-

while, for 9 % Cr welds treated at 740 °C, an increased scatter of test results and possibility of individual *KCV* values dropping to minimal level is observed (Figure 3, *a*). On the whole, however, in view of the data on the admissibility of lowering of impact energy for chromium welds to 27 J (or *KCV* to 34 J/cm²) [11, 12], such results can be considered acceptable.

As one can see from Figures 4, 5, the studied steels demonstrate different sensitivity to temper heating that can be traced by the nature of the change of hardness values of hardened HAZ metal. So, in P3 steel at all the temperatures the hardness drops abruptly and reaches base metal level (240–225 *HV*) approximately in 1–1.5 h. At minimal temperature (740 °C) soaking for more than 3–4 h leads to a noticeable lowering of hardness below this level. A more significant softening takes place at transition to tempering at 750 and 760 °C, starting from soaking for more than 2 h. Hardened regions of P91 steel undergo less intensive

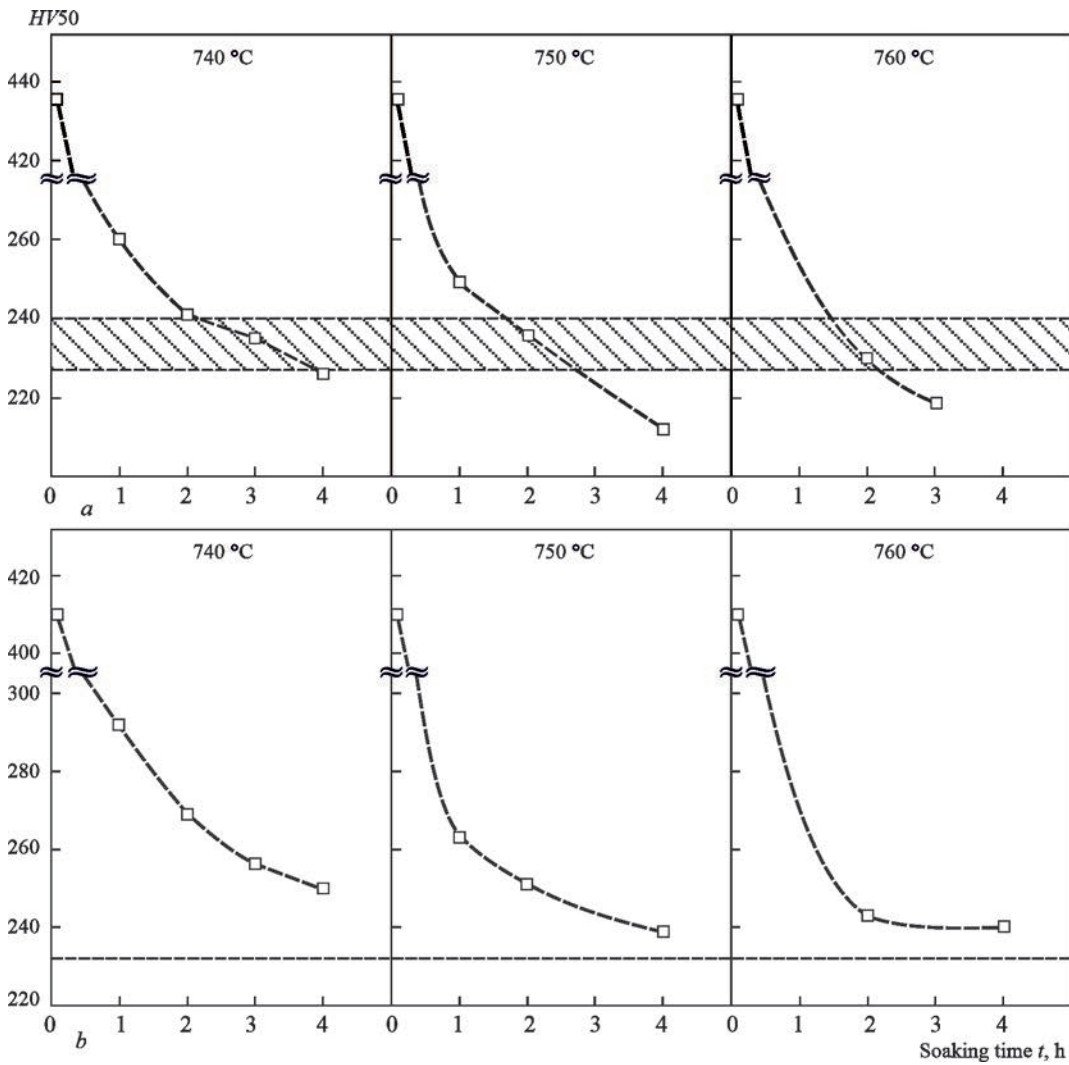


Figure 5. Influence of temperature and duration of postweld tempering on HAZ metal hardness in the area of hardening of P3–P91 steel welded joints (welding with Thermanit P24 electrodes): *a* — HAZ metal hardness in P3 steel; *b* — HAZ metal hardness in P91 steel

tempering. In the used modes, hardness is gradually lowered to the level close to base metal initial hardness (233 HV), while remaining somewhat greater, as one can see from the data obtained at 740 °C. No significant softening after long-term soaking (4–5 h) at higher temperatures (750, 760 °C) was found. The na-

ture of the change of weld metal hardness in different modes is close to the change of HAZ metal hardness (Figure 6).

Note that practical experience of tempering welded joints of some heat-resistant hardening steels envisages application of temperatures by 20 to 40 °C lower

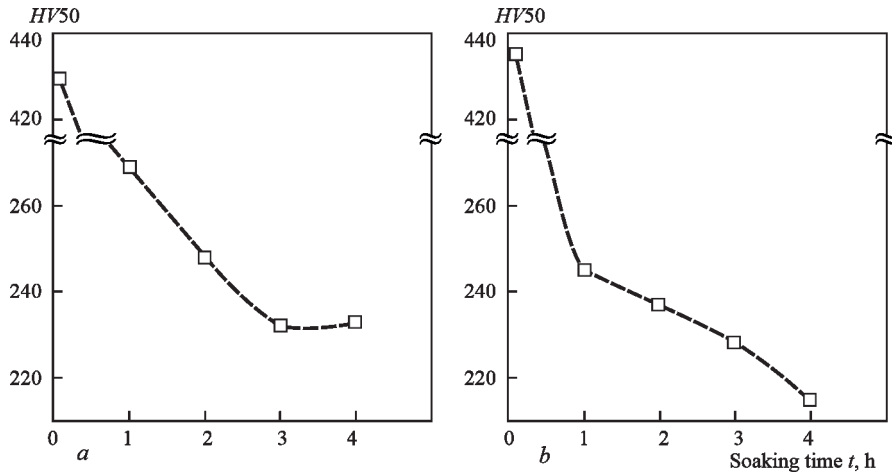


Figure 6. Influence of tempering at 740 °C on hardness of weld metal in P3 + P91 steel joints, welded by different electrodes: *a* — Thermanit Chromo 9V electrodes with 9 % Cr; *b* —Thermanit P24 electrodes with 2.25 Cr %

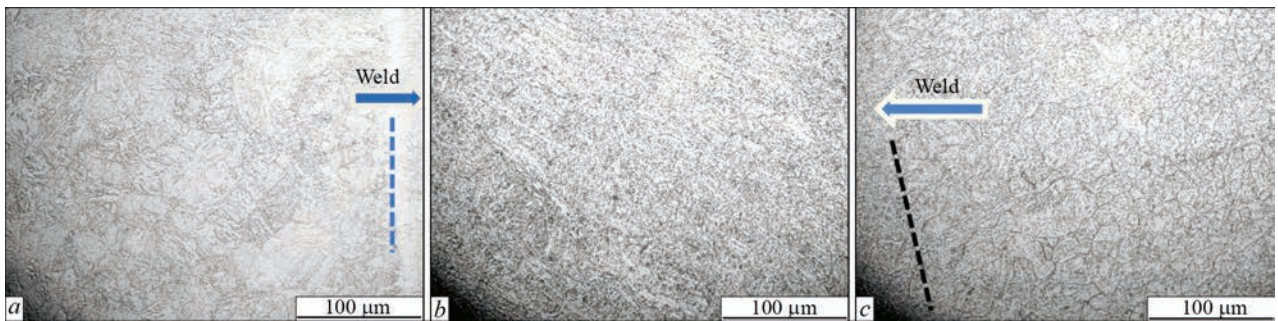


Figure 7. Microstructure of a joint welded with Thermanit Chromo 9V electrodes: *a* — HAZ and area of fusion of P3/weld; *b* — weld metal; *c* — HAZ metal and area of fusion of P91/weld

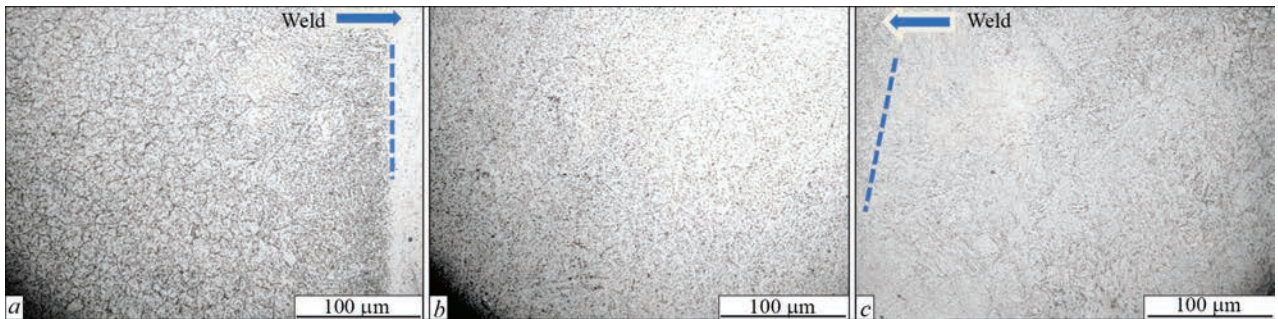


Figure 8. Microstructure of a joint ($\times 400$) welded with Thermanit P24 electrodes: *a* — HAZ and area of fusion of P91/weld; *b* — weld metal; *c* — HAZ metal and area of fusion of P3/weld

than the steel tempering temperature in its production. The objective of this measure is prevention of further structural changes and possible lowering of the initial strength characteristics of base metal. Under such conditions, HAZ metal hardness will be higher than that of steel in as-delivered condition. Moreover, in keeping with DSTU ISO 15614-1 standard, hardness of metal in martensitic chromium steel welded joints should not be higher than 350 *HV*, i.e. higher hardness of HAZ metal from the side of P91 steel that is observed at lower tempering temperature (as at 740 °C) should not be regarded as a rejection characteristic.

Considering the conditions for ensuring the necessary level of weld impact toughness, limitation of overheating of base metal and metal in the welded joint zone, the following modes of tempering the combined P3–P91 joint were selected: in welding with Thermanit Chromo 9V electrodes — 740 °C, 3 h, and with Thermanit P24V electrodes — 740 °C, 2 h.

Verification of the specified technological measures consisted in evaluation of the quality and mechanical properties of control butt joints produced with application of both the selected electrode types. Welding was performed with preheating to 200 °C and interpass temperature of up to 230 °C, tempering — by the above-given modes. Quality was evaluated visually and by metallographic examination of transverse microsections. Results of visual examination and metallographic analysis confirmed absence of cracks in welded joints. No pores, slag inclusions,

lacks-of-fusion were found (Figures 7, 8). In as-tempered condition, hardness of both types of welds was on the level of 230 *HV*.

Mechanical properties of welds and welded joints after short-term tensile and impact bend testing are given in Table 4. Tensile testing of transverse samples showed that weld strength was higher than that of base metal at room and working temperatures: all the samples broke through the HAZ metal. At static bending through an angle of 120° (Figure 9), no defects developed in the joints.

For maximum operating temperature (570 °C), the value of long-term strength limit of the metal of welds and welded joints was obtained by direct testing for periods of 10^3 and 10^4 h and by approximation method — for 10^5 h (Table 5). In all the cases of testing transverse samples of welded joints fracture ran through the HAZ

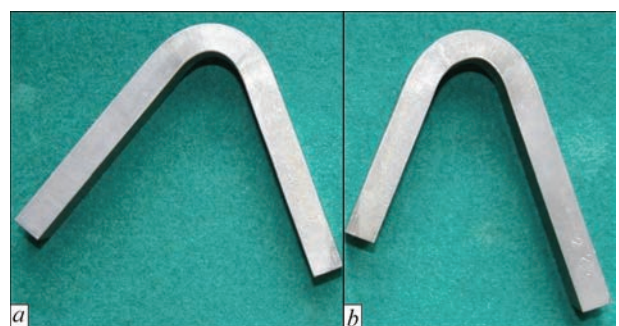


Figure 9. Samples of welded joints after testing for static bending at 20 °C: *a* — Thermanit Chromo 9V weld; *b* — Thermanit P24 weld

Table 4. Mechanical properties of combined welded joints

Electrode grade	$T_{\text{test}}, ^\circ\text{C}$	Weld metal*					Welded joint	
		$\sigma_{0.2}, \text{MPa}$	σ_t, MPa	$\delta, \%$	$\psi, \%$	$KCV, \text{J/cm}^2$	σ_t, MPa	Fracture area
Thermanit Chromo 9V	20	601.0	729.0	20.0	64.8	110.1	617.4	P3 HAZ metal
		602.5 (601.8)**	725.3 (727.2)	17.0 (18.5)	40.2* (64.8)	119.7 59.1 (96.3)	613.7 (615.6)	P3 HAZ metal
Thermanit Chromo 9V	570	376.9	407.9	20.3	79.8	–	353.6	P91 HAZ metal
		345.9 (361.4)	394.0 (401.0)	24.7 (22.5)	82.7 (81.3)	–	366.9 (360.3)	P91 HAZ metal
Thermanit P24	20	621.7	714.7	21.0	67.6	178.9	666.0	P3 HAZ metal
		618.5 (620.1)	718.6 (716.7)	19.7 (20.4)	69.7 (68.7)	209.0 193.8 (193.9)	669.5 (667.8)	P91 HAZ metal
Thermanit P24	570	409.9	447.5	19.3	79.8	–	396.2	P91 HAZ metal
		411.2 (410.6)	454.4 (451.0)	21.7 (20.5)	81.2 (80.5)	–	383.7 (390.0)	P91 HAZ metal

*Rupture near the working zone edge.
**Average value is given in the brackets.

Table 5. Results of long-term strength testing of composite welded joints of P3 + P91 steels

Sample type	Long-term strength limit (MPa) and fracture site				
	In 10 ³ h	Fracture site	In 10 ⁴ h	Fracture site	In 10 ⁵ h
Thermanit P24 deposited metal	193	–	147	–	112
Welded joint, Thermanit P24 weld	147	P3 HAZ metal	94	P3 HAZ metal	60
Thermanit Chromo 9V deposited metal	209	–	187	–	167
Welded joint, Thermanit Chromo 9V weld	152	P3 HAZ metal	87	P3 HAZ metal	50

metal of low-alloyed P3 steel. Weld metal had much higher fracture resistance than base metal.

CONCLUSIONS

1. It is shown that prevention of delayed fracture of the combined joints of P3 + P91 steels in welding by Thermanit Chromo 9V or Thermanit P24 electrodes can be achieved at preheating do not lower than 175 °C.

2. Proceeding from the conducted investigations, the following high-temperature tempering modes are recommended, depending on the applied type of welding electrodes: 740 °C, 3 h (Thermanit Chromo 9V electrodes) and 740 °C, 2 h (Thermanit P24 electrodes).

3. Welding of control combined joints confirmed that application of the proposed heat-treatment welding modes and high-temperature tempering provides absence of cold cracks, relatively homogeneous tempering structure with hardness of 220–240 HV of pre-hardened regions of welded joints, high impact toughness of weld metal (98 J/cm² for Thermanit Chromo 9V welds and 190 J/cm² for Thermanit P24 welds on average) and their higher short-term (at 20 °C) and long-term strength (at 570 °C) than that of base metal.

4. The developed welding process was accepted at JSC “Ukrenergymachines” for practical application.

REFERENCES

- (2016) Coal thermal power engineering: Ways of reconstruction and development. In: *Proc. of Int. Sci.-Pract. Conf. Kyiv*.
- Teslenko, O.I., Gorskyi, V.V., Maliarenko, O.Ye. (2020) Analysis of tendencies and directions of development thermal power engineering. *Problemy Zagalnoi Energetyky*, 60(1), 38–46 [in Ukrainian].
- Liratzis, T., Forno, M., Piombino, C. et al. (2010) Acciai martensitici al 9Cr–1Mo–Nb–V: Proprietà, soldabilità e controlli. *Riv. Ital. Saldatura*, Marzo/Aprile, 2, 161–168.
- Ahmet Shibli (2014) *Coal Power Plant Materials and life Assessment. Developments and Applications*. Woodhead Publishing.
- Kozlov, R.A. (1986) *Welding of heat-resistant steels*. Leningrad, Mashinostroenie [in Russian].
- Sawhill, J.M., Dix, A.W., Sawage, W.F. (1974) Modifild implant test for studying delayed cracking. *Weld. J.*, 35(12), 554–560.
- Hrivnak, I. (1984) *Weldability of steels*. Moscow, Mashinostroenie [in Russian].
- Skulsky, V.Yu., Strizhius, G.H., Nimko, M.A. et al. (2019) Delayed fracture resistance of welded joints of rotor steel 25Kh2NVFA after welding reheating. *The Paton Welding J.*, 2, 7–12. DOI: <http://dx.doi.org/10.15407/tpwj2019.02.01>

9. Brózda, J. (2004) Stale żarowitrymałe nowej generacji, ich spawalność i własności złączny spawanych. Część IV. Stal E911. *Biuletyn Instytutu Spawalnictwa*, **4**, 49–54.
10. (1993) *Specification*. Werkstoffblatt 435 R. Ausgabe März. Mannesmannröhren-Werke AG, Düsseldorf.
11. Skulsky, V.Yu., Tsaryuk, A.K., Gavrik, A.R. et al. (2016) Selection of modes of high-temperature tempering of heat-resistant steel welded joints made by electrodes Thermanit MTS616. *The Paton Welding J.*, **9**, 47–50. DOI: <http://doi.org/10.15407/tpwj2016.09.10>
12. Mokhila, P., Foldynova, K. (2014) Effect of postweld heat treatment on mechanical properties of P92 steel welded joints performed by submerged-arc welding. *Metallovedenie i Termich. Obrab. Metallov*, **4**, 36–39 [in Russian].

ORCID

V.Yu. Skulskyi: 0000-0002-4766-5355,
 M.O. Nimko: 0000-0002-9672-4921,
 A.R. Gavryk: 0000-0002-0793-2754,
 I.G. Osypenko: 0000-0002-9969-7375

CONFLICT OF INTEREST

The Authors declare no conflict of interest

CORRESPONDING AUTHOR

V.Yu. Skulskyi

E.O. Paton Electric Welding Institute of the NASU
 11 Kazymyr Malevych Str., 03150, Kyiv, Ukraine.
 E-mail: vsku@paton.kiev.ua

SUGGESTED CITATION

V.Yu. Skulskyi, M.O. Nimko, A.R. Gavryk, I.G. Osypenko, O.V. Vavilov, O.G. Kantor, L.P. Rubashka (2022) Peculiarities of welding combined joints of 15Kh2M2FBS (P3) and X10CrMoVNb91 (P91) steels. *The Paton Welding J.*, **8**, 9–17.

JOURNAL HOME PAGE

<https://pwj.com.ua/en>

Received: 05.02.2022

Accepted: 17.10.2022

SUBSCRIPTION-2023

«The Paton Welding Journal» is Published Monthly Since 2000 in English, ISSN 0957-798X, doi.org/10.37434/tpwj.

«The Paton Welding Journal» can be also subscribed worldwide from catalogues subscription agency EBSCO.

If You are interested in making subscription directly via Editorial Board, fill, please, the coupon and send application by Fax or E-mail.

12 issues per year, back issues available.

\$384, subscriptions for the printed (hard copy) version, air postage and packaging included.

\$312, subscriptions for the electronic version (sending issues of Journal in pdf format or providing access to IP addresses).

Institutions with current subscriptions on printed version can purchase online access to the electronic versions of any back issues that they have not subscribed to. Issues of the Journal (more than two years old) are available at a substantially reduced price.

The archives for 2009–2020 are free of charge on www://patonpublishinghouse.com/eng/journals/tpwj

ADVERTISING

in «The Paton Welding Journal»

External cover, fully-colored:

First page of cover
 (200×200 mm) — \$700
 Second page of cover
 (200×290 mm) — \$550
 Third page of cover
 (200×290 mm) — \$500
 Fourth page of cover
 (200×290 mm) — \$600

Internal cover, fully-colored:

First/second/third/fourth page
 (200×290 mm) — \$400

Internal insert:

(200×290 mm) — \$340
 (400×290 mm) — \$500

- Article in the form of advertising is 50 % of the cost of advertising area

- When the sum of advertising contracts exceeds \$1001, a flexible system of discounts is envisaged

- Size of Journal after cutting is 200×290 mm

Address

11 Kazymyr Malevych Str. (former Bozhenko Str.), 03150, Kyiv, Ukraine
 Tel./Fax: (38044) 205 23 90, E-mail: journal@paton.kiev.ua
www://patonpublishinghouse.com/eng/journals/tpwj

DOI: <https://doi.org/10.37434/tpwj2022.08.03>

INFLUENCE OF THE COMPOSITION OF CHARGE COMPONENTS OF FLUX-CORED STRIPS OF C–Fe–Cr–Nb ALLOYING SYSTEM ON CHEMICAL COMPOSITION AND STRUCTURE OF THE DEPOSITED METAL

O.P. Voronchuk, O.P. Zhudra, T.V. Kaida, O. V. Petrov, L.M. Kapitanchuk, I.L. Bogaichuk

E.O. Paton Electric Welding Institute of the NASU
11 Kazymyr Malevych Str., 03150, Kyiv, Ukraine

ABSTRACT

It is common knowledge that wear resistance of the deposited chromium carbide layer, additionally alloyed by such carbide-forming elements, as molybdenum, niobium, etc., largely depends on the reinforcing phase characteristics, its concentration, and properties of matrix alloy. Good performance of such alloys under the conditions of abrasive wear at up to 600 °C temperatures is achieved by adding niobium to the alloy composition. This work is a study of charge components of flux-cored strips of C–Fe–Cr–Nb alloying system on the deposited metal composition and properties. The methods of X-ray diffraction, metallographic and X-ray microprobe analysis of metal of 500Kh22B7 type deposited by flux-cored strips, revealed the dependence of concentrations, shape, orientation, phase components and integral hardness of the deposited layer on the form of addition of the main carbide-forming element, namely chromium, to the charge and flux-cored strip cross-section. It was found that at addition of chromium carbide Cr_3C_2 to the flux-cored strip charge, carbide phase concentration in the deposited layer increases by 10 %. Complex carbides of $(\text{Cr}, \text{Fe})_7\text{C}_3$ system are predominantly present in the deposited metal for all the samples. Niobium forms individual carbide components of much smaller dimensions, compared to complex chromium carbide. Optimal concentration of the carbide phase in the metal of 500Kh22B7 type deposited by flux-cored strip is achieved by addition of a carbide-forming element, namely chromium, to the electrode material charge, in the form of chromium carbide and ferrochromium. Flux-cored strip cross-section and surfacing modes practically do not affect the deposited layer properties.

KEYWORDS: flux-cored strip, chromium carbide, ferrochromium, niobium, carbides, hardness, microstructure, matrix, concentration

INTRODUCTION

Many parts of metallurgical equipment operate under the conditions of abrasive and gas-abrasive wear at normal and higher temperatures in combination with impact loads [1–3, etc.]. Selection of the alloy type for surfacing such parts is determined by the possibilities of surfacing some items, financial possibility, as well as the nature of loading, particularly in combination of abrasive wear and shock at increased (up to 600 °C) temperatures [4]. For substantiated alloying of wear-resistant alloys it was necessary to establish rational alloying limits, which would provide optimal properties of the deposited layer [5–7]. Studying the relation between alloy wear resistance and carbide phase structure, as well as between the regularity of carbide formation and alloy chemical composition is the most important for rational alloying of the materials. It is known that alloys having high hardness carbides with cubic lattice in their composition demonstrate the highest wear resistance [8–10, etc.]. However, deposited metal with carbides and with a different crystalline lattice, for instance hexagonal, also has a satisfactory wear resistance. For one and

the same carbide type, its properties will somewhat differ, depending on alloying. So, metal with carbides of Me_7C_3 type, containing a large quantity of iron, will differ by their wear resistance from metal of carbides of the same type, but with a smaller quantity of iron. Note that carbide hardness depends on the degree of their alloying that, in its turn, influences the deposited metal wear resistance. Kinetics of carbide formation at metal solidification is related to the value of Me/C (metal/carbon) ratio. In the presence of several carbide-forming elements in the deposited metal carbides of elements with the highest affinity to carbon are the first to form.

The objective of this work is studying the influence of carbide-forming components of the charge of PL-AN185 flux-cored strip, electrode material cross-section, and influence of surfacing modes on the structure and phase components of the deposited metal to produce a coating resistant to abrasive and gas-abrasive wear at higher temperatures.

INVESTIGATION PROCEDURE AND EQUIPMENT

The methods of X-ray diffraction, metallographic and X-ray microspectral analyses were used to study the

deposited metal of 500Kh22B7 type. Hardness measurements were conducted in M-400 microhardness meter of Leco Company, JAMP-950F and DRON-UM1 instruments were used for X-ray spectral, electron microscopy and X-ray diffraction investigations. Microstructural studies were performed in Neophot-32 microscope.

Sample surfacing was performed by electric arc process using PL-AN185 self-shield flux-cored strip that ensures producing deposited metal of the following chemical composition, wt.%: 4.5 C; 22 Cr; 7 Nb. Surfacing was performed by flux-cored strips of 16.5×40 mm (samples Nos 1, 3) and 10.0×3.0 mm cross-section (sample No. 2). PL-AN185 flux-cored strip was used for surfacing wear-resistant bimetal plates from 5 to 30 mm thick and other parts of metallurgical, power and mining equipment [11].

In C-Fe-Cr-Nb alloying system the reinforcing phase is the present predominantly chromium and niobium carbides, and the matrix is an iron-based alloy. It is important to determine how the concentration of carbides and other deposited layer characteristics are influenced by the method of addition of the main carbide-forming component, namely chromium to the flux-cored strip charge. High-carbon ferrochromium of FKh900 grade (sample No. 3) and chromium carbide in other samples were used to add chromium. The latter by its chemical composition is close to the stoichiometry of Cr_3C_2 carbide. Niobium was added to the flux-cored strip charge using ferroniobium. Moreover, graphite and other technological fillers were further added to the charge composition.

EXPERIMENTAL STUDIES AND THEIR RESULTS

Experimental studies were conducted on samples of metal of 500Kh22B7 type, deposited by a strip with a standard charge from chromium carbide, produced in different modes: $I_w \sim 750\text{--}850$ A (sample No. 1), $I_w \sim 450\text{--}500$ A (sample No. 2), sample No. 3 was produced using electrode strip with high-carbon ferrochromium of FKh900 grade in the following mode: $I_w \sim 750\text{--}850$ A. Here, other charge components remained unchanged. Table 1 gives the average composition in the samples of the deposited metal type.

Surfacing was performed in two layers as at two-layer surfacing with the strips the influence of

base metal (first layer) decreases and the working zone (second layer) forms only under the influence of the flux-cored strip material.

The weight fraction of phase components, type of crystalline lattice and its parameters were assessed by the method of X-ray diffraction analysis: $\gamma\text{-Fe} - 54.4$; $(Fe, Cr)_7C_3 - 22.3$; NbC - 17.3; $Me_2C - 6.0$ (sample No. 1); $\gamma\text{-Fe} - 57.2$; $(Fe, Cr)_7C_3 - 23.2$; NbC - 15.7; $Me_2C - 3.8$ (sample No. 2); $\gamma\text{-Fe} - 65.7$; $(Fe, Cr)_7C_3 - 16.0$; NbC - 15.9; $Me_2C - 2.4$ wt.% (sample 3). When producing this type of the deposited metal, the matrix structure is of great importance, as austenitic matrix is more appropriate at high loads and presence of impact action. Structure of the studied samples in the transition zone (first layer of the deposited metal) is an austenitic matrix with dendrite-cellular form of crystallization, niobium carbides and eutectic which precipitated on the boundaries of dendrites and cells. The working zone structure (second layer of the deposited metal) of all the studied samples is an alloyed austenitic matrix with dendritic-cellular form of crystallization. In samples No. 1 and 2 alloyed $(Fe, Cr)_7C_3$ and NbC carbides of lancet-like shape 20–25 μm long are chaotically arranged over the entire plane. The nature of crystallization of sample No. 3 in the working layer is somewhat different – the carbides are more dispersed, their size is 2–8 μm , and they are located along the cell boundaries.

Comparative analysis of surfaced samples Nos 1 and 2, produced in different modes (by wide strip at $I_w = 750$ A and by narrow strip at $I_w = 450$ A), showed that the weight fraction of the austenitic component is equal to 54.5 wt.% at $I_w = 750$ A and 57.2 wt.% at $I_w = 450$ A, and at the same modes ($I_w = 750$ A) for samples No. 1 (standard charge with chromium carbide) and 3 (charge with high-carbon ferrochromium of FKh900 grade) the austenitic component of sample No. 3 is equal to 65.7 wt.%. In this case, the carbide component decreases approximately by 10 %. Integral hardness in the working layer of samples Nos 1–3 is equal to 6868; 6870 and 5490 MPa, respectively.

Table 2 gives the average composition of alloying elements of the solid solution of deposited metal (samples Nos 1–3) and its carbide components. Chemical composition of the solid solution and niobium carbides of the three samples practically does not change, and the degree of alloying of (Fe,

Table 1. Average chemical composition of deposited metal 500Kh22B7, wt.%

Sample number	C	Si	Mn	Cr	Ni	Mo	Nb	Fe
1	4.8	1.04	0.29	24.6	≤0.1	0.086	7.3	Base
2	4.7	1.02	0.49	24.4	≤0.1	0.057	7.2	
3	4.5	1.02	0.47	19.6	≤0.1	0.089	8.6	

Table 2. Chemical composition of the solid solution and carbide phases of deposited metal of 500Kh22B7 type, wt.%

Sample number	Working zone solid solution				(Cr, Fe) ₇ C ₃ and NbC carbides				Carbide type
	C	Fe	Cr	Nb	C	Fe	Cr	Nb	
1	1.17	82.50	14.35	0.85	8.62	32.90	57.80	0.45	(Fe, Cr) ₇ C ₃
					11.20	1.20	1.19	85.60	NbC
2	1.25	82.70	13.90	0.30	8.64	32.70	58.00	0.44	(Fe, Cr) ₇ C ₃
					11.40	0.95	2.25	84.20	NbC
3	1.70	82.02	13.45	0.20	8.55	48.60	41.60	0.25	(Fe, Cr) ₇ C ₃
					10.80	1.28	1.65	84.80	NbC

Cr)₇C₃ carbides, located in the eutectic along the cell boundaries in sample No. 3 (without addition of chromium carbide to the charge, with its replacement by high-carbon ferrochromium), is somewhat different from that of the same type of carbides in samples Nos 1 and 2.

Integral hardness in height of the deposited layer changes gradually from the base metal to its surface in the range from 3700 to 6700–6900 MPa (samples Nos 1, 2) and from 3800 to 5400 MPa (sample No. 3), and it is leveled in the second layer of the deposited metal that corresponds to the change of chemical

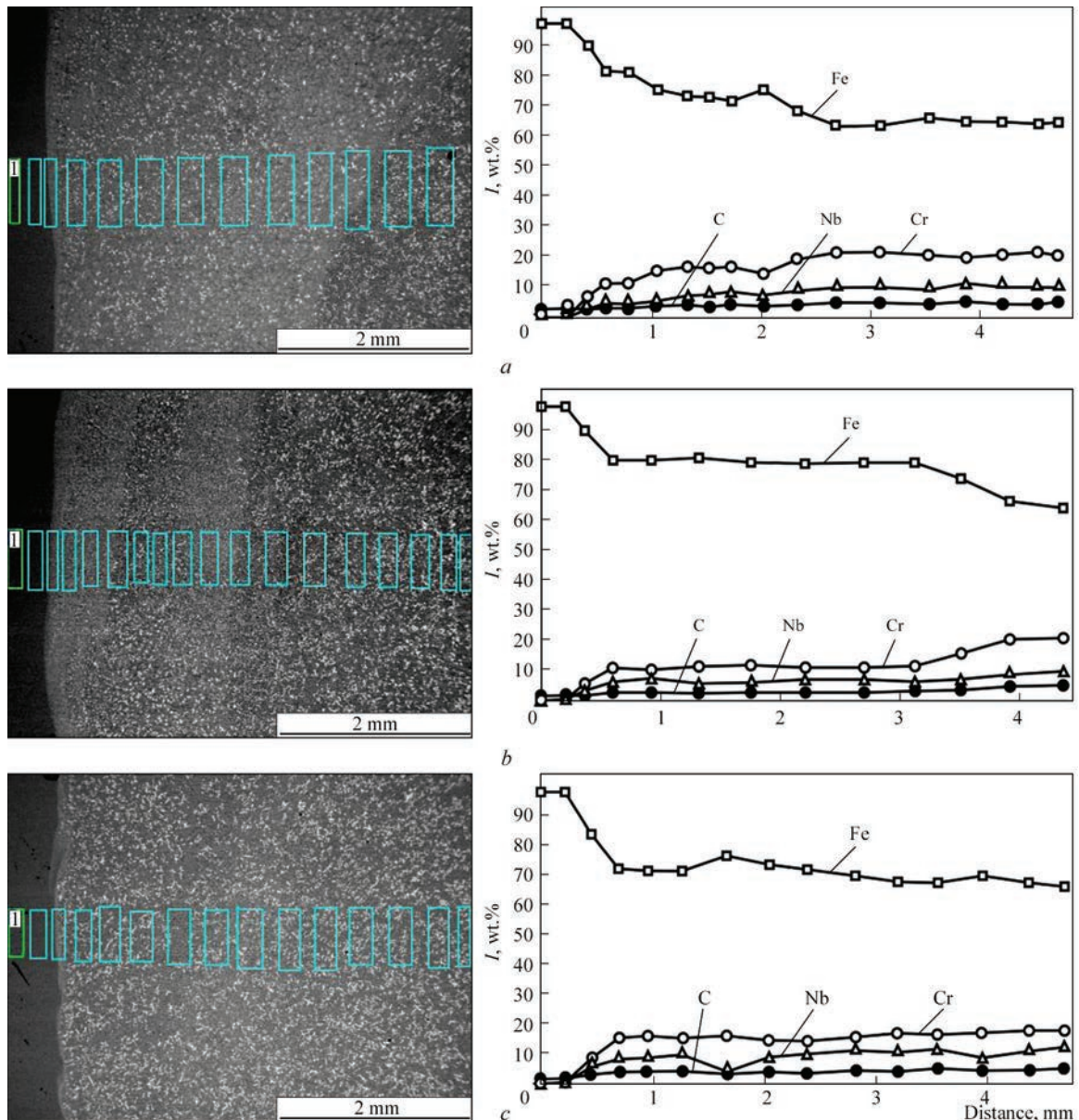


Figure 1. Electronic image and linear distribution of alloying elements in the deposited layer height: *a-c* — samples Nos 1–3, respectively

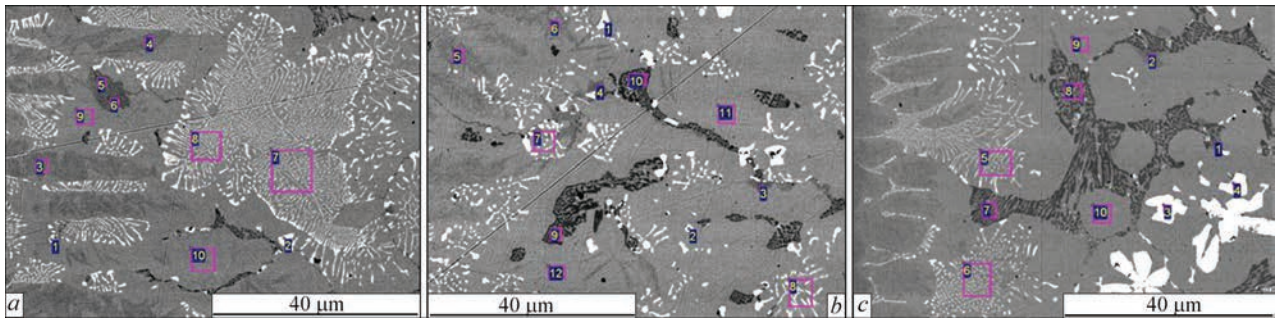


Figure 2. Electronic image of structural components of the deposited metal transition zone: *a-c* — samples Nos 1–3

composition on integral curves of linear distribution of alloying elements. The zone of fusion with the base metal has a smooth concentrational transition with further leveling of the chemical composition in the working zone. Linear distribution of alloying elements in the deposited layer height is shown in Figure 1. Chemical composition of the deposited layer along the line of electronic probe passage can be determined by the concentration scale.

Structure of crystallization of the transition zone of base metal–deposited layer is dendritic-cellular with eutectic precipitates in interdendritic areas on the cell boundaries and separate precipitates of niobium carbides. Two kinds of eutectic are observed — based on niobium carbide and on $(Fe, Cr)_7C_3$ carbides. Electronic image of the transition zone of base metal–de-

Table 3. Average chemical composition of the solid solution and eutectic formations of sample No. 1. Treatment parameters, wt. %

Spectrum number	C	Cr	Fe	Nb
1	11.87	1.28	3.64	83.07
2	11.51	3.96	18.89	65.45
3	1.30	6.72	90.55	0.55
4	1.42	7.16	90.20	0.41
5	2.61	12.00	84.45	0.24
6	2.63	12.91	83.72	0.00
7	2.06	8.60	81.63	6.96
8	2.52	8.34	80.17	8.27
9	1.90	9.38	87.72	0.18
10	1.37	8.82	88.69	0.20

Table 4. Average chemical composition of the solid solution and eutectic formations of samples No. 2. Treatment parameters, wt. %

Spectrum number	C	Si	Cr	Mn	Fe	Nb
1	9.76	0.00	1.69	0.77	2.67	83.67
2	11.44	0.05	1.85	0.18	3.39	82.61
3	2.10	0.44	8.71	1.22	86.78	0.42
4	2.40	0.48	8.21	1.69	86.62	0.11
5	1.39	0.43	5.49	0.92	91.41	0.28
6	1.74	0.42	6.39	0.91	89.87	0.55
7	2.94	0.53	6.50	0.95	77.81	11.10
8	2.66	0.51	8.30	1.06	74.98	12.01
9	5.25	0.29	25.71	1.05	67.68	0.00
10	5.29	0.24	24.76	1.71	67.17	0.67
11	1.28	0.37	7.33	1.41	88.93	0.35
12	1.34	0.45	7.36	1.72	88.73	0.00

Table 5. Average chemical composition of the solid solution and eutectic formations of sample No. 3. Treatment parameters, wt. %

Spectrum number	C	Si	Cr	Fe	Nb
1	2.20	0.69	8.88	87.82	0.00
2	2.36	0.72	9.53	86.63	0.23
3	11.30	0.01	1.80	2.46	83.68
4	1.19	0.03	1.44	2.57	83.87
5	2.33	0.36	7.21	81.99	7.81
6	2.12	0.41	6.90	82.50	7.63
7	5.36	0.38	26.65	67.24	0.16
8	5.21	0.26	24.90	68.89	0.60
9	1.39	0.49	10.19	87.34	0.14
10	1.52	0.54	9.57	87.15	0.62

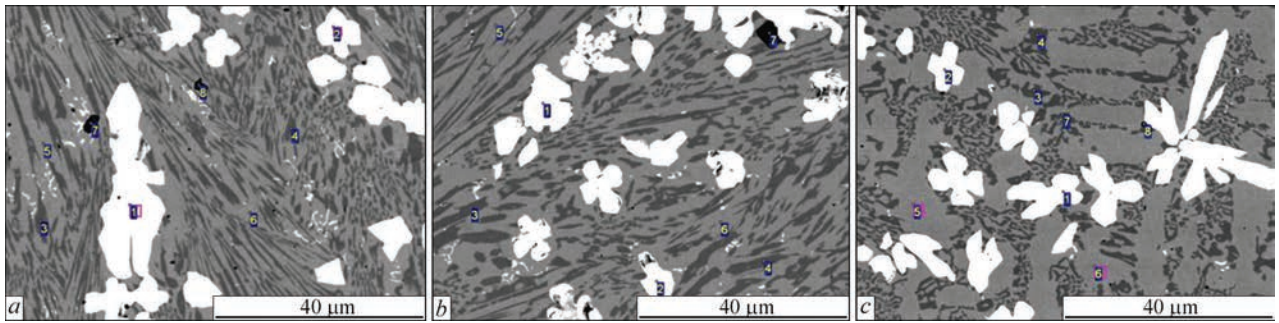


Figure 3. Electronic image of structural components of the deposited metal working zone: *a–c* — samples Nos 1–3, respectively

posited layer and average chemical composition of the structural components are shown in Figure 2 and in Tables 3–5.

Base metal influence in the transition zone and in first layer of the deposited metal is practically the same.

Deposited metal structures in the working zone (second layer), its electronic image and chemical composition of the structural components are shown in Figure 3, *a–c* and in Tables 6–8. Spectrum Nos 1,

2 is NbC; spectrum 3, 4 is $(Fe, Cr)_7C_3$; spectrum 5, 6 is the solid solution. A change of structure formation in samples No. 1 and 3 is found, depending on the change of the charge composition.

Distribution of alloying elements by the structural components in the deposited metal of the second layer is shown in Figure 4. Such structural components of the deposited metal with formation of carbides of a high hardness promote a considerable improvement of the quality of products operating under abrasive

Table 6. Chemical composition of structural components of the working zone (second layer) of sample No. 1. Treatment parameters, wt.%

Spectrum number	C	Si	Cr	Fe	Nb
1	11.56	0.10	0.75	1.34	85.30
2	10.80	0.04	1.60	1.04	85.66
3	8.53	0.00	58.21	32.61	0.56
4	8.70	0.00	57.38	33.17	0.40
5	1.12	0.96	15.22	81.66	0.41
6	1.22	1.25	13.50	83.37	0.17
7	1.12	0.12	0.64	2.10	0.00
8	1.16	0.12	0.73	1.70	0.30

Table 7. Chemical composition of structural components of the working zone (second layer) of sample No. 2. Treatment parameters, wt.%

Spectrum number	C	Si	Cr	Fe	Nb
1	11.21	0.08	2.44	0.54	84.45
2	11.67	0.02	2.18	1.30	83.89
3	8.70	0.00	58.59	31.93	0.72
4	8.58	0.06	57.57	33.35	0.17
5	1.26	1.11	14.12	82.54	0.21
6	1.42	1.15	13.70	82.95	0.13
7	–	0.35	3.08	11.80	1.89

Table 8. Chemical composition of structural components of the working zone (second layer) of sample No. 3. Treatment parameters, wt.%

Spectrum number	C	Si	Cr	Mn	Fe	Nb
1	10.89	0.00	1.33	0.55	0.95	85.00
2	10.68	0.10	1.97	0.00	1.60	84.04
3	8.67	0.06	49.19	0.00	41.28	0.31
4	8.29	0.02	48.02	1.07	41.91	0.24
5	1.87	0.91	13.06	0.78	82.03	0.00
6	1.65	1.05	13.23	0.27	82.07	0.20
7	–	0.09	4.55	7.62	5.99	0.00
8	–	0.00	0.81	1.68	2.28	0.00

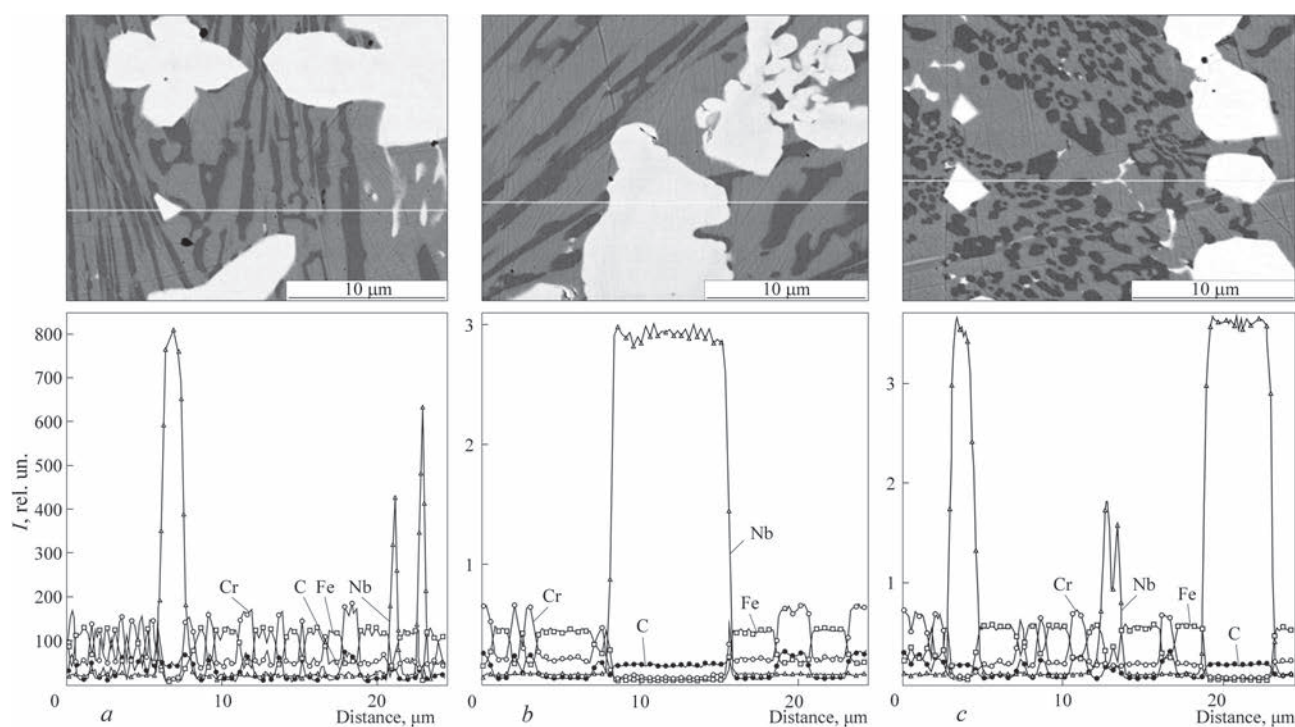


Figure 4. Linear distribution of C, Fe, Cr, Nb alloying elements by deposited metal structural components: *a-c* — samples Nos 1–3, respectively

wear conditions. At comparison of samples produced in different modes (Nos 1, 2) and in one mode, but with different composition of the charge (Nos 1, 3) may lead to the conclusion that weight fraction in the working zone increases from sample No. 1 to sample No. 3 by approximately 10–12 wt.%, and weight fraction of the carbide phase decreases. There is a change in structure formation: in samples Nos 1 and 2 the structure is an austenitic matrix with chaotically located Cr and Nb carbides of different shape. In sample No. 3 the crystallization structure is dendritic-cellular with $(\text{Fe, Cr})_7\text{C}_3$ carbides in the composition of the eutectic located on the cell boundaries and in the interdendritic space, and with niobium carbides of a different shape, randomly located in the entire height of the deposited layer. The degree of carbide alloying in samples Nos 1 and 2 is the practically the same, and in sample No. 3 it is somewhat higher (see Table 2).

DISCUSSION OF THE RESULTS

From the presented data, there is a decrease of the carbide component in absence of chromium carbide in the charge composition.

The weight fraction of phase components, crystalline lattice type and its parameters were determined, which were assessed by the method of X-ray diffraction analysis: $\gamma\text{-Fe}$ – 54.4; $(\text{Fe, Cr})_7\text{C}_3$ – 22.3; NbC – 17.3; Me_2C – 6.0 wt.% (surfacing with a strip of 16.5×4.0 mm cross-section); $\gamma\text{-Fe}$ – 57.2; $(\text{Fe, Cr})_7\text{C}_3$ – 23.2; NbC – 15.7; Me_2C – 3.8 wt.% (surfacing with a strip of 10.0×3.0 mm cross-section in lower

modes); $\gamma\text{-Fe}$ – 65.7; $(\text{Fe, Cr})_7\text{C}_3$ – 16.0; NbC – 15.9; Me_2C – 2.4 wt.% (complex carbide, containing iron and other carbide-forming elements, surfacing with flux-cored strip of 16.5×4.0 mm cross-section with chromium carbide replacement by high-carbon ferrochromium in the charge composition).

Integral hardness in height of the deposited layer changes gradually from base metal to the hardened layer surface in the range from 3700 to 6700–6900 MPa (samples Nos 1, 2) and from 3800 to 5400 MPa (sample No. 3) and it is leveled in the second layer of the deposited metal that corresponds to the change of chemical composition in integral curves of linear distribution of alloying elements.

Wear-resistant layer obtained using flux-cored strips of different cross-section and in different surfacing modes, practically does not differ by its characteristics. Replacement of chromium carbide by high-carbon ferrochromium in the charge composition reduces the amount of the carbide phase and integral hardness of hardened surface.

CONCLUSIONS

It is found that optimum concentration of the carbide phase in the metal deposited by flux-cored strip of PL-AN185 type, is reached due to addition of carbide-forming element — chromium to the electrode material charge in the form of chromium carbide. Replacement of chromium carbide by high-carbon ferrochromium in the charge composition leads to increase of austenitic component and decrease of in-

tegral microhardness of the deposited layer. In the deposited metal complex carbide systems (Cr, Fe)₇C₃ are predominantly present in all the samples. Niobium forms individual carbide components, which are uniformly arranged in the working zone and promotes formation of a finely-dispersed structure of the deposited layer.

REFERENCES

1. Ryabtsev, I.A., Senchenkov, I.K., Turyk, E.V. (2015) *Surfacing. Materials, technologies, mathematical modeling*. Gliwice, Wydawnictwo Politechniki Śląskiej.
2. Ryabtsev, I.A. (2005) High-efficiency wide-layer surfacing using electrode wires and strips. *The Paton Welding J.*, **6**, 36–41.
3. Pokhodnya, I.K., Shlepakov, V.N., Maksimov, S.Yu., Ryabtsev, I.A. (2010) Research and developments of the E.O.Paton Electric Welding Institute in the field of electric arc welding and surfacing using flux-cored wire (Review). *The Paton Welding J.*, **12**, 34–42.
4. Voronchuk, A.P., Zhudra, A.P., Petrov, A.V., Kochura, V.O. (1991) Influence of temperature on hardness and heat resistance of high-chromium cast irons deposited by flux-cored strips. *Avtomatich. Svarka*, **6**, 44–50 [in Russian].
5. Zhudra, A.P., Voronchuk, A.P. (2012) Cladding flux-cored strips (Review). *The Paton Welding J.*, **1**, 34–38.
6. Kuskov, Yu.M., Bogajchuk, I.L., Chernyak, Ya.P., Evdokimov, A.I. (2013) Electroslag surfacing of parts, made of high-chrome cast iron, using cast iron shot. *The Paton Welding J.*, **8**, 47–49.
7. Kuskov, Yu.M., Evdokimov, A.I. (2014) Electroslag surfacing of wear-resistant alloyed cast irons. *Uprochniyushchie Tekhnologii i Pokrytiya*, **10**, 21–24 [in Russian].
8. Livshits, L.S., Grinberg, N.A., Kurkumelli, E.G. (1969) *Fundamentals of alloying of deposited metal*. Moscow, Mashinostroenie [in Russian].
9. Kudinov, V.D., Filimonov, B.V., Shevnov, S.A., Netesa, I.V. (1985) Cladding by composite alloys of metallurgical equipment parts. *Avtomatich. Svarka*, **5**, 48–50 [in Russian].
10. Voronchuk, A.P. (2009) Effect of concentration of hard particles on gas-abrasive wear resistance of composite alloy. *The Paton Welding J.*, **8**, 43–44.
11. Zhudra, A.P., Voronchuk, A.P., Petrov, A.V., Kochura, V.O. (2012) Technology, equipment and materials for manufacturing of sheet lining elements. *Svarochn. Proizvodstvo*, **11**, 40–43 [in Russian].

CONFLICT OF INTEREST

The Authors declare no conflict of interest

CORRESPONDING AUTHOR

O.P. Voronchuk

E.O. Paton Electric Welding Institute of the NASU
11 Kazymyr Malevych Str., 03150, Kyiv, Ukraine.

E-mail: voronchuk@aranei.com

SUGGESTED CITATION

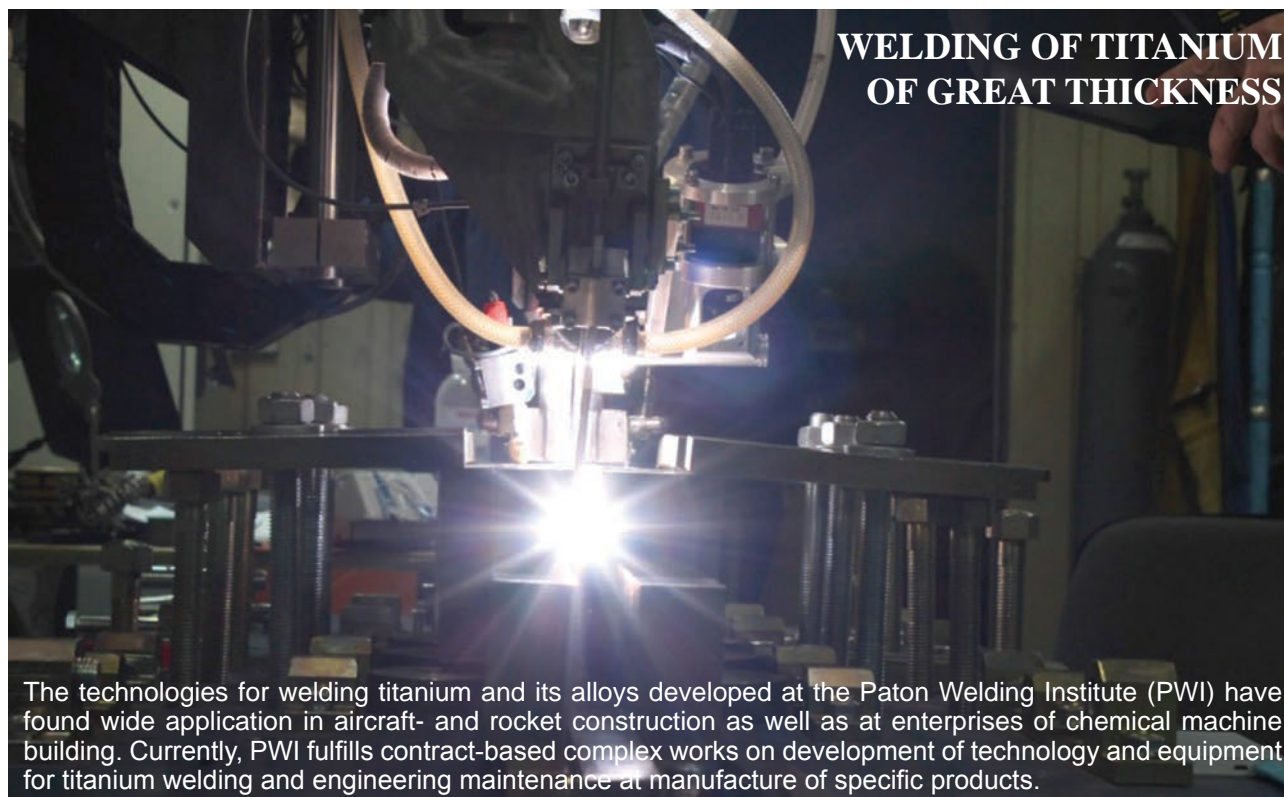
O.P. Voronchuk, O.P. Zhudra, T.V. Kaida, O.V. Petrov, L.M. Kapitanchuk, I.L. Bogaichuk (2022) Influence of the composition of charge components of flux-cored strips of C–Fe–Cr–Nb alloying system on chemical composition and structure of the deposited metal. *The Paton Welding J.*, **8**, 18–24.

JOURNAL HOME PAGE

<https://pwj.com.ua/en>

Received: 14.06.2022

Accepted: 17.10.2022



WELDING OF TITANIUM OF GREAT THICKNESS

The technologies for welding titanium and its alloys developed at the Paton Welding Institute (PWI) have found wide application in aircraft- and rocket construction as well as at enterprises of chemical machine building. Currently, PWI fulfills contract-based complex works on development of technology and equipment for titanium welding and engineering maintenance at manufacture of specific products.

DOI: <https://doi.org/10.37434/tpwj2022.08.04>

INVESTIGATION OF HEAT RESISTANCE OF PLASMA COATINGS FROM TiAl INTERMETALLIC WITH APPLICATION OF PARAMETRIC OXIDATION DIAGRAM

Yu.S. Borysov, A.L. Borysova, O.P. Gryshchenko, T.V. Tsymbalista, M.A. Vasylykivska

E.O. Paton Electric Welding Institute of the NASU
11 Kazymyr Malevych Str., 03150, Kyiv, Ukraine

ABSTRACT

Heat resistance of plasma coatings from TiAl intermetallic was studied by heating in air environment at temperatures of 700–1000 °C with determination of the change of sample weight and plotting of the parametric diagram of heat resistance, as well as phase composition of coatings before and after testing. It was determined that titanium oxide (TiO₂) is the main product of TiAl coating oxidation, and at higher temperatures it is a mixture of TiO₂ and Al₂O₃ oxides. Titanium nitride (TiN), TiO, Ti₂O, Ti₂O₃ oxides and Ti₃Al intermetallic were found in the scale composition. Kinetic dependencies of oxidation process were used to perform calculations of heat resistance parameters for temperatures of 700–1000 °C that allows assessment of durability of TiAl intermetallic coating for any temperatures up to 1000 °C. Calculations of average oxidation rate showed that heat resistance diagrams can be used to determine the main heat resistance characteristics: specific weight loss and uniform corrosion depth.

KEYWORDS: plasma spraying, intermetallics, Ti–Al system, heat resistance, oxidation, parametric diagram

INTRODUCTION

Intermetallics are a unique class of materials with a wide range of useful properties. Due to that they are used as structural alloys and coatings that ensure corrosion resistance.

As regards titanium intermetallics (TiAl, Ti₃Al), owing to such characteristics as high melting temperature, low density (two times lower than that of nickel-based superalloys (3.9–4.2 g/cm³)), high strength in a broad temperature range, higher creep resistance and fatigue strength, high modulus of elasticity and good oxidation resistance, they can compete with nickel-based superalloys in such industries as aviation and rocket technology.

So, application of titanium aluminide leads to lowering of part weight by 20–30 %, fuel consumption up to 20 %, noise by 50 % and NO_x emissions by 80 % [1]. TiAl intermetallics can be used as a protective material for titanium alloys, as it has higher oxidation resistance than the regular titanium alloys, and presence of an intermediate diffusion layer between the coating and base ensures good adhesion on the interface without brittle phase formation.

Titanium aluminides are promising for application in such industries as medicine, chemical and nuclear engineering, where such characteristics as corrosion and high-temperature resistance are of special importance, alongside other properties.

Analysis of published data [2–7] on heat resistance of TiAl intermetallic and alloys on its base indicate that the temperature range of their application is equal

to approximately 600–850 °C (at higher temperatures their mechanical properties and oxidation resistance are relatively low). It is known that limit operating temperatures of aluminium alloys are equal to 450 °C, and those of titanium alloys are 600–700 °C. At the same time, aluminium oxide Al₂O₃ has oxidation protection properties at up to 1425 °C.

Practically in all the works, devoted to investigation of oxidation processes of Ti–Al system intermetallics, there is a statement that TiO₂ titanium and Al₂O₃ aluminium oxides are the main oxidation products. Here, only Al₂O₃ is capable of forming a continuous film that slows down the oxidation process.

Predominant formation of Al₂O₃, compared with TiO₂ depends on Al content in the intermetallic, partial pressure of oxygen and temperature.

So, work [2] devoted to study of Al₃Ti and TiAl oxidation process shows that Al₃Ti oxidation stability at 1000 °C for 48 h is 30 times better than that of TiAl. At this moment TiAl loses Al, transforms into Ti₃Al on the interface of TiAl and scale, and Ti diffusion through an Al₂O₃ layer and TiO₂ formation only enhance TiAl oxidation.

As shown by the results of work [8] devoted to study of the influence of partial pressure of oxygen on oxidation of Ti–Al system intermetallics, at temperatures from room to 1000 °C predominantly Al₂O₃ forms already at very low pressure (5 mBar), and at increase of oxygen pressure TiO₂ formation becomes the predominant process. At 1000 °C new oxide phase forms namely Al₂TiO₅.

The main factor that limits TiAl application area is the fact that this alloy has poor oxidation resistance at temperature above 800 °C, as the outer layer of oxide scale consists of TiO_2 , or a mixture of TiO_2 and Al_2O_3 oxides, but not of Al_2O_3 protective layer. Owing to close affinity of Ti and Al to oxygen, TiO_2 and Al_2O_3 oxides grow competitively at the same rate on TiAl surface during oxidation that is confirmed by Ti–Al–O constitutional diagram [7, 8]. Mixed scale cannot prevent further oxidation of TiAl, that is why TiAl has a lower oxidation resistance at high temperatures.

More over, at oxidation in air titanium simultaneously reacts with oxygen and nitrogen. Nitrogen dissolution in rutile lattice leads to formation of a defective lattice, acceleration of oxygen diffusion and increase of oxidation rate. Formation of titanium nitrides in air prevents appearance of Al_2O_3 protective layer [9].

As regards the work in the field of technology and application of protective coatings based on Ti–Al intermetallic system, they are not very numerous. Known are only studies of producing coatings by magnetron sputtering. So, authors of work [4], produced good quality coatings from TiAl_2 , which demonstrated a high resistance at temperatures of 800–900 °C at oxidation in air. Work [3] presents the results of producing gradient and multilayer coatings, using magnetron sputtering. Here, in gradient coatings Al content increased in the direction from the base to the surface, and in multilayer coatings the layers formed in the same direction from Ti_3Al towards TiAl and TiAl_3 . Coatings showed good oxidation resistance at the temperature of 750 °C.

While the mechanism of interaction of TiAl system intermetallics with oxygen is quite well studied, the information on heat resistance of these materials in the form of protective coatings is scarce, and especially the works on assessment of their life prediction are not available now.

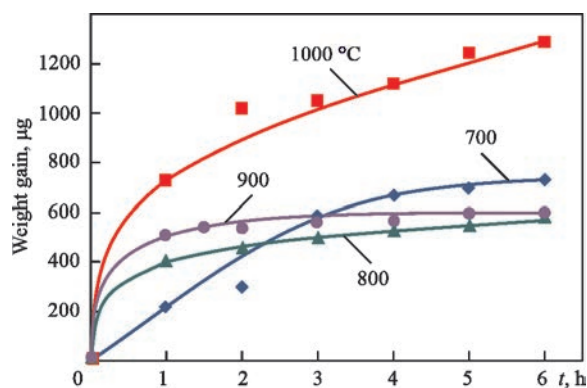


Figure 1. Kinetic dependencies of oxidation of TiAl powder

At the same time, the task of studying the coating heat resistance consists not only in evaluation of the coating role in base metal protection, but also in prediction of the service life of metal-protective coating system under the real service conditions.

The objective of this work was investigation of heat resistance of plasma coatings from TiAl intermetallics and plotting parametric diagrams of oxidation to assess the coating life at up to 1000 °C temperatures.

INVESTIGATION PROCEDURE

TiAl powder (PVT65Yu35 alloy) with particle size of $\leq 80 \mu\text{m}$ was used to produce coated samples.

Plasma spraying (PS) of coatings was performed in UPU-8M unit at the following parameters: $I = 500 \text{ A}$; $U = 40 \text{ V}$, plasma gas ($\text{Al} + \text{N}_2$) flow rate — 25 l/min, $L = 120 \text{ mm}$.

In order to study the coating heat resistance, samples were made from St45 grade steel in the form of “acorns” of 15 mm diameter and 20 mm length (coating thickness was 700–800 μm).

Investigations of heat resistance of both the powders and coatings were conducted by continuous welding of samples at temperatures of 700–1000 °C and isothermal soaking of up to 6 h.

Weight method (sample weight gain) was selected in connection with the fact that only solid products can form at oxidation of Ti–Al system samples.

The high-temperature testing unit allowed weighing the tested samples directly in the furnace, as it is fitted with analytical scales, from one arm of which the sample is suspended on a thin platinum wire. The unit had automatic regulation of temperature with the accuracy of $\pm 5 \text{ }^\circ\text{C}$, analytical scales ensured the accuracy of up to $\pm 0.1 \text{ mg}$.

Coating structure and phase composition were studied by the methods of metallography (Neophot-32 microscope fitted with digital camera attachment). X-ray diffraction phase analysis (XRPD) was performed in DRON-3 diffractometer in CuK_α -radiation with a graphite monochromator with 0.1° stepping and 4 s exposure time in each point with further computer processing of digital data. Phase identification was performed using ASTM data base.

EXPERIMENTAL RESULTS AND THEIR DISCUSSION

Analysis of kinetic dependencies of the process of TiAl powder oxidation revealed that in the entire temperature range of 700–1000 °C the process obeys the time parabolic law with parabola exponent close to 2, that is indicative of the fact that the diffusion stage is the limiting link of the process (Figure 1). Here,

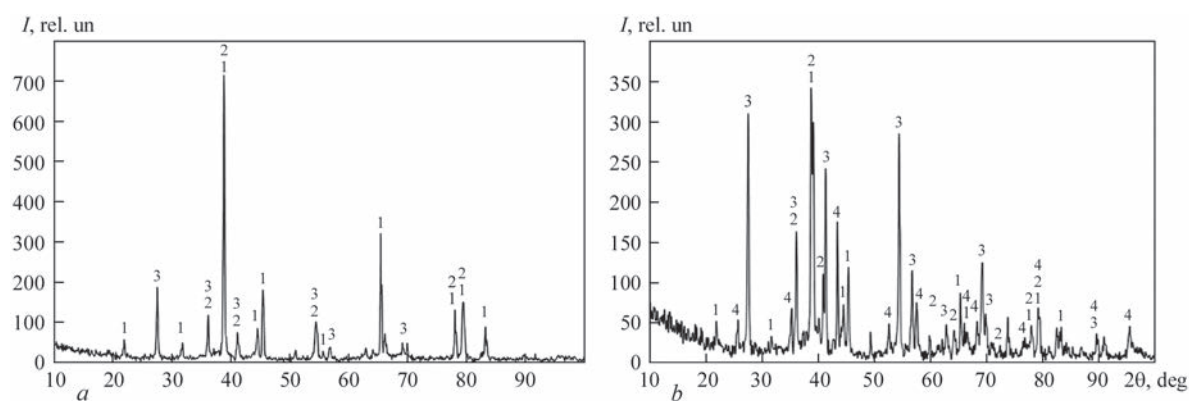


Figure 2. Roentgenograms of TiAl powder after oxidation at the following temperatures, °C: *a* — 700; *b* — 800; 1 — TiAl; 2 — Ti_3Al ; 3 — TiO_2 ; 4 — Al_2O_3

TiO_2 titanium oxide is the main product of oxidation of TiAl powder at the temperature of 700 °C, and at 800 °C and higher temperatures Al_2O_3 forms in addition to TiO_2 (Figure 2).

The processes of oxidation of plasma coatings and powders are described by parabolic dependence (Figure 3). However, the speed of process development is considerably higher in the first case (see Figure 1), which is attributable to the size of the surface in contact with oxygen.

Comparison of phase composition of coatings after heat resistance testing with as-deposited coatings (Figure 4) showed that oxidation at all the temperatures leads to increase of the content of TiO_2 and TiN phases, which formed in the coating during spraying as a result of interaction of powder particles with air, present in the plasma jet. Moreover, TiO, Ti_2O , Ti_2O_3 titanium oxides were detected in oxidation products in small quantities, in addition to TiO_2 , similar to Al_2O_3 formation in the case of TiAl powder oxidation at temperatures above 800 °C. Quantity of TiO_2 oxide grows with temperature increase.

At metallographic analysis of coatings after heat resistance testing (Figure 5) it was found that coatings remain dense, without delamination from the base, and oxide film forms on their surface.

Note that the oxide film thickness becomes greater at temperature rise, and at 900 °C it has a clear two-layered structure.

As was earlier noted, investigation results showed that the rate of oxide layer growth on the powders and coatings from TiAl intermetallics is a diffusion-controlled process (parabolic oxidation, Figures 1, 5). Here, either metal cation diffusion through the oxide to the surface and their interaction with oxygen on oxide/gas, or oxygen anion diffusion inside through the oxide and their interaction with metal on metal/oxide. Judging from the two-layer structure of the scale, a combination of both the processes is in place here.

One of the important characteristics of the protective heat-resistant coatings is prediction of their service life. Such a prediction can be made by plotting the parametric diagrams of heat resistance [10, 11].

Parametric diagram of heat resistance is the dependence of coating material weight loss (gain) at oxidation on heat resistance. Heat resistance parameter is a physical quantity, which changes in time with the rate proportional (with an opposite sign) to the true rate of oxidation of coating material, calculated by the values of relative losses (gain) of its weight.

The procedure for plotting the parametric diagrams consists in determination of n and Q values, where n is the exponent of parabolic dependence of oxidation process, Q is the activation energy.

Exponent n is determined from the experimental kinetic dependence of specific weight gain (loss) q on time t :

$$q^n = K \cdot t,$$

where K is the constant of oxidation rate, which transforms into the following linear dependence when plotted in “ $\lg q - \lg t$ ” logarithmic coordinates:

$$n \lg q = \lg K + \lg t \text{ or } \lg q = 1/n \lg K + 1/n \lg t.$$

Hence, $n = \text{ctg } \alpha$ in time– $\Delta m/s$, mg/cm^2 coordinates, where α is the angle of inclination of a straight line to abscissa axis or it can be calculated by the following formula:

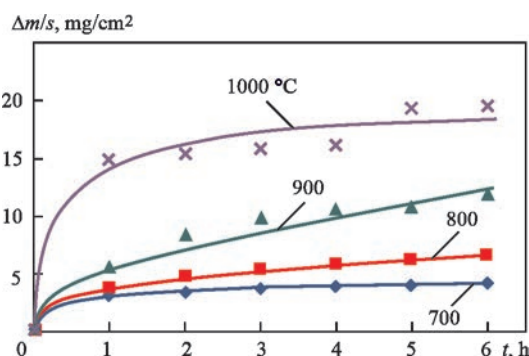


Figure 3. Kinetic dependencies of plasma coating oxidation

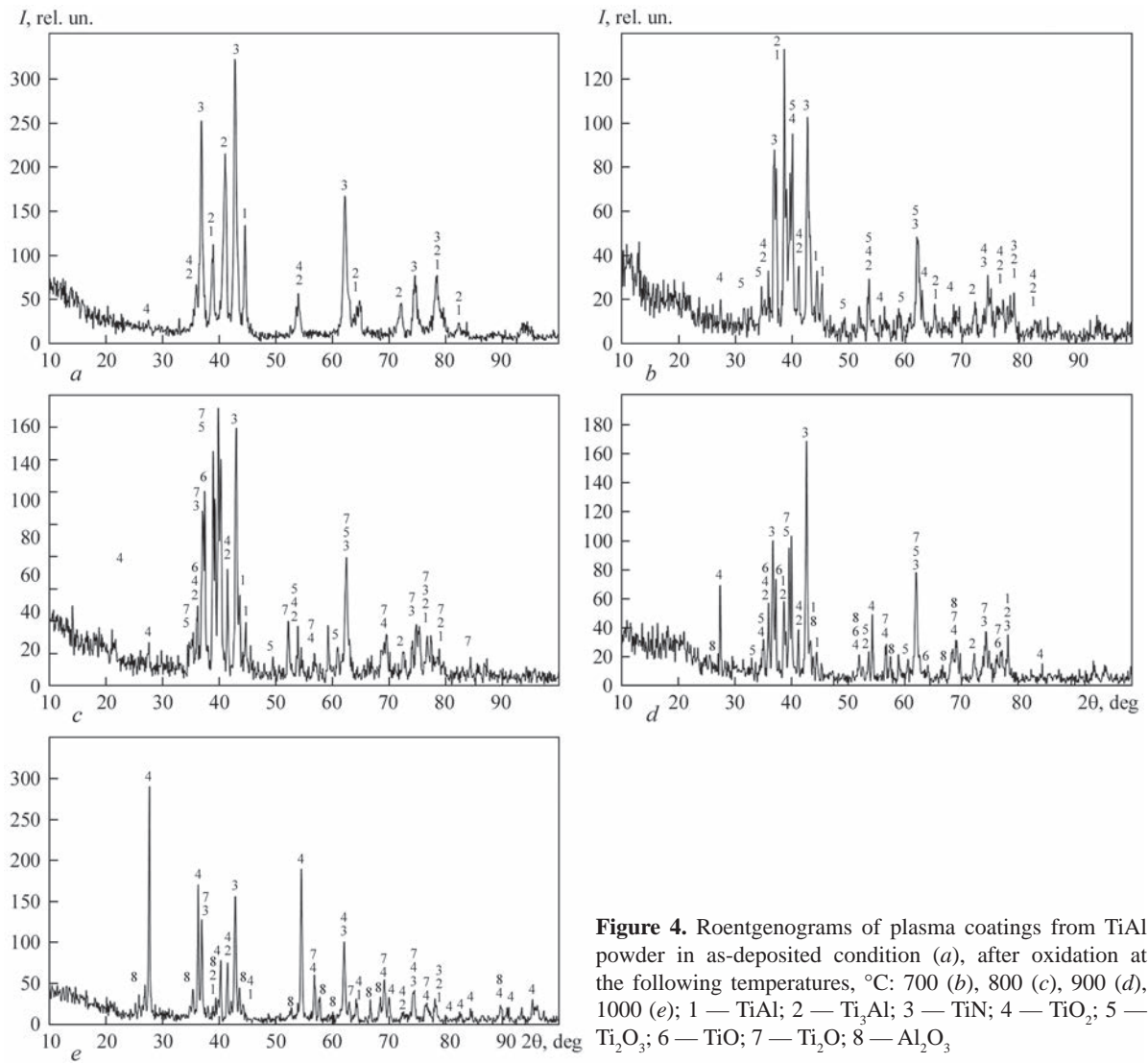


Figure 4. Roentgenograms of plasma coatings from TiAl powder in as-deposited condition (a), after oxidation at the following temperatures, °C: 700 (b), 800 (c), 900 (d), 1000 (e); 1 — TiAl; 2 — Ti_3Al ; 3 — TiN; 4 — TiO_2 ; 5 — Ti_2O_3 ; 6 — TiO; 7 — Ti_2O ; 8 — Al_2O_3

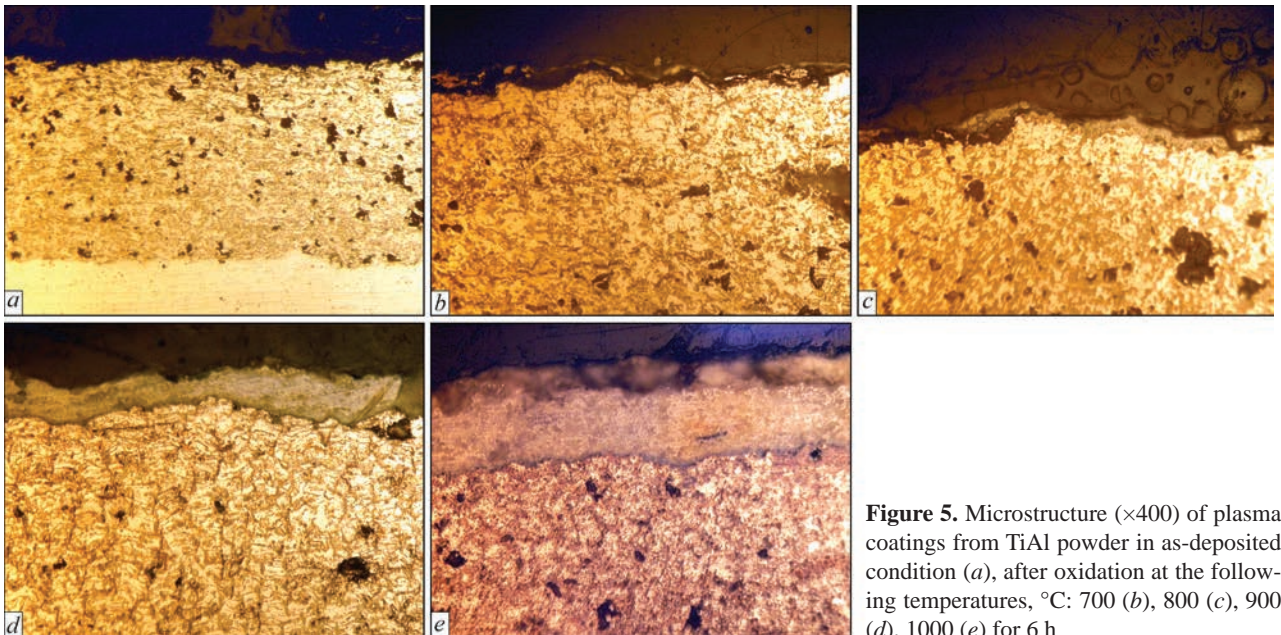


Figure 5. Microstructure ($\times 400$) of plasma coatings from TiAl powder in as-deposited condition (a), after oxidation at the following temperatures, °C: 700 (b), 800 (c), 900 (d), 1000 (e) for 6 h

Table 1. Results of calculation of the parameters of plasma coating heat resistance

Temperature, K	$10^3/T, 1/K$	Oxidation time, h	$\lg t$	Specific weight gain, mg/cm ²	$\lg q$	$(Q\lg e)/RT$	Heat resistance parameter, (P)
973	1.027	1	0	3.185	0.503	11.986	11.986
		2	0.301	3.450	0.538		11.685
		3	0.477	3.715	0.570		11.509
		4	0.602	3.842	0.584		11.384
		5	0.699	4.057	0.608		11.287
		6	0.778	4.234	0.627		11.208
1073	0.932	1	0	3.740	0.572	10.869	10.869
		2	0.301	4.805	0.682		10.568
		3	0.477	5.446	0.736		10.392
		4	0.602	5.940	0.770		10.267
		5	0.699	6.320	0.800		10.170
		6	0.778	6.680	0.825		10.091
1173	0.852	1	0	5.674	0.754	9.925	9.925
		2	0.301	8.468	0.928		9.624
		3	0.477	10.00	1.000		9.448
		4	0.602	10.58	1.025		9.323
		5	0.699	10.858	1.036		9.226
		6	0.778	11.862	1.074		9.147
1273	0.785	1	0	14.887	1.173	9.16	9.160
		2	0.301	15.42	1.188		8.860
		3	0.477	15.84	1.200		8.684
		4	0.602	16.18	1.209		8.560
		5	0.699	19.40	1.288		8.462
		6	0.778	19.63	1.293		8.383

$$n = \lg \frac{t_2}{t_1} / \lg \frac{q_2}{q_1}, \quad (1)$$

where t_1, t_2 are the two values of time (h) on the kinetic dependence which are quite far apart; q_1 and q_2 are specific gains (losses) of the coating weight (g/cm²) during the oxidation time, which correspond to t_1 and t_2 values.

Accuracy of calculation of exponent n by formula (1) is the higher, the greater the distance between t_1 and t_2 values.

Activation energy of the oxidation process (Q) is determined using temperature dependence $K = K_0 \cdot \exp(-Q/RT)$ through the tangent of φ angle formed by a straight line on $\lg q - 1/T$ graph after taking the logarithm: $\lg K = \lg K(-Q/RT) \lg e$.

Activation energy can be calculated also by the following formula:

$$Q = \frac{n \lg q_2 / q_1 \cdot R}{\lg e \left(\frac{1}{T_1} - \frac{1}{T_2} \right)}, \quad (2)$$

where e is the base of natural logarithms; R is the universal gas constant; T_1 and T_2 are temperature values, K , rather far apart in $\lg q - 1/T$ plot; q_1, q_2 are the specific weight gains (losses) which correspond to temperature values T_1 and T_2 .

Similar to calculation of n value in this case it is recommended to select T_1 and T_2 values that are quite far apart.

Value of heat resistance parameter (P) is determined, proceeding from the value of activation energy of the coating oxidation process, calculated by formula (1) and (2), as well as using the results of tests conducted to derive $\lg q - \lg t$ and $\lg q - 1/T$ dependencies:

$$P = \frac{Q \lg e}{RT} - \lg t. \quad (3)$$

Results of calculation of heat resistance parameter based on investigation of kinetic dependencies of plasma coating oxidation process at 700–1000 °C temperatures are shown in Table 1.

Conducted studies allowed assessing the life of protective coatings for any temperatures up to 1000 °C by plotting the parametric heat resistance diagrams (Figure 6).

Parametric method allows calculation of the average rate of metal corrosion (oxidation) [12]. Specific weight loss (gain) and metal corrosion depth (film thickness) at the specified temperature and time of exposure in oxidizing environment can be determined by two methods. One of them is analytical which consists in the following: a parameter is calculated by formula (3), then an ordinate is drawn from the respective point on P axis of parametric diagram (Figure 6) up

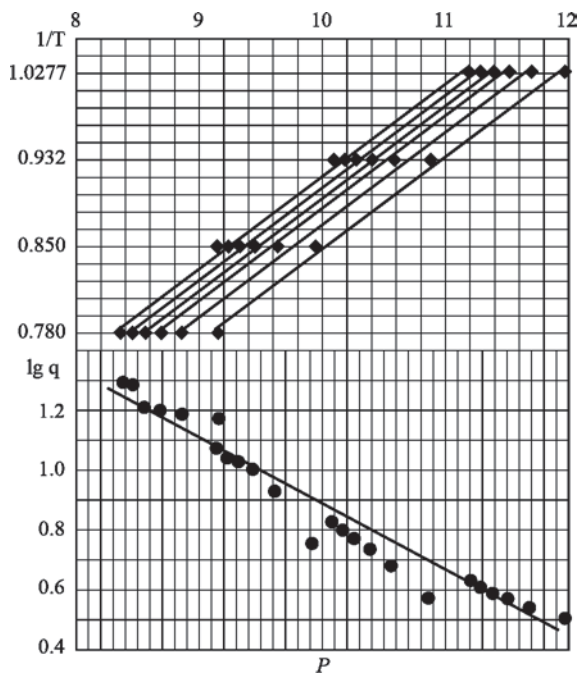


Figure 6. Combined parametric constitutional diagram of the plasma coating with nomogram

to crossing with the parametric line and an abscissa is drawn from their crossing point to $\lg q$ axis, where the sought value of weight gain (loss) or metal corrosion depth (film thickness) can be read. The specified values of metal oxidation time and temperature are used to determine by the parameteric diagram the value of weight loss (gain) or corrosion depth (film thickness). Then, $v = q/t$ ratio is used to determine the average rate of metal corrosion during the specified time. Here, it is assumed that oxidation starts when the metal has a clean surface, i.e. the metal does not oxidize up to the moment, when $t = 0$. If it is necessary to determine the average corrosion rate for time period $t_1 - t_2$, then first q_1 and q_2 values, corresponding to the beginning and end of this period, are found from the parametric diagram, and then the average rate is calculated by the following formula:

$$V_q = \frac{q_2 - q_1}{t_2 - t_1}. \quad (4)$$

The second method to determine the heat resistance characteristics is graphic. It is simpler so that it does not require any calculations. In this case, for convenience of using the parametric diagram, so as not to calculate the parameter values, the diagram is combined with $P - 1/T$ nomogram (Figure 6), and axes P of the nomogram and the diagram are parallel, have the same scale and the origins of coordinates on both the axes are located opposite each other. At simultaneous application of the diagram and the nomogram the heat resistance characteristics are determined by the calculated data of heat resistance parameter, finding

Table 2. Calculations of average corrosion (oxidation) rate of TiAl plasma coating using parametric diagram of heat resistance

Temperature, K	q_2	q_1	V_q
1023	5.52	4.52	0.25
1113	6.57	5.58	0.2475

first the specified temperature values on nomogram axis $1/T$, and then the specified time line on the nomogram, and only after them – the parameter (on diagram upper axis) and so on, as in the first case. All these operations are reduced to displacements on the nomogram and the diagram. As an example, Table 2 gives the calculation results for $t_1 = 1.5$ h, $t_2 = 5.5$ h.

CONCLUSIONS

1. Heat resistance of TiAl powders from PVT65Yu35 alloy and plasma coatings from it was studied by heating in an air environment up to 700–1000 °C with determination of sample weight change and plotting the parametric diagram of heat resistance.

2. As a result of analysis of kinetic dependencies of TiAl powder oxidation process it was found that the process obeys the parabolic law in the entire temperature range of 700–1000 °C, i.e. the limiting stage is diffusion. The main oxidation product at the temperature of 700 °C is TiO_2 titanium oxide, and at 800 °C and higher temperatures also Al_2O_3 aluminium oxide forms.

3. At coating oxidation in the studied temperature range, TiO_2 and Ti_2O_3 titanium oxides are found as additional phases. Quantity of TiO_2 oxide becomes greater with temperature increase.

4. Oxide film thickness at testing temperature rise is increased, and at 900 °C it has a clear two-layer structure that is indicative of the fact that during the diffusion process the oxide film forms both on metal-oxide and oxide-gas interfaces.

5. It is found that specific weight gain ($mg/cm^2 \cdot h$) was 0.18–0.62 and it increased up to 3.28 at 1000 °C.

6. Use of the plotted parametric diagram allows assessment of the life of TiAl-based coatings for any temperatures up to 1000 °C.

REFERENCES

1. Povarova, K.B., Antonova, A.V., Bannykh, I.O. (2003) High-temperature oxidation of TiAl-based alloys. *Metally*, **5**, 61–72 [in Russian].
2. Umakoshi Y., Yamaguchi M., Sakagami T., Yamane T.(1989) Oxidation resistance of intermetallic compounds Al_3Ti and TiAl. *J. of Materials Sci.*, **24**, 1599–1603.
3. Leyens C., Peters M., Kaysser W. (1997) Intermetallic Ti–Al coatings for protection of titanium alloys: Oxidation and mechanical behavior. *Surface and Coatings Technology*, **94–95**, 34–40.

4. Liu, Z., Wang, G. (2005) Isothermal oxidation behavior of Ti₃Al-based alloy at 700 and 1000 °C in air. *Materials Sci. and Engineering A*, **397**, 50–57.
5. Ostrovskaya, O., Badini, C., Baudana, G. et al. (2018) Thermogravimetric investigation on oxidation kinetics of complex Ti–Al alloys. *Intermetallics*, **93**, 244–250.
6. Dai J., Zhu J., Chen Ch., Weng F. (2018) High temperature oxidation behavior and research status of modifications on improving high temperature oxidation resistance of titanium alloys and titanium aluminides: A review. *J. of Alloys and Compounds*, **685**, 784–798.
7. Leyens, C., Peters, M., Kaysser, W.A. (1996) Influence of intermetallic Ti–Al coatings on the creep properties of bimetal 1100. *Scripta Materialia*, **35**(12), 1423–1428.
8. Das, K., Choudhury, P., Das, S. (2002) The Al–O–Ti (aluminum–oxygen–titanium) system. *J. of Phase Equilibria*, **23**(6), 525–536.
9. Ilatovskaia, M., Savinykh, G., Fabrichnaya, O. (2017) Thermodynamic description of the Ti–Al–O system based on experimental data. *J. Phase Equilib. Diffus.*, **38**, 175–184.
10. Nikitin, V.I. (1976) *Calculation of heat-resistance of metals*. Moscow, Metallurgiya [in Russian].
11. Gimelfarb, V.N. (1980) *Construction of parametric diagram of self-fluxing alloy oxidation*. Izvestiya AN BSSR [in Russian].
12. Nikitin, V.I. (1981) Method of service life prediction of protective coatings. *Fiz.-Khim. Mekhanika Materialov*, **3**, 95–99 [in Russian].

ORCID

Yu.S. Borysov: 0000-0002-6019-8464,
 A.L. Borysova: 0000-0002-7376-3370,
 O.P. Gryshchenko: 0000-0003-2640-8656,
 T.V. Tsymbalista: 0000-0001-9569-7776,
 M.A. Vasylykivska: 0000-0001-8311-6428

CONFLICT OF INTEREST

The Authors declare no conflict of interest

CORRESPONDING AUTHOR

T.V. Tsymbalista
 E.O. Paton Electric Welding Institute of the NASU
 11 Kazymyr Malevych Str., 03150, Kyiv, Ukraine.
 E-mail: tstania@gmail.com

SUGGESTED CITATION

Yu.S. Borysov, A.L. Borysova, O.P. Gryshchenko, T.V. Tsymbalista, M.A. Vasylykivska (2022) Investigation of heat resistance of plasma coatings from TiAl intermetallic with application of parametric oxidation diagram. *The Paton Welding J.*, **8**, 25–31.

JOURNAL HOME PAGE

<https://pwj.com.ua/en>

Received: 16.06.2022

Accepted: 17.10.2022

WORLD TRADE FAIR FOR WELDING-ENGINEERING —
 JOINING, CUTTING, SURFACING

LET'S JOIN
 THE WORLD!

11. – 15. September, 2023

REGISTER NOW!

www.schweissen-schneiden.com

SCHWEISSEN & SCHNEIDEN
 No. 1 IN THE WORLD

MESSE ESSEN

DVS GERMAN WELDING SOCIETY

DOI: <https://doi.org/10.37434/tpwj2022.08.05>

REACTIVE-FLUX BRAZING OF ALUMINIUM TO TITANIUM

O.M. Sabadash, S.V. Maksymova

E.O. Paton Electric Welding Institute of the NASU
11 Kazymyr Malevych Str., 03150, Kyiv, Ukraine

ABSTRACT

At brazing dissimilar joints of AD1 aluminium to VT1-0 titanium at the temperature of 605–610 °C by Al–12Si brazing filler metal in argon application of reactive flux of $KAlF_4$ – $10K_2SiF_6$ system with additives of CoF_2 , K_2ZrF_6 compounds, promotes production of a sound joint due to formation of a low-melting alloy of Al–Si system on the contact surface. The low-melting alloy of Al–Si system newly-formed at reactive-flux brazing can independently fulfill the function of brazing filler metal at formation of a dissimilar metal joint. Cobalt reduced from the flux has little influence on weld structure and joint strength. At application of Al–12Si brazing filler metal and reactive flux of $KAlF_4$ – $10K_2SiF_6$ – $5K_2ZrF_6$ system, which contains potassium-zirconium fluoride (K_2ZrF_6), a certain refinement of the structure (dendrites of aluminium-based solid solution) is observed from the aluminium side that promotes an improvement of shear strength of aluminium-titanium brazed joints.

KEYWORDS: aluminium, titanium, reactive-flux brazing, Al–Si brazing filler metal, reactive flux of KF – AlF_3 – K_2SiF_6 system, brazed joint

INTRODUCTION

Aluminium and titanium structures are optimal by strength/weight ratio, have high corrosion resistance and strength and are characterized by a wide spectrum of potential application in automotive and aerospace industry.

At present methods of welding and brazing of aluminium to titanium are actively developed. Their mechanically loaded joints are used in structures of various products. Formation of a sound joint of aluminium and titanium, as well as of their alloys is a complex problem, because of a considerable difference of physico-chemical properties of the metals (melting temperature, thermal expansion coefficient, heat conductivity, corrosion resistance), active interaction with gases (O_2 , N_2 , H_2), presence of a dense film from refractory oxides on the surface and ability to form brittle intermetallic compounds.

Effective application of electromagnetic radiation, filler material, joint configuration at laser braze-welding [1–6]; improvement of the geometrical shape of the rotating tool and optimization of its movement modes in friction stir welding [7–9] — this is an incomplete range of methods aimed at breaking up the highly stable oxide film, formation of a favourable weld structure and strong joint. At spot stir braze-welding (close to melting temperature of Zn–Al eutectic) of A2014 aluminium alloy and Ti6Al4V alloy application of a double coating (Al and Zn) on titanium increases (by 110 %) the shear strength of the joint [10], compared to the traditional technology.

High-temperature brazing in vacuum (purged by argon) by aluminium brazing filler metal below the critical temperature of titanium ($T < 800$ °C), alumin-

ium ($T < 630$ °C), and their alloys is the best choice as to the cost and preservation of mechanical properties of a joint of dissimilar metals [11–16]. Temperature limitation is due to undesirable changes of the microstructure and properties of both the thin-walled base metal and the joint: i.e. below $\alpha \leftrightarrow \beta$ -phase transformation in Ti [17, 18] and considerable loss of aluminium alloy strength at heating [19]. At titanium interaction with liquid aluminium and brazing filler metals (Al–Me systems (Me = Ag, Cu, Si), Al–Si–Cu, Al–Si–Mg) brittle intermetallic compounds form, which are close to $TiAl_3$ [20–22], Al_2Ti [23], and $Al_xSi_xTi_z$ [12, 14, 24, 25] by their stoichiometric composition, and whose interlayer has different influence on brazed joint strength. For instance, increase of soaking time ($t \leq 25$ min) at brazing temperature of 620 °C promotes an increase of the strength of Al/Ti joint brazed with Al–12Si–1Mg brazing filler metal [12]. At 620 °C temperature silicon diffusion from the brazing filler metal into Al results in isothermal crystallization of the solid solution, and a double layer from $Al_5Si_{12}Ti_7$, $Al_{12}Si_3Ti_5$ intermetallic compounds forms on titanium.

Prior application of an interlayer from (67Ag–33Al) alloy or (50Zn–50Al) coating on titanium at brazing by Al–Si brazing filler metal by immersion into the flux melt [26] and in vacuum [27] does not lead to any significant increase of shear strength ($\tau_{sh} \leq 40$ MPa) of Al/Ti joint.

Based on investigation results it was established that application of reactive flux of KF – AlF_3 – K_2SiF_6 salt system improves wetting and formation of the joint between the parts at brazing of aluminium alloys with low (≤ 0.7 wt.%) magnesium and aluminium content with steel [28–30]. At reactive-flux braz-

Table 1. Chemical composition of base materials and brazing filler metal, wt.%

Metal	Si	Fe	Cu	Mn	Mg	Cr	Ti	Al	O	N	H	C
AD1	0.15	0.30	0.30	0.05	0.02	0.05	0.10	99.3	–	–	–	–
VT1-0	0.1	0.15	–	–	–	–	–	–	0.2	0.04	0.01	0.07
AK12	10–13	<1.5	<0.6	<0.5	<0.1	<0.1Zn	<0.1	–84.3	–	–	–	–

ing active cleaning of the aluminium contact surface takes place, silicon is reduced from K_2SiF_6 compound in a short time, its content in the weld changes as a result of diffusion in the liquid state and properties of the joint of similar and dissimilar metals change accordingly.

Improvement of aluminium and titanium wetting by brazing filler metal at flux brazing, when their surface is covered by a strong refractory oxide film, and possibility of weld alloying by elements reduced from the reactive fluoride flux, are a factor in the formation of quality joints of components from dissimilar materials.

This work presents the results of studying the structure and strength of titanium-aluminium joint, formed with application of Al–12Si brazing filler metal and powder flux of $KF-AlF_3-K_2SiF_6$ salt system with CoF_2 , K_2ZrF_6 additives in temperature-time modes that were established for high-temperature brazing of aluminium in argon.

MATERIALS AND EXPERIMENTAL PROCEDURE

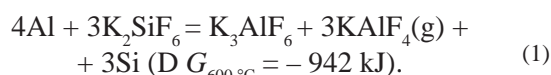
Experiments were performed using tee-samples ($40 \times 40 \times 1$ mm substrate, $40 \times 5 \times 1$ mm strip, assembled with a narrow gap of less than 0.1 mm) from AD1 aluminium alloy and VT1-0 titanium, AK12 brazing filler metal of Al–Si system (Table 1) and non-hygroscopic reactive fluxes: $KAIF_4-10K_2SiF_6$, $KAIF_4-10K_2SiF_6-CoF_2$, $KAIF_4-10K_2SiF_6-5K_2ZrF_6$.

Preparative synthesis method with application of reagents (hydrofluoric acid HF, $Al(OH)_3$ aluminium hydroxides and KOH potassium hydroxides and SiO_2 silicon oxide) were used to obtain $KAIF_4-10K_2SiF_6$ reactive flux. Reactive flux was mixed with addition of ready CoF_2 (ch.cl), K_2ZrF_6 (ch.cl) chemical compounds to produce the required compositions of homogeneous dispersed powder mixture. Before brazing metal samples were cleaned in water solutions of: 15 % NaOH and degreased, 20 vol.% HNO_3 , 2 vol.% HF and etched, and washed in distilled water between the operations. Tee-samples were assembled by placing a strip from aluminium alloy (titanium) on base metal substrate. Powder flux of ~ 0.06 g weight (in the sample upper zone) and a sample (0.17 g) of Al–12 Si aluminium brazing filler metal with flux (in the sample lower zone) were applied along the line of contact of the strip with base metal substrate. Flux brazing was performed at the temperature of $600-620 \pm 2$ °C

in pure argon atmosphere (vol.%): 99.987Ar, 0.002O₂, 0.01N₂, 0.001H₂O at dew point temperature $T = -58$ °C. Sample image was obtained with Panasonic FZ-30 digital camera. Brazed joint microstructure was studied using optical (Neophot-32) and scanning electron microscope (JSM840). Brazed joint strength was determined by tensile testing of overlap samples (two assembled plates of the following dimensions: 55 mm length, 15 mm width of the working part, 1.0 mm thickness) in R-5 tensile testing machine with maximum force of 50 kN. Mathematical processing methods with application of HSC 6.0 program were used for calculation of Gibbs energy.

INVESTIGATION RESULTS AND DISCUSSION

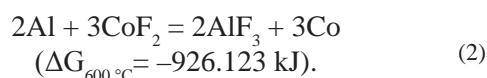
Based on calculations (using HSC 6.0 program) of the change of Gibbs free energy (ΔG) the nature of running of chemical reactions (1), (2) at aluminium interaction with chemical compounds (K_2SiF_6 , CoF_2) under the high-temperature conditions was determined as follows:



aluminium interaction with potassium hexafluoro-silicate (K_2SiF_6) by reaction (1) can result in silicon reduction in the composition of double fluoride is possible.

Conducted research of interaction of reactive flux of $KF-AlF_3-K_2SiF_6$ salt system on aluminium substrate (that is above the temperature of formation of Al–Si double eutectic) in high-purity argon atmosphere [31] showed that two processes proceed on aluminium surface: silicon reduction from the composition of potassium hexafluoride and contact-reactive melting of silicon with aluminium. Such an interaction results in formation of a metallic layer of Al–Si system, which improves the wetting and capillary properties of the brazing filler metal and can independently perform the function of brazing filler metal at narrow gap filling.

Proceeding from calculation results, under the brazing conditions cobalt can be reduced by aluminium from CoF_2 fluoride by the following reaction (2):



Balance of processes (1) and (2) is shifted completely towards the interaction products.

The sequence of chemical reactions (3) and (4) of potassium fluorozirconate (K_2ZrF_6) with aluminium occurring at high temperatures was studied in work [32]:



X-ray structural analysis confirms the appearance of $KAlF_4$, K_3AlF_6 , and Al_3Zr compounds in the products of reactions (3), (4). When brazing filler metal of Al–Si system is used, silicon interact with K_2ZrF_6 . Based on the results of X-ray diffraction analysis of the products obtained after vacuum heating of $K_2ZrF_6 + (Si)$ or $K_2ZrF_6 + (Al-7Si)$ mixtures at $700^\circ C$, showed that the reaction between K_2ZrF_6 and silicon does not take place [32]. At temperature modes of brazing, reduction (processes 1–3) of metals such as Si (conditionally referred to metals), Co, Zr by aluminium from K_2SiF_6 , CoF_2 , K_2ZrF_6 chemical compounds is possible.

Interaction in the heterogeneous system of “salt melt ($KF-AlF_3-K_2SiF_6$ flux) – metal alloy (Al–Si brazing filler metal) – solid metal (Al, Ti)” determines the nature of wetting and formation of a strong permanent joint by brazing filler metal at brazing.

Formation of brazed joint of AD1 alloy was studied using tee samples with AD1 alloy strip and Al–12Si brazing filler metal with flux placed in its lower zone, and just the flux applied in its upper zone (Figure 1, *a*). At heating of such a sample up to $605^\circ C$ temperature, filling of the gap takes place in the lower zone, its length reaching 40 mm (Figure 1, *b*), and in the upper zone (at application of just the flux) the gap is filled to length $L = 16$ mm (by newly-formed low-melting Al–Si alloy). Increase of soaking time to 16 s at heating of this sample leads to completion of the joint formation by newly-formed low-melting alloy of Al–Si system (Figure 1, *c*). Temperature rise from the moment of brazing filler metal melting is the

main factor for improvement of wetting and capillary properties of the brazing filler metal at the joint formation. High mutual solubility of molten brazing filler metal and newly-formed low-melting alloy, which belong to the same Al–Si metal system, has a positive influence on the kinetics of narrow gap filling.

Thus, proceeding from the conducted studies, the following sequence of running of the process of formation of aluminium brazed joint in argon was established: melt of flux of $KF-AlF_3-K_2SiF_6$ salt system wets and cleans the metal surface; new (cleaned) state of the surface activates the process of silicon reduction from the flux (by aluminium), further interaction of silicon with aluminium as a result of contact melting promotes formation of low-melting Al–Si alloy in the form of a continuous layer, which improves base metal wetting by the brazing filler metal. In the case of brazing filler metal absence the newly-formed alloy (Al–Si) under the impact of capillary forces fills the gap and its solidification takes place at cooling (Figure 1). In both the cases we obtain a sound brazed joint that differs only by the brazed seam width.

At aluminium brazing with titanium without using the brazing filler metal, heating up to the temperature of $585^\circ C$ also leads to silicon reduction from the flux on aluminium contact surface and formation of a low-melting alloy of Al–Si system, which improves wetting of both the base metals, and independently fulfills the function of brazing filler metal during brazing. Obtained sample of aluminium substrate with titanium strip demonstrates good filling of the capillary gap (Figure 2).

The difference of wetting of titanium substrate by aluminium filler of Al–Si system consists in that an interlayer of intermetallic compounds forms on the contact surface [20, 23].

Results of the conducted experiments showed that in order to achieve filling of the gap by brazing filler metal at brazing of titanium with aluminium and application of titanium as substrate (with just the flux), it is necessary

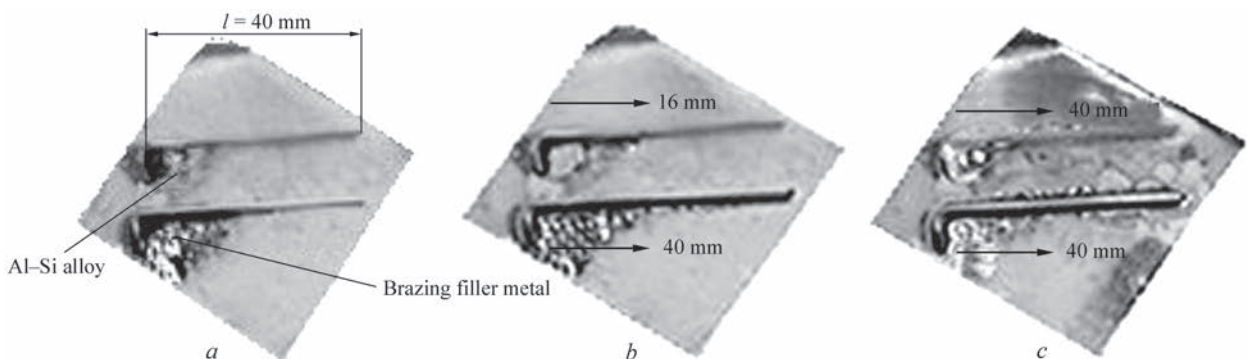


Figure 1. Appearance of a tee-sample with molten Al–12Si brazing filler metal and $KAlF_4-10K_2SiF_6$ flux after heating of an aluminium joint (AD1) up to the following temperature: *a* – $585^\circ C$, t_0 ; *b* – $605 \pm 2^\circ C$, $t = 8$ s; *c* – $605 \pm 2^\circ C$, $t = 16$ s

to raise the temperature and increase the soaking time by approximately 1.5–2.5 times (Figure 3).

Further increase of brazing temperature (by 5–7 °C) promotes formation of a joint of titanium substrate with aluminium strip, both using Al–12Si brazing filler metal, and without the filler, with application of $\text{KAlF}_4\text{--}10\text{K}_2\text{SiF}_6$ reactive flux.

Based on the conducted experiments, the temperature range ($T = 610 \pm 2$ °C) was determined for formation of a sound Al/Ti brazed joint (on Al and Ti substrate) in high-purity argon with 100 % filling of a narrow ($a \leq 0.1$ mm) gap at application of reactive $\text{KAlF}_4\text{--}10\text{K}_2\text{SiF}_6$ flux and Al–12Si brazing filler metal and at application of just the flux without using the brazing filler metal. Base metal brazing is conducted at temperature close to 0.95 of aluminium alloy solidus temperature, and further temperature rise can lead to complete softening, for instance, of thin-walled structure elements. Active running of the chemical reaction between the flux salt melt and base metal contact surface limits the time of soaking at brazing temperature.

Detailed study of microstructure of joints produced by reactive-flux brazing with brazing filler metal application demonstrated good weld formation (Figure 4). Samples were brazed in the same temperature-time modes: temperature of 610 ± 2 °C, soaking time $t = 30$ s. Based on the results of metallographic investigations it was found that at application of the brazing filler metal (Al–Si) and $\text{KAlF}_4\text{--}10\text{K}_2\text{SiF}_6$ flux the brazed seam structure consists of dendrites of aluminium-based solid solution ($\alpha\text{-Al}$), Al–Si eutectic (e), precipitating in interdendritic spaces and a

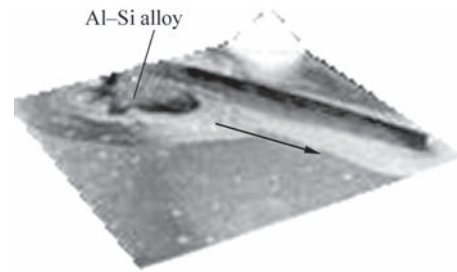


Figure 2. Appearance of a tee sample of AD1 (substrate)/VT1-0 (strip) with $\text{KAlF}_4\text{--}10\text{K}_2\text{SiF}_6$ flux without application of brazing filler metal after heating up to temperature of 605 ± 2 °C, $t = 18$ s in argon

continuous intermetallic layer (IML) on titanium of thickness $\delta = 8\text{--}10$ μm (Figure 4, *a*).

Local X-ray microprobe analysis revealed that silicon content in $\alpha\text{-Al}$ solid solution is equal to (0.54 %), and in the eutectic component it is (~12.8 %) at application of Al–Si brazing filler metal and $\text{KAlF}_4\text{--}10\text{K}_2\text{SiF}_6$ reactive flux. Intermetallic layer on titanium is formed by $\text{Ti}_{37.24}\text{Al}_{61.5}\text{Si}_{1.26}$ compound, which by its stoichiometric composition [20] is close to TiAl_3 phase (37.2 % Ti), containing a small silicon concentration.

In joints formed with reactive flux application without the brazing filler metal (Figure 4, *b*) a much smaller quantity of the eutectic component forms in thin interdendritic $\alpha\text{-Al}$ spaces and a thinning of the intermetallic layer to $\delta \leq 3$ μm is observed.

At application of Al–12Si brazing filler metal and $\text{KAlF}_4\text{--}10\text{K}_2\text{SiF}_6\text{--}2\text{CoF}_2$ reactive flux silicon content in the solid solution ($\alpha\text{-Al}$) and in the eutectic component almost does not change (Figure 5, *a*, Table 2).

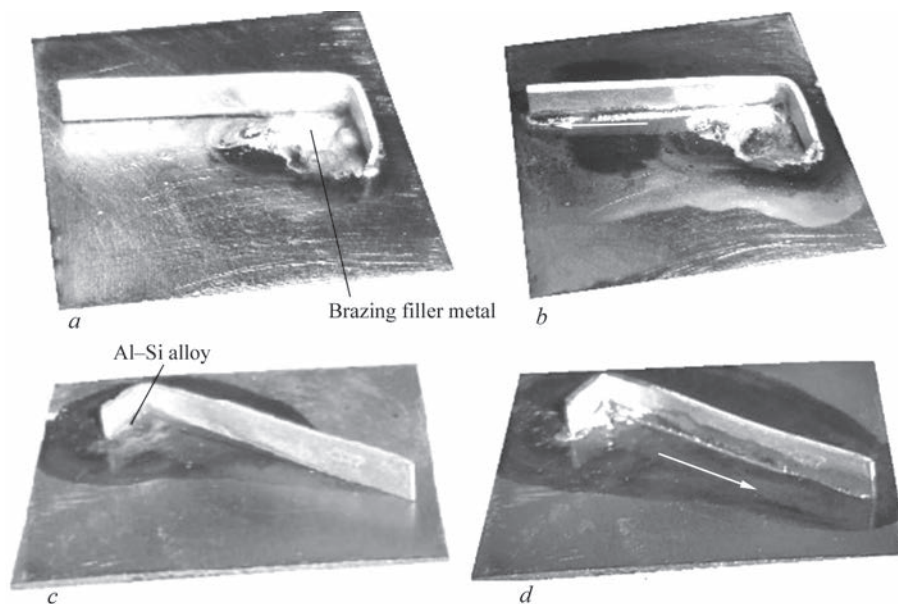


Figure 3. Appearance of a tee sample of VT1-0 (substrate)/AD1 (strip) with Al–12Si brazing filler metal and $\text{KAlF}_4\text{--}10\text{K}_2\text{SiF}_6$ flux after heating up to the temperature of 585 °C, t_0 (*a*); 610 ± 2 °C, $t = 26$ s (*b*) and without brazing filler metal application (585 °C, t_0) (*c*); after joint solidification (610 ± 2 °C, $t = 44$ s) (*d*) in argon

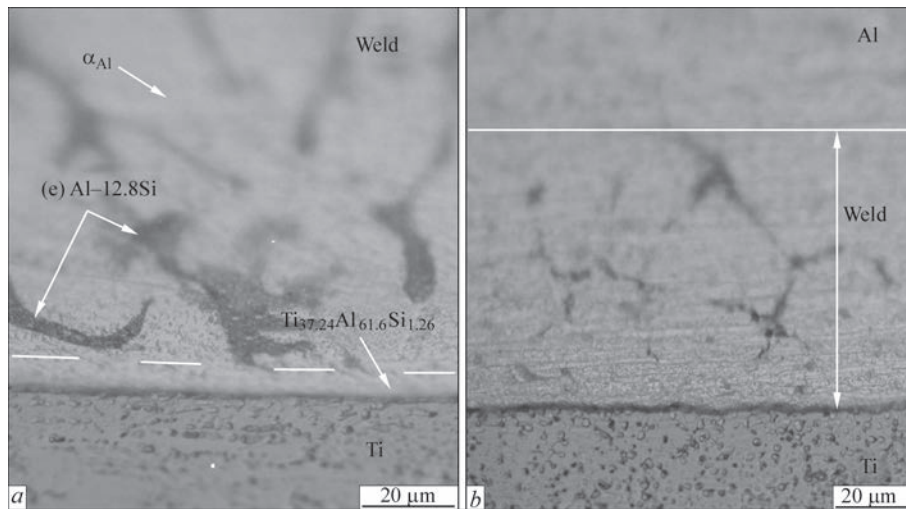


Figure 4. Microstructure of Al/Ti joint brazed with Al-12Si filler and $\text{KAlF}_4\text{-10K}_2\text{SiF}_6$ flux (a); without filler application, just with $\text{KAlF}_4\text{-10K}_2\text{SiF}_6$ flux (b)

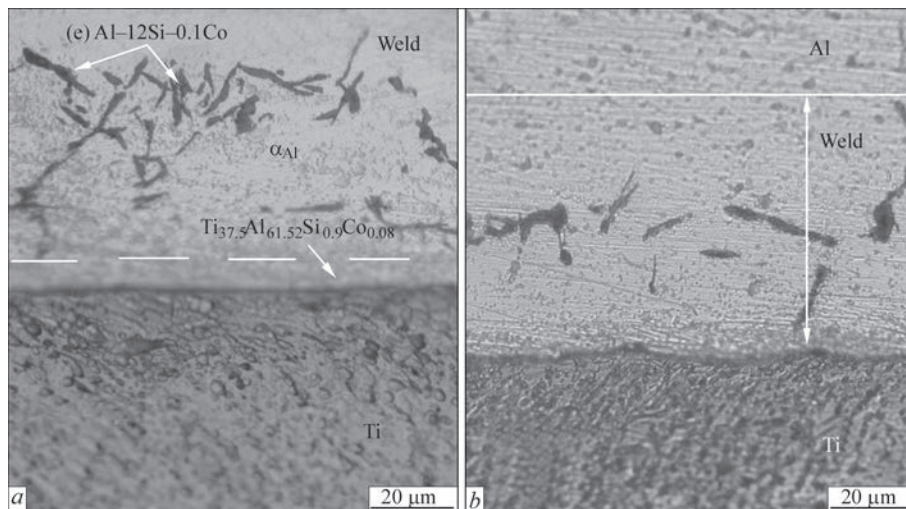


Figure 5. Microstructure of Al/Ti joint brazed by Al-12Si filler and $\text{KAlF}_4\text{-10K}_2\text{SiF}_6\text{-2CoF}_2$ flux (a), $\text{KAlF}_4\text{-10K}_2\text{SiF}_6\text{-2CoF}_2$ without filler application (b)

Cobalt content (0.10 wt.%) in the eutectic does not influence the dimensions of aluminium-based solid solution.

At application of Al-12Si brazing filler metal and $\text{KAlF}_4\text{-10K}_2\text{SiF}_6\text{-5K}_2\text{ZrF}_6$ reactive flux containing K_2ZrF_6 potassium-zirconium fluoride, silicon concentration in $\alpha\text{-Al}$ sol.s remains on the same level, and

in the eutectic component it decreases to 10.63 wt.% (Figure 6, a, Table 3).

Results of X-ray microprobe analysis showed that at application of $\text{KAlF}_4\text{-10K}_2\text{SiF}_6\text{-5K}_2\text{ZrF}_6$ flux, containing potassium-zirconium fluoride (IV) (K_2ZrF_6) there is 0.19 wt.% Zr in the eutectic component (Table 3). More over, certain refinement of dendrites of aluminium-based solid solution is observed (Figure 7).

The same effect of microstructure refinement is observed at alloying of eutectic alloy of Al-12.4Si system by zirconium (0–0.5 wt.%) [33]. Increase of the eutectic phase content up to 12 vol.% at zirconium alloying of the cast aluminium alloy and decrease of $\alpha\text{-Al}$ volume, respectively is shown in the case of Al-12.4Si-0.2Zr cast alloy, that promotes increase of tensile strength up to $\sigma_t = 100$ MPa [33].

Based on mechanical testing results it was found that at the temperature of 20 °C the maximum strength of overlap Al/Ti sample is equal to $\tau_{sh} = 61$ MPa at

Table 2. Chemical element content in Al/Ti brazed joint, wt.%

Component	Al	Si	Co	Ti
$\alpha\text{-Al}$ sol.s	99.46	0.53	0.01	0
(e)	87.9	12.0	0.10	0
IML (Ti)	61.52	0.9	0.08	37.5

Table 3. Chemical element content in Al/Ti brazed joint, wt.%

Component	Al	Si	Zr	Ti
$\alpha\text{-Al}$ sol.s	98.84	0.56	0.16	0
(e)	89.18	10.63	0.19	0
IML (Ti)	62.83	0.8	0.17	36.2

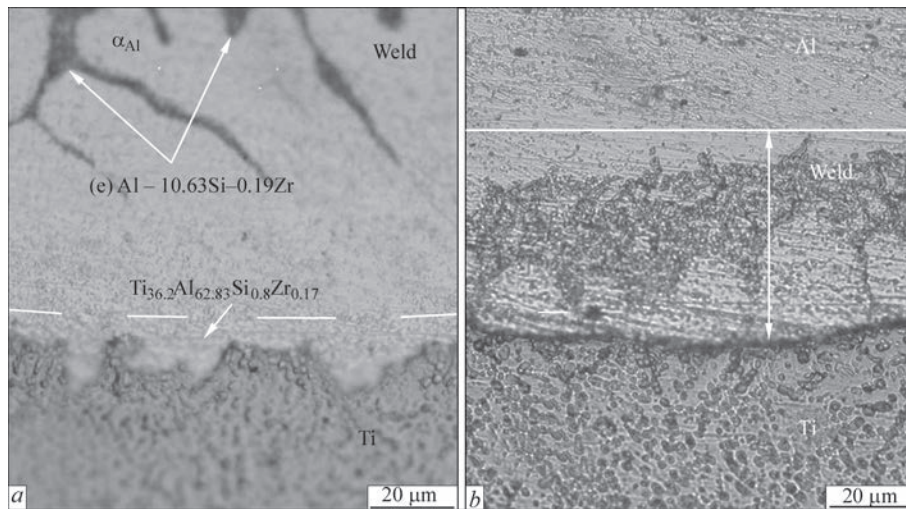


Figure 6. Microstructure of Al/Ti joint, brazed by Al-12Si filler and $\text{KAlF}_4\text{-}10\text{K}_2\text{SiF}_6\text{-}5\text{K}_2\text{ZrF}_6$ flux (a), $\text{KAlF}_4\text{-}10\text{K}_2\text{SiF}_6\text{-}5\text{K}_2\text{ZrF}_6$ flux without filler application (b)

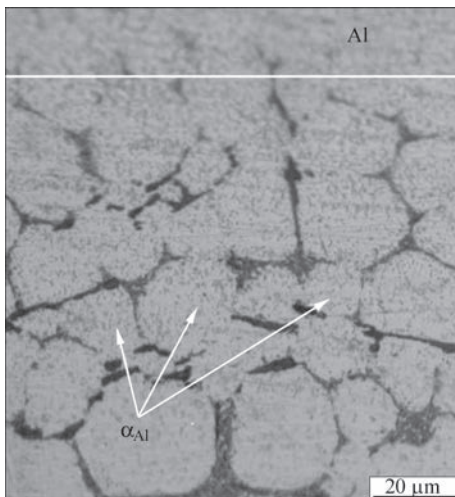


Figure 7. Microstructure of an area the weld of Al/Ti joint brazed with Al-12Si filler and $\text{KAlF}_4\text{-}10\text{K}_2\text{SiF}_6\text{-}5\text{K}_2\text{ZrF}_6$ flux

application of Al-12 % Si brazing filler metal and $\text{KAlF}_4\text{-}10\text{K}_2\text{SiF}_6\text{-}5\text{K}_2\text{ZrF}_6$ reactive flux (Figure 8).

CONCLUSIONS

1. At brazing different joints of AD1 aluminium with VT1-0 titanium by Al-12Si brazing filler metal, application of $\text{KF-AlF}_3\text{-}10\text{K}_2\text{SiF}_6$ reactive flux promotes cleaning of base metal surface and formation of a sound joint (at the temperature of 605–610 °C in argon).

2. At reactive-flux ($\text{KF-AlF}_3\text{-}10\text{K}_2\text{SiF}_6$) brazing of dissimilar aluminium-titanium joints without application of brazing filler metal, a low-melting alloy of Al-Si system forms on the aluminium contact surface at the temperature of 585–610 °C as a result of silicon reduction by aluminium from the flux. This alloy independently fulfills the function of brazing filler metal.

3. At application of Al-12Si brazing filler metal and $\text{KAlF}_4\text{-}10\text{K}_2\text{SiF}_6\text{-}5\text{K}_2\text{ZrF}_6$ reactive flux, which contains potassium-zirconium fluoride (IV) (K_2ZrF_6), a certain refinement of the structure (dendrites of al-

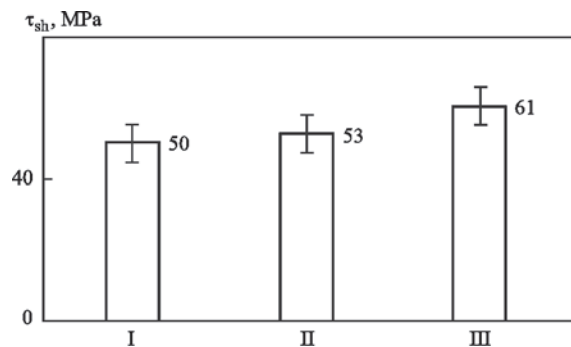


Figure 8. Strength of Al/Ti overlap joint brazed by Al-12Si filler using the following reactive fluxes: $\text{KAlF}_4\text{-}10\text{K}_2\text{SiF}_6$ (I), $\text{KAlF}_4\text{-}10\text{K}_2\text{SiF}_6\text{-}2\text{CoF}_2$ (II), $\text{KAlF}_4\text{-}10\text{K}_2\text{SiF}_6\text{-}5\text{K}_2\text{ZrF}_6$ (III)

uminium-based solid solution) of the brazed seam is observed from the aluminium side that improves an increase of shear strength of aluminium-titanium brazed joints.

REFERENCES

- Tomashchuk, I., Sallamand, P., Méasson, A. et al. (2017) Aluminium to titanium laser welding-brazing in V-shaped groove. *J. Materials Proc. Technology*, **245**, 24–36. DOI: <https://doi.org/10.1016/j.jmatprotec.02.009>
- Sahul, M., Sahul, M., Vyskoč, M. et al. (2017) Disk laser weld brazing of AW5083 aluminum alloy with titanium Grade 2. *J. Materials Eng. and Performance*, **26**(3), 1346–1357. DOI: <https://doi.org/10.1007/s11665-017-2529-6>
- Shelyagin, V.D., Bernatskiy, A.V., Berdnikova, O.M. et al. (2020) Effect of technological features of laser welding of titanium-aluminium structures on the microstructure formation of welded joints. *Metallophysics and Advanced Technologies*, **42**(3), 363–379. DOI: <https://doi.org/10.15407/mfint.42.03.0363>
- Dal, M., Peyre, P. (2017) Multiphysics simulation and experimental investigation of aluminum wettability on a titanium substrate for laser welding-brazing process. *Metals*, **7**(6), 218–232. DOI: <https://doi.org/10.3390/met7060218>
- Chen, Y., Chen, S., Li. (2010) Influence of interfacial reaction layer morphologies on crack initiation and propagation in Ti/Al joint by laser welding-brazing. *Materials and Design*, **31**, 227–233. DOI: <https://doi.org/10.1016/j.matdes.2009.06.029>

6. Zhou, X., Duan, J., Zhang, F., et al. (2019) The study on mechanical strength of titanium-aluminum dissimilar butt joints by laser welding-brazing process. *Materials*, **12**, 712–728. DOI: <https://doi.org/10.3390/ma12050712>
7. Choi, J.-W., Liu, H., Fujii, H. (2018) Dissimilar friction stir welding of pure Ti and pure Al. *Materials Sci. & Eng. A*, **730**, 168–176. DOI: <https://doi.org/10.1016/j.msea.2018.05.117>
8. Fall, A., Jahazia, M., Khodabandehb, A. (2016) Effect of process parameters on microstructure and mechanical properties of friction stir-welded Ti–6Al–4V joints. *Inter. J. of Advanced Manufacturing Technology*, **91(5–8)**, 2919–2931. DOI: <https://doi.org/10.1007/s00170-016-9527-y>
9. Yue, Y., Zhang, Z., Ji, S. (2018) Friction stir lap welding of 6061-T6 Al to Ti–6Al–4V using low rotating speed. *Inter. J. of Advanced Manufacturing Technology*, **96(5–8)**, 2285–2291. DOI: <https://doi.org/10.1007/s00170-018-1769-4>
10. Zhou, X., Chen, Y., Li, S. (2018) Friction stir spot welding-brazing of Al and hot-dip aluminized Ti alloy with Zn interlayer. *Metals*, **8**, 922–935. DOI: <https://doi.org/10.3390/met8110922>
11. Takemoto, T., Nakamura, H., Okamoto, I. (1990) Strength of titanium joints brazed with aluminum filler metals. *Transact. of JWRI*, **19(1)**, 45–49.
12. Sohn, W.H., Bong, H.H., Hong, S.H. (2003) Microstructure and bonding mechanism of Al/Ti bonded joint using Al–10Si–1Mg filler metal. *Material of Sci. Eng.*, **A355**, 231–240. DOI: [https://doi.org/10.1016/S0921-5093\(03\)00070-4](https://doi.org/10.1016/S0921-5093(03)00070-4)
13. Eckardt, T., Hanhold, B., Petrasek, D. (2012) Evaluating low-temperature brazing filler metals for joining titanium. *Welding J.*, **91(2)**, 45–50.
14. Khorunov, V.F., Voronov, V.V., Maksymova, S.V. (2012) Brazing of titanium alloys by using aluminium-base filler alloys. *Welding J.*, **11**, 2–5.
15. Voronov, V.V. (2013) Development of the technology for brazing of titanium alloys using filler alloys based on the Al–Mg system. *Welding J.*, **2**, 56–58.
16. Basude, A., Kumar, A., Rajasingh G. et al. (2022) Dissimilar joining of titanium alloy to aluminium using Al–Si based filler alloy by vacuum brazing technique. *Proc. IMechE Part L: J. of Materials: Design and Applications* **0(0)**1–14 DOI: <https://doi.org/10.1177/146442072211081951>
17. Leyens, C., Peters, M. (2003) *Titanium and titanium alloys. Fundamentals and applications*. Weinheim, WILEY-VCH Verlag GmbH & Co. KGaA.
18. Shapiro, A.E., Flom, Y.A. (2007) Brazing of titanium at temperatures below 800 °C: Review and prospective applications. *DVS-Berichte*, **243**, 254–267
19. Kaufman, J.G. (2008) *Parametric analyses of high-temperature data for aluminum alloys*. Ohio, ASM International® Materials Park.
20. Mondolfo, L.F. (1976) *Aluminum alloys: Structure and properties*. London, UK, Butterworths and Co., Ltd.
21. Takemoto, T., Okamoto, I. (1988) Intermetallic compounds formed during brazing of titanium with aluminium filler metals. *J. of Materials Sci.*, **23(4)**, 1301–1308.
22. Sujata, M., Bhargava, S., Sangal, S. (1997) On the formation of TiAl₃ during reaction between solid Ti and liquid Al. *J. of Materials Sci. Letters*, **16**, 1175–1178.
23. Ohnuma, I., Fujita, Y., Mitsui, H. (2000) Phase equilibria in the Ti–Al binary system. *Acta Materialia*, **48**, 3113–3123.
24. Liu, S., Weitzer, F., Schuster, C. J. et al. (2008) On the reaction scheme and liquidus surface in the ternary system Al–Si–Ti. *Inter. J. of Materials Research (formerly Z. Metallkde.)* **99**, 705–711.
25. Dezellusz, O., Gardiolaz, B., Andrieuxz, J. et al. (2014) On the liquid/solid phase equilibria in the Al-rich corner of the Al–Si–Ti ternary system. *J. of Phase Equilibria and Diffusion*, **35(2)**, 137–145. DOI: <https://doi.org/10.1007/s11669-014-0282-1>
26. (1979) *Aluminum Brazing Handbook*. Third Ed. New Washington, Aluminium Association.
27. Winiowski, A., Majewski, D. (2017) Brazing of titanium with aluminium alloys. *Archives of Metallurgy and Materials*, **62(2)**, 763–770.
28. Khorunov, V.F., Sabadash, O.M. (2013) *Brazing of aluminium and aluminium to steel*. Ch. 9. Ed. by Dušan P. Seculić. Advances in Brazing. Science Technology and Applications/Oxford-Cambridge Woodhead Publishing, England.
29. Khorunov, V.F., Sabadash, O.M. (2009) Reactive-flux brazing of aluminium to steel. *Welding & Material Testing*, **4**, 46–50.
30. Khorunov, V.F., Sabadash, O.M. (2013) Flux arc brazing of aluminium to galvanised steel. *The Paton Welding J.*, **2**, 31–36.
31. Sabadash, O.M., Maksymova, S.V. (2020) Formation and structure of Al–Si layer on contact surface of aluminium–reactive flux of KF–AlF₃–K₂SiF₆ system. *Metallophysics and Advanced Technologies*, **42(8)**, 1079–1092 [in Ukrainian]. DOI: <https://doi.org/10.15407/mfint.42.08.1079>
32. Rocher, J.P., Quenisset, J.M., Naslain, R. (1989) Wetting improvement of carbon or silicon carbide by aluminium alloys based on a K₂ZrF₆ surface treatment: Application to composite material casting. *J. of Materials Sci.*, **24(8)**, 2697–2703. DOI: <https://doi.org/10.1007/bf02385613>
33. Biswas, P., Patra, S., Kumar Mondal, M. (2020) Structure-property correlation of eutectic Al–12.4Si alloys with and without zirconium (Zr) addition. *Inter. J. of Cast Metals Research*, **33(2–3)**, 134–145. DOI: <https://doi.org/10.1080/13640461.2020.1769319>

ORCID

O.M. Sabadash: 0000-0003-0158-5760,
S.V. Maksymova: 0000-0002-9582-8673

CONFLICT OF INTEREST

The Authors declare no conflict of interest

CORRESPONDING AUTHOR

S.V. Maksymova
E.O. Paton Electric Welding Institute of the NASU
11 Kazymyr Malevych Str., 03150, Kyiv, Ukraine.
E-mail: maksymova@paton.kiev.ua

SUGGESTED CITATION

O.M. Sabadash, S.V. Maksymova (2022)
Reactive-flux brazing of aluminium to titanium. *The Paton Welding J.*, **8**, 32–38.

JOURNAL HOME PAGE

<https://pwj.com.ua/en>

Received: 04.07.2022
Accepted: 17.10.2022

DEVELOPMENT OF THE CoCrAlY/ZrO₂-8 % Y₂O₃ TYPE THERMAL BARRIER COATING BY SURFACE DOPING OF THE METAL LAYER WITH ALUMINIUM

K.Yu. Yakovchuk¹, G.P. Myalnytsya², A.V. Mykytchyk¹, Yu.E. Rudoy¹, R.O. Tkach¹

¹State-Run Enterprise «International Center for Electron Beam Technologies of the E.O. Paton Electric Welding Institute, NASU»

68 Antonovych Str. 03150, Kyiv, Ukraine

²State-Run Enterprise «Gas Turbine Research & Production Complex «Zorya»-«Mashproekt» 42-a Bohoyavlenskyi Prosp., 54018, Mykolayiv, Ukraine

ABSTRACT

The diffusion processes occurring at aluminium enrichment of the CoCrAlY overlayer during vacuum annealing from the slurry suspension applied to its surface and their influence on the structure, chemical composition and properties of CoCrAlY/ZrO₂-8 % Y₂O₃ coatings electron beam evaporated on nickel-based superalloy samples were studied. It is shown that the diffusion layer formed on the surface of the CoCrAlY alloy, enriched in aluminium, has a heterogeneous thickness and contains two microstructural zones with different aluminium content (external zone with aluminium up to 31 % and inner with aluminium up to 19 %). It was found that during vacuum heat treatment, cobalt and chromium diffuse into the slurry layer. As a result, microhardness increases up to 9 GPa and microcracks that propagate into the CoCrAlY layer are formed. The parameters of low-temperature heat treatment, which provides the formation of a defect-free diffusion zone in CoCrAlY, are established. The obtained results allowed us to optimize the technology of CoCrAlY layer thermodiffusional aluminization from the slurry for CoCrAlY/ZrO₂-8 % Y₂O₃ coatings in order to increase the operating temperature of the turbine blades made of CM-88U and CM-93 superalloys.

KEYWORDS: electron beam physical vapor deposition, condensation in vacuum, thermal barrier coatings, nickel-based superalloy, CoCrAlY metal bond coat, thermodiffusional aluminization, aluminium, slurry, thermally grown Al₂O₃ oxide (TGO), ZrO₂-8 % Y₂O₃ ceramic layer, diffusion of elements

INTRODUCTION

Alloys of MCrAlY type (M—Ni, Co or their combination) are used as coatings or bond coat in MCrAlY/ZrO₂/ZrO₂-Y₂O₃ thermal barrier coatings for protection of blades of modern gas turbine engines (GTE) made of high-temperature alloys (HTA) from high-temperature oxidation and corrosion. Aluminium content in them is usually equal to 8–12 % (wt.% here and furtheron) and it provides formation of a surface layer of Al₂O₃-based scale (TGO — thermally grown oxide) at high temperature in operation [1, 2].

Improvement of the effectiveness of GTE operation is accompanied by increase of working temperature, which necessitates increase of oxidation resistance (high-temperature resistance) of MCrAlY metal. One of the possible directions of such an increase is saturation of the surface of metal layer from MCrAlY alloy by aluminium using various methods [2–6]. The simplest and most cost-effective of these methods is saturation by aluminium from the coatings or slurries by prior deposition on the metal layer surface of filler material in the form of a suspension, containing the required alloying elements, and performing further heat treatment [7, 8].

The objective of this study is optimization of the parameters of the process of thermodiffusional aluminization of the condensed CoCrAlY layer from the slurry with further heat treatment and deposition of ZrO₂-8 % Y₂O₃ ceramic layer by the method of electron beam evaporation and condensation in vacuum.

MATERIALS AND INVESTIGATION PROCEDURE

Deposition of CoCrAlY/ZrO₂-8 % Y₂O₃ thermal barrier coatings was conducted by electron beam evaporation and condensation in vacuum on samples (segments of airfoil of blades made from high-temperature nickel alloys of CM-88U and CM-93 type) by the serial multistage technology which is used in State-Run Enterprise «Gas Turbine Research & Production Complex «Zorya»-«Mashproekt».

At the first stage of coating deposition a CoAlY layer (composition of evaporation ingots in keeping with TU U 27.4-20113410.002–2001) was applied on the blades, which was followed by their vacuum heat treatment (HT).

At the second stage a layer of slurry was deposited on the surface of CoCrAlY layer by the method of atomization of liquid suspension of PMS-Yu composition (analog of Sermetel W suspension), which was

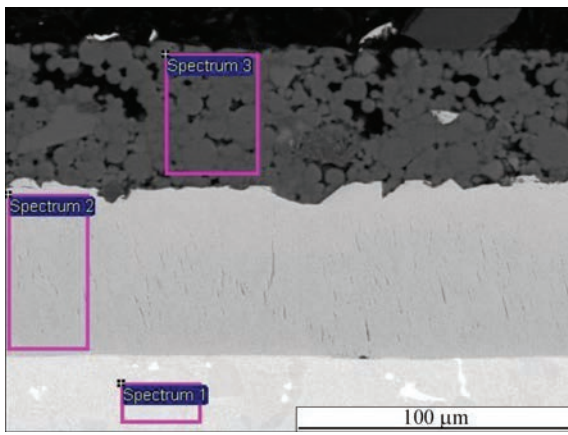


Figure 1. Microstructure and composition of CoCrAlY layer with PMS-Yu slurry on the surface after thermal setting

followed by thermal setting of the deposited slurry by drying at 350 °C.

At the third stage vacuum HT was performed for saturation of the surface of CoCrAlY layer by aluminium.

At the fourth stage air-abrasive treatment (AAT) by particles of abrasive from aluminium oxide was performed to remove the remains of slurry, and the outer ceramic layer of $ZrO_2-8\% Y_2O_3$ (8YSZ) was deposited on the blade airfoil surface.

Part of the blades after the second stage were transferred to SC “ICEBT of the E.O. Paton Electric Welding Institute of NASU” for further investigations and deposition of an outer ceramic layer.

The thickness of individual coating layers was determined in PolivarMet optical microscope. Microstructural studies and determination of microhardness of the coatings were conducted on samples in as-delivered condition and after heat treatment.

The structure of coating layers was studied using scanning microscope Carl Zeiss Sigma 300. The chemical composition was further determined using X-ray microprobe energy-dispersive attachment XMAX 50 for electron microscope.

Microhardness measurement was performed on transverse sections of the coatings using Micro-Duromat 4000 E attachment for Polyvar-Met optical microscope by standard Vickers indenter at 200 N load and exposure time of 10 s.

Thermal cycle life of CoCrAlY/8YSZ coatings on segments of blade airfoils was studied by the method of furnace testing in air by the following mode: heating up to 1100 °C temperature for 6 min, soaking for 50 min at this temperature, fan cooling to the tempera-

ture of approximately 60–80 °C for 4 min. Segments were examined after every twenty cycles. Coating failure was assumed to be outer ceramic layer delamination from 20 % of airfoil segment surface.

INVESTIGATION RESULTS AND THEIR DISCUSSION

Figure 1 and Table 1 give the microstructure and chemical composition of CoCrAlY layer with a layer of PMS-Yu slurry after thermal setting (after stage 2).

CoCrAlY layer contains about 22 % Cr and 11 % Al and a low content of yttrium (0.1 %), which is detected only in individual regions of the layer.

The layer of aluminium-based slurry has a porous microstructure, which contains predominantly spherical-like particles of 4–15 μm dia.

Thickness of CoCrAlY layer is equal to 55–65 μm, microhardness is on the level of 5.8 GPa, thickness of the deposited slurry layer varies in the range of 30–50 μm, and its microhardness is not higher than 0.7 GPa.

Further high-temperature HT in vacuum in the temperature range of 950–1100 °C for 0.5–1.0 h leads to formation of an aluminium-saturated diffusion layer on CoCrAlY surface (Figure 2, Table 2). This formed diffusion layer is of a heterogeneous thickness (20–40 μm) and it contains two zones with the characteristic microstructure and different aluminium content. Outer zone has grain structure, the size of globular particles of intermetallics of Co–(26–31) % Al–(9–14) % Cr composition is equal to 25–35 μm. It was found to contain numerous microcracks and pores, and its microhardness reaches 8.0–8.2 GPa. The inner zone contains 15–19 % aluminium, its microhardness is equal to approximately 6 GPa.

With increase of the duration of vacuum HT at 1100 °C up to 4 h, the total thickness of this diffusion layer increases by 15–20 μm (Figure 2, *a–j*). Aluminium content in the outer zone decreases from 31 to 25 %, and the globular particles of CoAlCr intermetallics do not significantly change their composition or dimensions. The inner zone, alongside an increase of its thickness to 10–15 μm, is saturated by aluminium due to its diffusion from the slurry and the outer zone, its content rising from 14.7 to 17.5 %. Here a decrease of total aluminium content in the volume of CoCrAlY layer (from 11 to 10 %) is also observed

Table 1. Chemical composition of CoCrAlY layer with PMS-Yu slurry on the surface after thermal setting, wt. %

Spectrum	O	Mg	Al	Si	P	Ti	Cr	Co	Ni	Y	Mo	W	Re
1	–	–	2.6	1.0	–	4.7	14.1	7.8	63.0	–	1.0	3.6	2.5
2	–	–	11.1	–	–	–	22.0	66.9	–	0.1	–	–	–
3	14.0	1.6	71.5	4.0	6.1	–	2.8	–	–	–	–	–	–

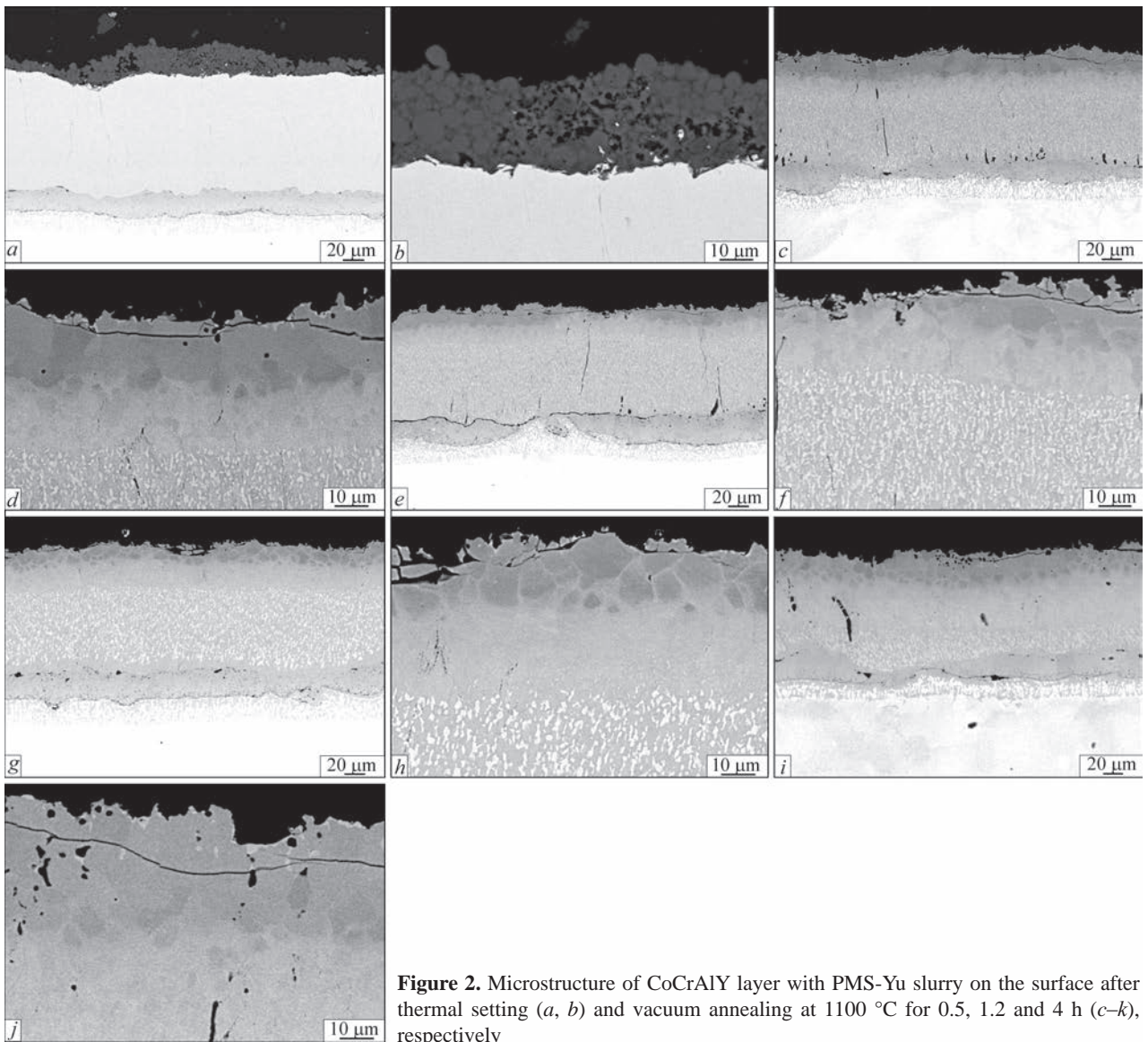


Figure 2. Microstructure of CoCrAlY layer with PMS-Yu slurry on the surface after thermal setting (*a, b*) and vacuum annealing at 1100 °C for 0.5, 1.2 and 4 h (*c-k*), respectively

that is attributable to its diffusion into the high-temperature alloy.

Lowering of vacuum HT temperature to 950 °C did not affect the forming defects. Microcracks form in the outer zone of CoCrAlY layer, which, as a rule, propagate parallel to the substrate (Figure 3).

The probable cause for microcrack appearance can be sintering of the slurry suspension during the process of high-temperature HT, resulting in increase of slurry layer microhardness to the level of 9 GPa. This is also promoted by cobalt (close to 41 %) and chromium (close to 8 %) diffusion into the slurry from CoCrAlY layer (Figure 3, Table 3). On the contact

boundary of the slurry, containing up to 50 % aluminium, and the surface of CoCrAlY layer, enriched in aluminium up to 30 %, stresses develop during cooling after HT, which lead to slurry cracking and crack propagation into the aluminium-enriched metal layer.

Attempts to remove the defective surface layer by intensive air-abrasive treatment before deposition of the outer ceramic layer did not yield the desirable result, either, and appearance of microcracks was observed on metal-ceramics interface (Figure 4).

As the thickness of the applied slurry suspension (it is applied in a layer of minimum possible thickness) cannot be reduced, it is rational to lower HT

Table 2. Composition (wt.%) and microhardness of CoCrAlY layer (GPa), depending on annealing time at 1100 °C

Zone of Al-saturated CoCrAlY layer	Initial		0.5 h		1 h		2 h		4 h	
	H_{μ}	Al								
Outer	–	–	8.8	31.2	8.2	31.0	7.6	28.2	6.5	25.5
Inner	–	–	6.4	14.7	6.2	16.3	7.0	16.0	6.9	17.5
Layer	6.0	12.0	5.3	10.7	5.7	11.5	6.1	10.6	6.5	9.9

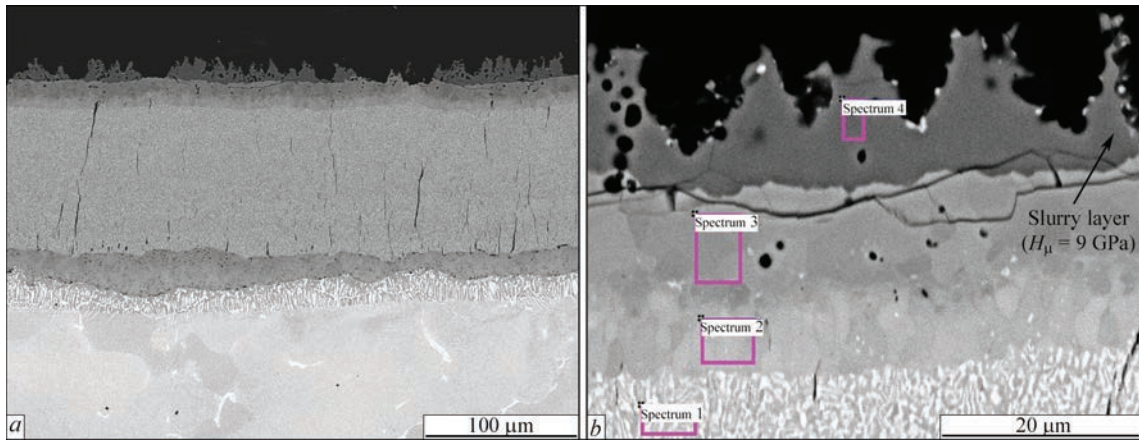


Figure 3. Microstructure (*a* — $\times 300$; *b* — $\times 1800$) of CoCrAlY layer after slurry deposition ($H_{\mu} = 9$ GPa) and vacuum HT at 950°C , 1 h temperature at stage 3 of coating deposition process so as to slow down both the diffusion processes of CoCrAlY layer saturation by aluminium, and the processes of sintering of the slurry layer. Here, diffusion interaction in slurry CoCrAlY layer system would occur only in a limited volume of the slurry, adjacent to the metal surface. It would allow lowering the aluminium content in the diffusion layer, the thickness of this layer and reducing the microhardness of sintered slurry (preventing microcrack initiation in it). After that, when performed further AAT, part of the slurry, which has not reacted and remained, will be removed for the surface of aluminium-saturated diffusion zone in CoCrAlY layer that will prevent its further saturation by aluminium.

In order to clarify the possibility of preventing such microcrack initiation in aluminium-saturated CoCrAlY layer, investigations were performed on the influence of temperature and time of heat treatment after slurry application (stage 3 – coating deposition).

Minimum HT temperature, at which no microcracks form during annealing in the range of $0.5\text{--}0.8$ h, was established (not higher than $700\text{--}750^{\circ}\text{C}$).

Figure 5 and in Table 4 give the microstructure and composition of CoCrAlY layer with deposited slur-

ry after high-temperature HT for 6 h. On the surface of CoCrAlY layer after HT the slurry layer contains three zones: outer of approximately $30\ \mu\text{m}$ thickness (slurry which did not react) with microhardness on the level of 0.65 GPa; middle of approximately $20\ \mu\text{m}$ thickness (sintered slurry) with microhardness on the level of 3.9 GPa; and diffusion of approximately $8\ \mu\text{m}$ thickness (microhardness is equal to 6.7 GPa), which is adjacent to the surface of CoCrAlY layer (microhardness of 6 GPa).

Aluminium content in the diffusion zone reaches 42.5% . Here, no microcrack formation was detected in the sintered slurry layer and in the diffusion zone.

Lowering of the temperature of vacuum HT allows: ensuring formation of aluminium-saturated diffusion zone of a more homogeneous thickness in CoCrAlY, due to aluminium coming not from the entire volume of slurry layer of heterogeneous thickness, but just from the slurry zone which is in direct contact with CoCrAlY surface; controlling both the thickness and content of aluminium in the diffusion zone owing to a change of HT time.

Here, selection of AAT mode parameters, ensuring removal of remains of the slurry mass from the diffusion layer surface after HT, is important.

After performance of stage 4 (deposition of 8YSZ layer) the diffusion zone thickness increased up to $15\ \mu\text{m}$, Al content was close to 21% and it gradually decreased to the level of 12% in CoCrAlY layer, and a TGO interlayer of approximately $1\ \mu\text{m}$ thickness was present between CoCrAlY layer and 8YSZ layer (Figure 6, Table 5).

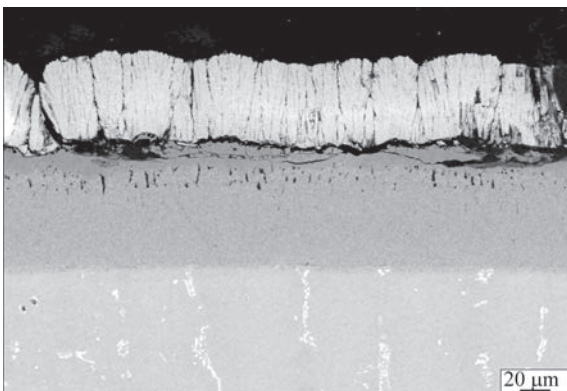


Figure 4. Microstructure of CoCrAlY/8YSZ coating after stages 1–4 of coating deposition (HT) in vacuum at the temperature of 950°C for 1 h)

Table 3. Composition of CoCrAlY layer with slurry after vacuum HT at 950°C , 1 h

Spectrum	Al	Cr	Co	Y
1	11.3	21.4	67.2	–
2	17.5	15.9	66.4	0.15
3	30.6	6.8	62.1	0.4
4	50.5	8.2	41.3	–

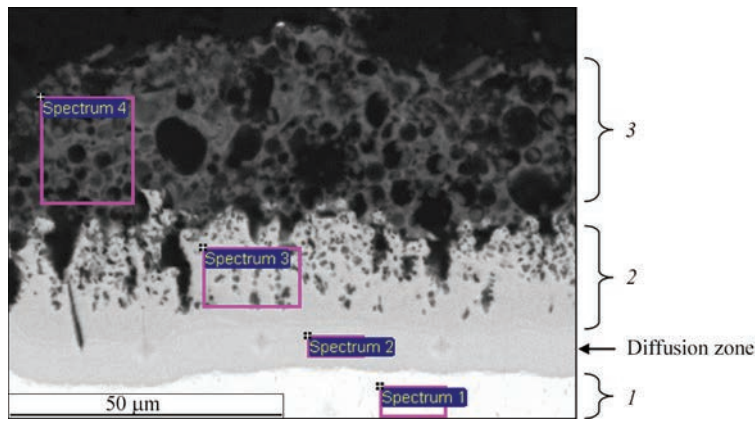


Figure 5. Microstructure and composition of CoCrAlY layer with PMS-Yu slurry on the surface after thermal setting and low-temperature HT for 6 h: 1 — CoCrAlY layer; 2 — sintered slurry layer; 3 — layer of slurry which did not react

Table 4. Chemical composition (wt.%) of CoCrAlY layer with PMS-Yu slurry on the surface after thermal setting and low-temperature HT for 6 h

Spectrum	O	Na	Mg	Al	Si	P	Cl	Ca	Cr	Co	Y
1	–	–	–	10.9	–	–	–	–	23.0	66.1	–
2	–	–	–	42.6	2.6	–	–	–	14.4	40.5	0.1
3	2.4	–	–	48.8	2.8	–	–	–	12.1	33.9	–
4	39.1	2.1	4.4	37.7	3.5	7.4	0.4	0.4	4.1	0.8	–

Changing HT time and temperature enables increasing the thickness of the diffusion zone, saturated by aluminium, to 40 μm, and reducing its aluminium content to 15–16 % (Figure 7, Table 6).

Performed thermal cycling testing of blade airfoil segments with CoCrAlY/8YSZ coating showed that slurry application improves the life by 25–30 %, due to a positive influence of aluminium-saturated diffu-

sion zone, under the conditions of high-temperature cyclic testing (increase of high temperature resistance and prevention of spinel formation during growth of Al₂O₃ layer) [9].

Developed recommendations on improvement of the technology of thermodiffusional aluminization of the surface of metal layer of CoCrAlY/8YSZ coatings (lowering of the temperature of vacuum heat treat-

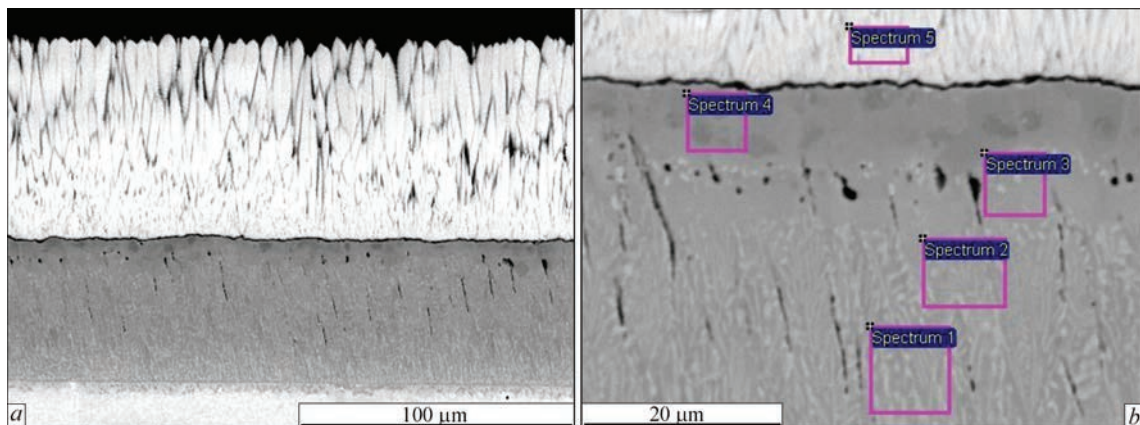


Figure 6. Microstructure (*a* — ×500; *b* — ×1800) and composition of CoCrAlY/8YSZ coating with predeposited PMS-Yu slurry after stages 1–4 (variant with low-temperature HT)

Table 5. Chemical composition (wt.%) of CoCrAlY/8YSZ layer with predeposited PMS-Yu slurry after stages 1–4 (variant with low-temperature HT)

Spectrum	O	Al	Si	Cr	Co	Y	Zr	Hf
1	–	11.3	–	22.8	65.9	–	–	–
2	–	11.6	–	22.9	65.5	–	–	–
3	–	14.9	0.4	21.3	63.4	–	–	–
4	–	21.7	0.8	13.4	64.0	–	–	–
5	25.1	–	–	–	0.6	7.6	64.6	2.2

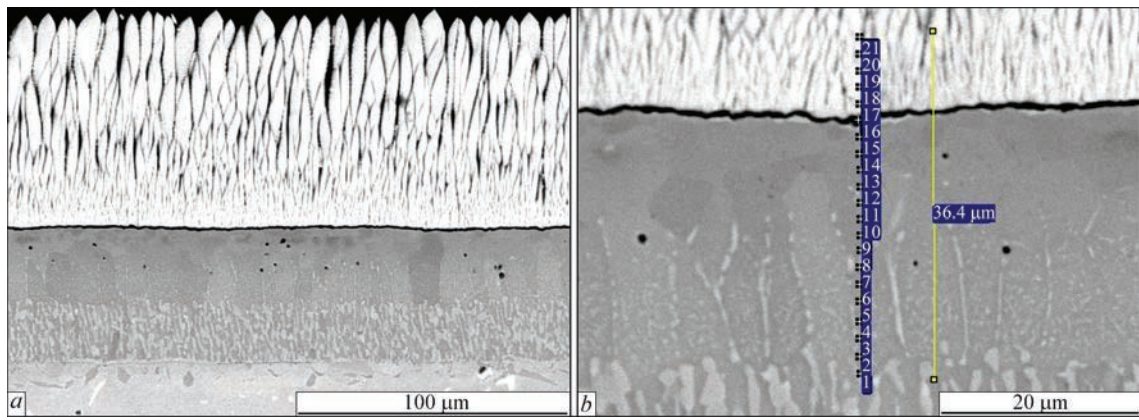


Figure 7. Microstructure (*a* — $\times 500$; *b* — $\times 1800$) of CoCrAlY/8YSZ coating and distribution of chemical elements in aluminium-saturated diffusion zone with predeposited PMS-Yu slurry after stages 1–4 (variant with low-temperature HT)

Table 6. Distribution of chemical elements (wt.%) in aluminium-saturated diffusion zone with predeposited PMS-Yu slurry after stages 1–4 (variant with low-temperature HT)

Spectrum	O	Al	Ti	Cr	Co	Ni	Y	Zr	Hf
1	–	12.7	0.8	23.9	54.4	8.3	–	–	–
2	–	14.0	0.7	18.4	56.4	10.4	–	–	–
3	–	14.9	0.8	19.4	56.2	8.8	–	–	–
4	–	10.5	0.5	21.8	60.0	7.3	–	–	–
5	–	14.9	→–	17.9	59.5	7.2	–	–	–
6	–	15.6	→–	18.0	59.8	6.1	–	–	–
7	–	13.0	→–	20.9	59.6	6.0	–	–	–
8	–	15.4	0.4	18.5	61.1	4.6	–	–	–
9	–	15.3	0.2	18.6	61.7	4.3	–	–	–
10	–	→–	0.1	18.2	62.4	4.0	–	–	–
11	–	14.8	0.3	20.6	61.4	2.9	–	–	–
12	–	→–	0.1	18.5	63.9	2.6	–	–	–
13	–	16.4	0.2	17.2	63.8	2.4	0.1	–	–
14	–	15.8	–	16.3	65.6	2.3	–	–	–
15	–	15.6	–	16.9	64.6	→–	–	0.7	–
16	31.8	19.3	–	5.4	9.6	0.2	2.9	29.7	1.2
17	24.6	1.2	–	0.5	0.8	–	6.9	63.4	2.6
18	→–	–	–	–	–	–	7.7	65.7	2.1
19	24.0	–	–	–	–	–	7.6	66.6	1.7
20	24.8	–	–	–	–	–	7.9	65.5	1.9
21	25.1	–	–	–	–	–	7.3	64.5	3.1

ment to 700–750 °C at stage 3 and optimized parameters for AAT at stage 4) were transferred to end user.

CONCLUSIONS

1. It was found that vacuum heat treatment of CoCrAlY layer with aluminium-containing slurry applied on its surface, ensures formation of a surface diffusion layer of heterogeneous thickness in it (10–40 μm) at the temperature in the range of 950–1100 °C, which contains two microstructure zones with different aluminium content. The outer zone contains globular particles of up to 20 μm size from intermetallics with the composition of 60 % Co–31 % Al–9 % Cr. Numerous microcracks are observed in this zone, its microhardness reaching 8 GPa. The inner zone contains 15–19 % aluminium.

2. It was established that diffusion of cobalt and chromium from CoCrAlY layer into the slurry layer (40 and 9 %, respectively) results in the slurry layer microhardness increasing up to the level of 9 GPa. Numerous microcracks form in it, which propagate into CoCrAlY layer.

3. Mode of low-temperature vacuum heat treatment (not higher than 700–750 °C) was determined, when a defectfree surface diffusion layer approximately 8 μm thick with aluminium content of approximately 42 % forms in CoCrAlY. Here, the slurry contains two zones: outer zone of approximately 30 μm thickness (slurry which did not react) and inner one of approximately 20 μm thickness (sintered slurry, containing approximately 34 % Co and 12 % Cr).

4. Performed thermal cyclic testing of blade airfoil segments with CoCrAlY/8YSZ coating, in which the thickness of diffusion zone saturated by aluminium from the diffusion zone slurry was equal to 15 µm, and aluminium content was up to 21 %, showed that slurry application increases the life by 25–30 % due to increase of high-temperature resistance of the metal layer and ability to prevent spinel formation during growth of Al₂O₃ layer.

5. Recommendations were developed as to improvement of the technology of thermodiffusion-aluminization of the surface of metal layer of CoCrAlY/8YSZ coatings to ensure the operation of blades made from high-temperature alloys of CM-88U and CM-93 type at higher temperature.

REFERENCES

1. Darolia, R. (2013) Thermal barrier coatings technology: Critical review, progress update, remaining challenges and prospects. *Int. Mater. Rev.*, **58**, 315–348. DOI: <https://doi.org/10.1179/1743280413Y.0000000019>
2. Pollock, T.M., Lipkin, D.V., Hemker, K.J. (2012) Multifunctional coating interlayers for thermal-barrier systems. *MRS Bulletin*, **37**, 923–931.
3. Movchan, B.A., Yakovchuk, K.Yu. (2004) Graded thermal barrier coatings, deposited by EB-PVD. *Surface & Coatings Technology*, **188–189**, 85–92.
4. Bababdani, S., Nogorani, F. (2014) Overaluminizing of a CoCrAlY coating by inward and outward diffusion treatments. *Metallurg. and Mater. Transact.*, **A45**, 2116–2112.
5. Jiang, J., Zhao, H., Zhou, X. et al. (2013) Oxidation resistance of vacuum plasma sprayed CoNiCrAlY coating modified by filtered cathodic vacuum arc deposition aluminizing. *J. of Thermal Spray Technology*, **22**, 69–74.
6. Pillai, R., Jalowicka, A., Galiullin, T. et al. (2019) Simulating the effect of aluminizing on a CoNiCrAlY-coated Ni-base superalloy. *Calphad*, **65**, 340–345. DOI: <https://doi.org/10.1016/j.calphad.2019.04.004>
7. Boissonnet, G., Grégoire, B., Bonnet, G., Pedraza, F. (2019) Development of thermal barrier coating systems from Al microparticles. Pt I: Influence of processing conditions on the mechanisms of formation. *Surface and Coatings Technology*, **380**, 125085. <https://doi.org/10.1016/j.surfcoat.2019.125085>
8. Kashin, D.S., Dergacheva, P.E., Stekhov, P.A. (2018) Heat-resistant coatings deposited by slip method (Review). *Trudy VIAM*, **65(5)**, 64–75 [in Russian].
9. Jalowicka, A., Naumenko, D., Ernsberger, M. et al. (2018) Alumina formation and microstructural changes of aluminized CoNiCrAlY coating during high temperature exposure in the temperature range 925–1075 °C. *Materials at High Temperatures*, **35(1–3)**, 66–77. DOI: <https://doi.org/10.1080/09603409.2017.1392114>

ORCID

K.Yu. Yakovchuk: 0000-0001-8446-1645,
A.V. Mykytchuk: 0000-0002-9761-9429,
Yu.E. Rudoy: 0000-0002-7265-1879,
R.O. Tkach: 0000-0002-6085-8901

CONFLICT OF INTEREST

The Authors declare no conflict of interest

CORRESPONDING AUTHOR

K.Yu. Yakovchuk
E.O. Paton Electric Welding Institute of the NASU
11 Kazymyr Malevych Str., 03150, Kyiv, Ukraine.
E-mail: yakovchuk@paton-icebt.kiev.ua

SUGGESTED CITATION

K.Yu. Yakovchuk, G.P. Myalnytsya,
A.V. Mykytchuk, Yu.E. Rudoy, R.O. Tkach (2022)
Development of the CoCrAlY/ZrO₂-8 % Y₂O₃ type
thermal barrier coating by surface doping of the
metal layer with aluminium. *The Paton Welding J.*,
8, 39–45.

JOURNAL HOME PAGE

<https://pwj.com.ua/en>

Received: 04.07.2022

Accepted: 17.10.2022

XVI International Conference

"Problems of corrosion and corrosion protection of materials"

"Corrosion-2022"

15–16 November, Lviv, Ukraine



The Organizing Committee continues the registration of participants and forms a conference abstracts book. Papers containing new, original results will be selected for publication in the journal «Materials Science» (Scopus).

<https://www.ipm.lviv.ua/corrosion2022>

DOI: <https://doi.org/10.37434/tpwj2022.08.07>

EVALUATION OF BRITTLE FRACTURE RESISTANCE OF WWER-1000 REACTOR BAFFLE DURING LONG-TERM SERVICE, TAKING INTO ACCOUNT THE RESIDUAL TECHNOLOGICAL STRESSES

O.V. Makhnenko, S.M. KandalaE.O. Paton Electric Welding Institute of the NASU
11 Kazymyr Malevych Str., 03150, Kyiv, Ukraine**ABSTRACT**

The need to take into account the residual technological stresses (RTS) in the material of the baffle of reactor internals (RI) of NPP power units of WWER-1000 type, resulting from technological processes of welding and postweld heat treatment at extension of safe service period beyond the design life is substantiated. The influence of RTS on the stress-strain state of the baffle, as well as brittle fracture resistance (BFR) of the material in service was determined. It is shown that an essential redistribution of axial and circumferential stresses in the baffle is observed due to allowing for RTS, namely of the zone of high tensile stresses, which under normal operation conditions (NOC) move into the internal volume of the baffle from its outer surface, while the area of these zone becomes larger. Such a redistribution of stresses has an essential influence on the level of stress intensity coefficient on the contour of the cracklike defects. The most critical areas, in terms of brittle strength, form in the inner volume of the baffle, whereas the dimensions of subsurface elliptical crack, which is postulated, can be increased due to widening of the tensile stress zone, thus promoting greater conservatism of BFR assessment. Moreover, taking RTS into account allows a significant lowering of conservatism at assessment of baffle BFR under NOC for surface semielliptic cracks, located on the baffle outer surface, where residual compressive stresses arise during manufacture. Obtained results allow more precise determination of baffle zones, prone to brittle fracture of the material under NOC that is important for improvement of the approaches to determination of RI of WWER-1000 type reactor.

KEYWORDS: WWER-1000, reactor internals, baffle, residual technological stresses, brittle fracture resistance, postulated cracks, stress intensity coefficient, normal operating conditions

INTRODUCTION

WWER-1000 reactor internals (RI) are very important structural elements which influence the life of all power plant. One of the key approaches in the papers on extension of life of NPP safe operation is a predictive evaluation of the structural integrity of structures with the help of mathematical modeling of the physical processes typical for conditions of operation of power units in radiation exposure of structural material. The results of existing investigations [1, 2] justify the insurance of conditions of brittle fracture resistance of RI baffle under normal operating conditions (NOC) and emergencies. However, these papers do not consider the effect of residual technological stresses on structural integrity of RI elements in course of long-term operation.

Mathematical modeling methods allowed determining appearance of high residual technological stresses (RTS) in manufacture of RI of WWER-1000 power unit. It happens in a process of fast air cooling during postweld heat treatment by austenitization mode ($T = 1100\text{ }^{\circ}\text{C}$). A calculation analysis of a level of effect of determined RTS on stress-strain state and brittle fracture resistance (BFR) of the RI baffle in a process of long-term operation up to 60 years with

different level of accumulated damaging dose was carried out in this paper.

Inner surface of a thick-walled cylinder shell of the baffle has faceted shape which limits a reactor core (Figure 1, *a*). The structure has a mirror-cyclic symmetry that allows dividing it on the twelve similar 30-deg sectors in modeling (Figure 1, *b*). A baffle section is inhomogeneous and being characterized with the presence of 84 cooling channels and its thickness varies in the limits from 67 to 242 mm. Material is austenitic steel 08Kh18N10T.

INPUT DATA

In order to determine the level of effect of RTS on SSS and BFR of the baffle structure in the process of long-term operation the following input data were used (Figure 2), namely RTS distribution [3]; two distributions of accumulated damaging dose different by level; distribution of heat emission due to γ -heating. Used distributions of the damaging dose and heat emission are taken as typical data from a practice of performance of corresponding calculations.

MODELS OF RADIATION SWELLING AND CREEP

A process of long-term operation of RI baffle under conditions of neutron radiation is accompanied by ra-

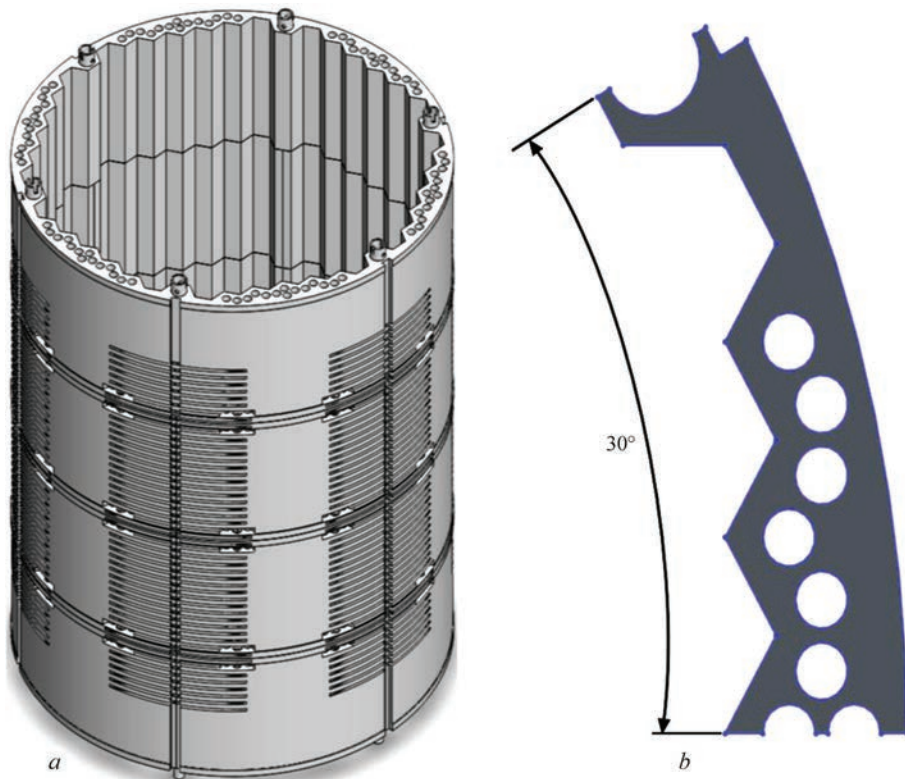


Figure 1. Appearance of baffle (a) and its cross-section (30-deg sector) (b)

diation swelling which can be described by a model tested in SE NNEGEC “Energoatom” [4–6]:

$$S = C_D \cdot D^n \cdot f_1(T) \cdot f_2(\sigma_m, \sigma_{eq}) \cdot f_3(\alpha), \quad S > 0,$$

$$f_1(T) = \exp(-r \cdot (T - T_{\max})^2),$$

$$f_2(\sigma_m, \sigma_{eq}) = 1 + P \cdot (0.85 \cdot \sigma_m + 0.15 \cdot \sigma_{eq}),$$

$$f_3(\alpha) = \exp(-\eta \cdot \alpha),$$

$$C_D = 1.035 \cdot 10^{-4} \text{ dpa}^{-n}, \quad n = 1.88,$$

$$r = 1.825 \cdot 10^{-4}, \quad ^\circ\text{C}^{-2}, \quad T_{\max} = 470 \text{ }^\circ\text{C},$$

$$P = 8 \cdot 10^{-3} \text{ MPa}^{-1}, \quad \eta = 8.75, \quad (1)$$

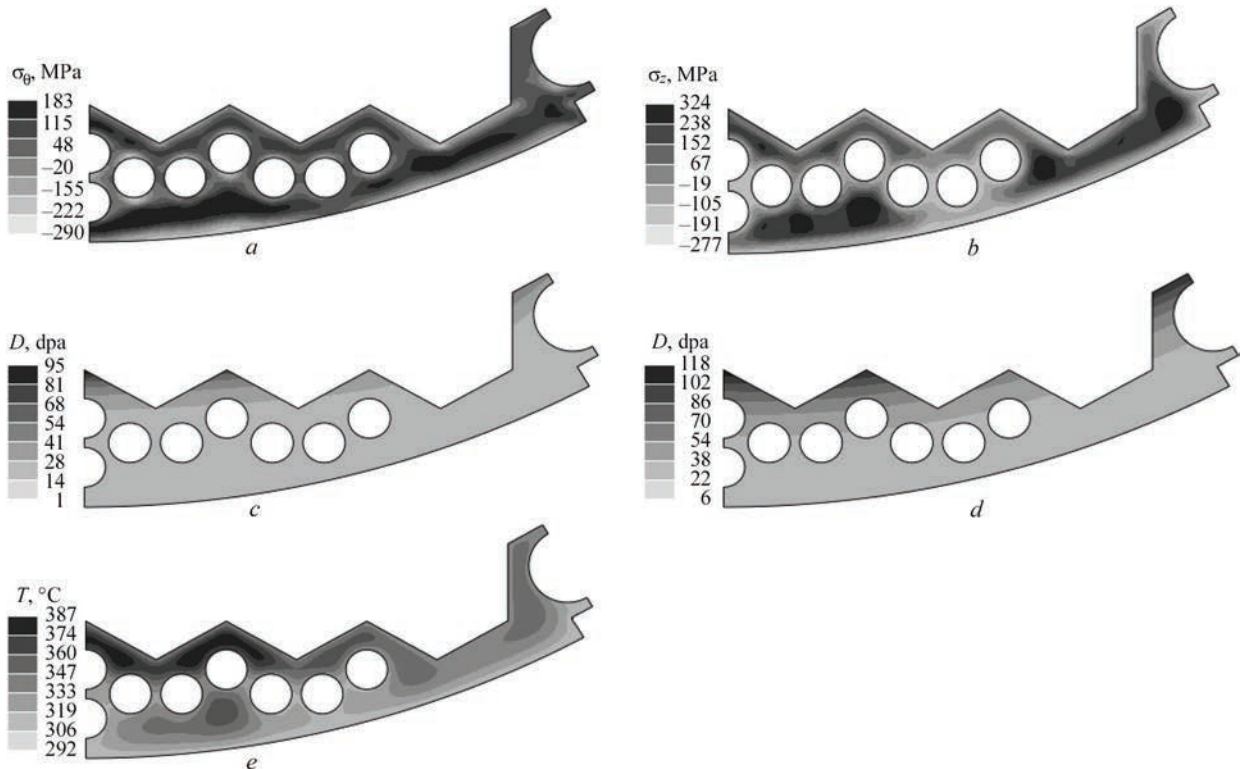


Figure 2. Input data for calculation: distributions of circumferential (a) and axial (b) RTS; distributions of accumulated damaging dose — variant 1 up to 95 dpa (c) and variant 2 up to 118 dpa (d); temperature field as a result of γ -heating (heat emission) (e)

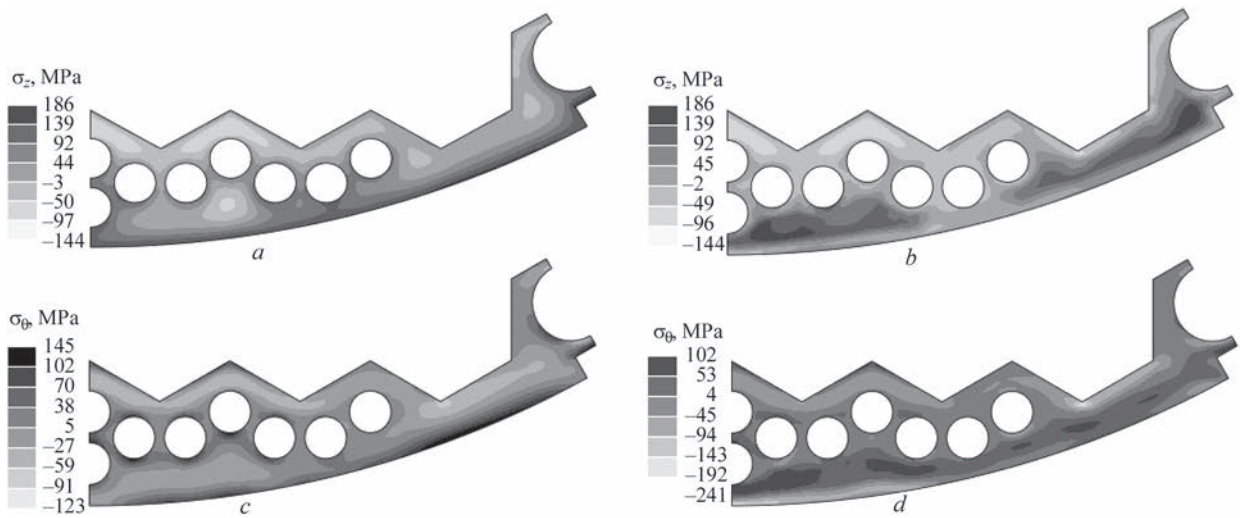


Figure 3. Distributions of stresses in the baffle in its sixtieth year of operation with maximum accumulated dose 95 dpa: *a* — axial component without consideration of RTS; *b* — axial component with RTS consideration; *c* — circumferential component without RTS consideration; *d* — circumferential component with RTS consideration

where S is the swelling, %; D is the damaging dose, dpa; T is the radiation temperature, °C; σ_m are the medium stresses, MPa; σ_{eq} are the equivalent stresses, MPa; α is the Odqvist parameter.

Also the model takes into account deformations of radiation creep which for 08Kh18N10T steel is described by the law [6]:

$$\frac{d\varepsilon^{cr}}{dt} = \left(B_0 \frac{dD}{dt} + \omega \frac{dS}{dt} \right) \sigma_{eq}, \quad (2)$$

where ε^{cr} is the radiation creep deformation; $B_0 = 1 \cdot 10^{-6} \text{ (MPa} \cdot \text{dpa)}^{-1}$, $\omega = 2.95 \cdot 10^{-3} \text{ (MPa}^{-1})$.

DETERMINATION OF STRESS DISTRIBUTIONS DURING OPERATION

SSS of the baffle taking into account the processes of radiation swelling and creep of material can be

determined as a result of solution of a boundary value problem of mechanics of continuous media using finite element method in the elastic-viscous-plastic statement [5, 7]:

$$\varepsilon = \varepsilon^e + \varepsilon^p + \varepsilon^{cr},$$

where ε are the total deformations; ε^e , ε^p , ε^{cr} are elastic, plastic and creep deformations, respectively.

Solution of the corresponding 2D problem with initial and boundary conditions in form of RTS distributions, damaging dose and heat emission due to γ -heating (Figure 2) as well as conditions of heat exchange with coolant of the baffle surfaces [5, 7] by means of continuous monitoring of time with $\Delta t = 0.2$ year step resulted in getting the distributions of stresses in a baffle cross-section in the processes of long-term operation taking and not taking into account RTS. Figures 3, 4 show axial and circumfer-

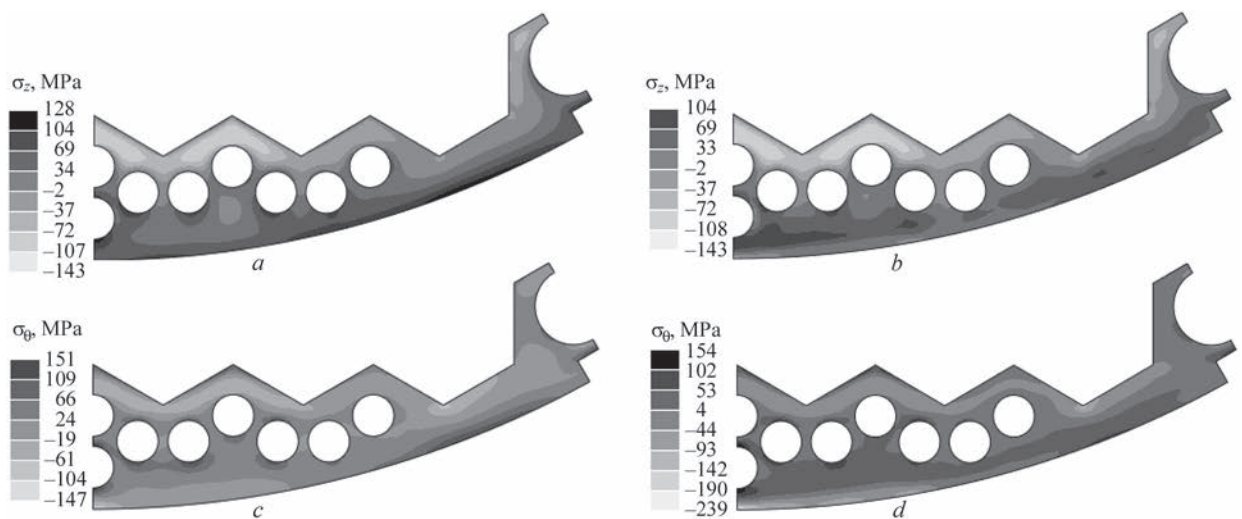


Figure 4. Distributions of stresses in the baffle in its sixtieth year of operation with maximum accumulated dose 118 dpa: *a* — axial component without consideration of RTS; *b* — axial component with RTS consideration; *c* — circumferential component without RTS consideration; *d* — circumferential component with RTS consideration

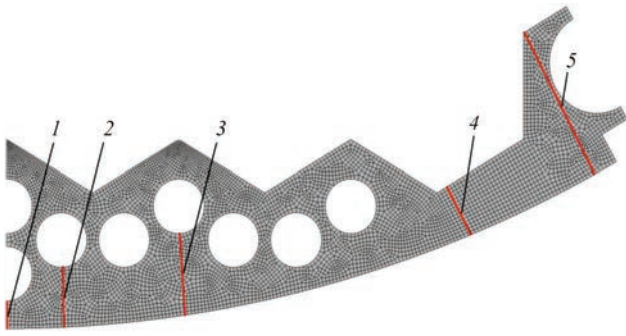


Figure 5. Scheme of location of typical sections for evaluation of RTS effect on SSS of the baffle in process of long-term operation. The diagram shows a cross-section of a baffle with five numbered sections (1-5) marked for stress analysis. Section 1 is at the outer edge, section 2 is near the cooling channels, section 3 is in the middle, section 4 is near the inner edge, and section 5 is at the very inner edge.

ential stresses in operating mode of the baffle in its sixtieth year of operation for two considered variants of the level of accumulated damaging dose — 95 dpa and 118 dpa, respectively.

Figures 3, 4 demonstrate noticeable difference of stress distributions in axial and circumferential directions depending on RTS consideration. Taking into account RTS the zones of high tensile stresses from outer wall of the baffle transfer into external volume and their area increases. Also it is necessary to note the effect of the level of damaging accumulated dose on the level of stresses in process of baffle operation.

As can be seen from data on Figures 3, 4 RTS have small effect on distribution of stresses on inner surface of the baffle in area of cooling channels. Therefore, for the analysis there were taken 5 typical sections closer to outer surface, where effect of RTS on SSS of the baffle is the most significant. Figure 5 shows a scheme of their location.

Figures 6, 7 represent the calculation distributions of axial and circumferential stresses in sections No. 1 and No. 5, respectively, in the sixtieth year of operation depending on accumulated damaging dose and considering RTS.

Consideration of RTS can promote decrease of the level of stresses in axial direction in the process of operation (Figure 6, *a*) and closer to the baffle outer

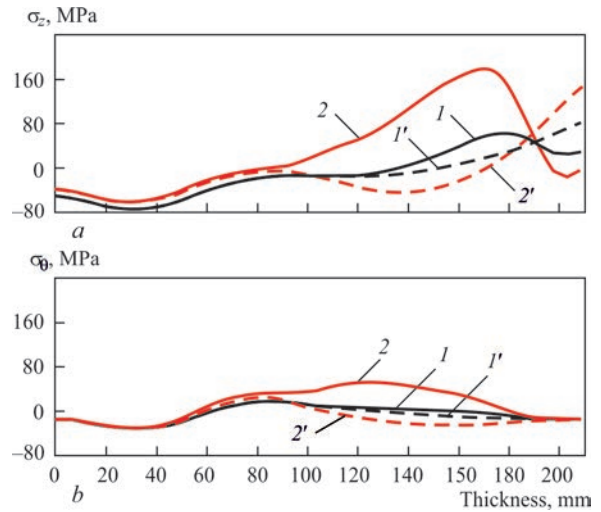
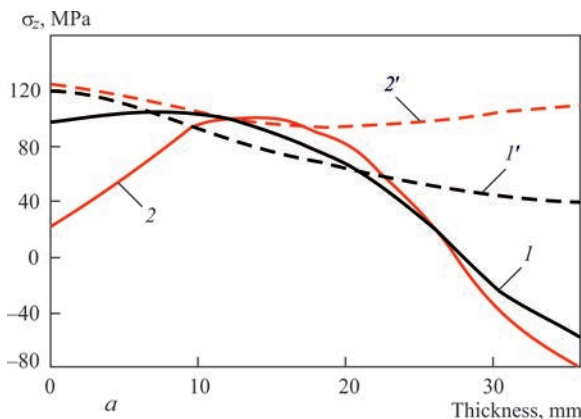


Figure 7. Distribution of axial $\sigma_z(a)$ and circumferential σ_θ stresses in section No. 5 depending on accumulated damaging dose and RTS consideration: 1' — at $D_{\max} = 118$ dpa; 2' — at $D_{\max} = 95$ dpa without RTS consideration; 1 — at $D_{\max} = 118$ dpa; 2 — at $D_{\max} = 95$ dpa with RTS consideration

surface in section No.1 the stresses even transfer into compressive ones.

Data from Figure 7, which refer to section No. 5, show that consideration of RTS independent on level of accumulated damaging dose has significant effect on stress distribution, namely takes place formation of the zones of high tensile stresses (up to 180 MPa) in axial direction (Figure 7, *a*).

It should be noted that the circumferential stresses (Figure 6, *b* and Figure 7, *b*) in comparison with axial ones are relatively low in examined sections (up to 50 MPa) and in most of the cases consideration of RTS does not promote significant effect on their distribution.

Also, it was determined that in sections Nos 2–4 the axial stresses in case of taking into account RTS are greatly higher in the baffle inner volume, whereas on the inner and outer surfaces they become lower in comparisons with the calculation case, where RTS have not been considered.

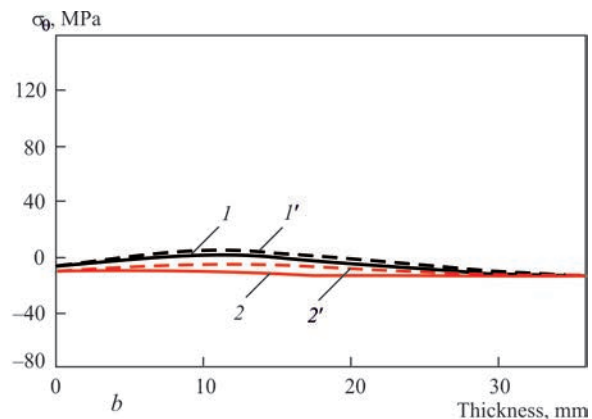


Figure 6. Distribution of axial $\sigma_z(a)$ and circumferential σ_θ stresses in section No. 1 depending on accumulated damaging dose and RTS consideration: 1' — at $D_{\max} = 118$ dpa; 2' — at $D_{\max} = 95$ dpa without RTS consideration; 1 — at $D_{\max} = 118$ dpa; 2 — at $D_{\max} = 95$ dpa with RTS consideration

BFR CALCULATION PROCEDURE

In accordance with the existing requirements [4] BFR calculation is one of the necessary strength calculations during calculation substantiation of RI safe operation. It is performed corresponding to the requirements of acting in Ukraine reference documents [8] as well as it is necessary to take into account the recommendations of foreign documents [6, 9].

Brittle fracture resistance of RI is provided if the following condition is fulfilled under all operation conditions:

$$K_1 \leq [K_1]_i, \quad (3)$$

where K_1 is the calculation value of stress intensity coefficient (SIC) on a contour of postulated crack; $[K_1]_i$ is the allowable SIC value, which is determined for normal operation conditions (NOC) ($i = 1$) with a safety factor $n_k = K_{1c}/[K_1]_1 = 2$, K_{1c} is the critical value of material SIC.

Elliptical subsurface crack with large semi-axis c and smaller semi-axis a (Figure 8, *a*) as well as semi-elliptical surface crack (Figure 8, *b*) are considered as a postulated crack. According to PNAE [8] the relationship of semi-axes $a/c = 2/3$ and according to [4] $a/c = 1/3$, the maximum postulated defect depth $2a$ can not exceed quarter of base metal thickness.

It should be noted that the RI elements operate under conditions of intensive neutron irradiation.

This in process of operation results in degradation of mechanical properties of the base metal. Therefore, the critical values of SIC in the different points (volumes) of the base metal will depend on the level of accumulated damaging dose as well as radiation temperature and can be described by the next law [4]:

$$J_c(D, T, T_{irr}) = 2.5 \cdot 10^{-4} \sigma_y(D, T, T_{irr}) \times \left[1 - A_{J(e)} \sqrt{1 - \exp(-0.2D)} \right], \quad (4)$$

where σ_y is the material yield strength, MPa; D is the accumulated damaging dose, dpa; $A_{J(e)} = 0.93$.

In order to determine the SIC critical values using J -integral values there was used a transition formula [1]:

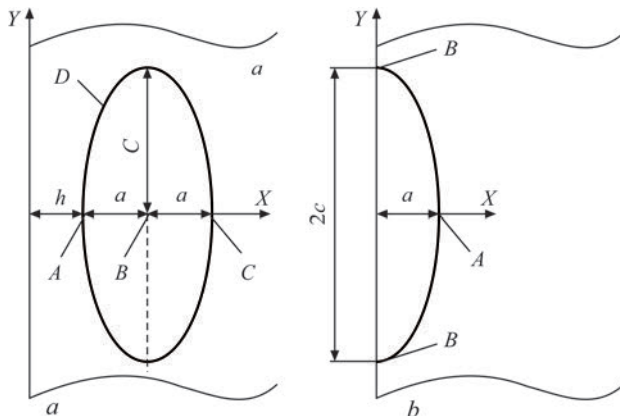


Figure 8. Postulated elliptical (a) and semi-elliptical (b) cracks

$$J = \frac{K_I^2(1 - \nu^2)}{E}. \quad (5)$$

Calculation of SIC values for the postulated cracks was carried out by three different procedures according to PNAE [8], VERLIFE [6] and RD EO [9].

METHOD ACCORDING TO PNAE

According to the requirements of PNAE [8] the SIC for cylinder elements being loaded by internal pressure and temperature effect is allowed to be determined by formula:

$$K_I = \eta (\sigma_p M_p + \sigma_q M_q) \sqrt{\left(\pi \frac{a}{10^3} \right)} / Q, \quad (6)$$

where η is the coefficient that considers the effect of stress concentration; σ_p is the component of tensile stresses, MPa; σ_q is the component of bending stresses, MPa; $M_p = 1 + 0.12(1 - a/c)$, $M_q = 1 - 0.64a/h$; a — crack depth, mm; c is the semi-length of crack, mm; h is the length of zone, in the limit of which a component of bending stresses saves the positive value, mm,

$$Q = \left[1 + 4.6(a/2c)^{1.65} \right]^{1/2}. \quad (7)$$

A component of tensile stresses (circumferential or axial) are determined by formula:

$$\sigma_{jp} = \frac{1}{s} \int \sigma_j dx, \quad (8)$$

where j is the θ or Z coordinate; σ_j is the function of change of stresses on wall thickness; s is the wall thickness in calculation section.

A value of component of bending stresses are determined by formula:

$$\sigma_{jq} = \sigma_{jn} - \sigma_{jp}, \quad (9)$$

where σ_{jn} are the values of function of stress change by wall thickness in point n .

It should be noted that PNAE [8] has no information for which type of the crack-like defects (subsurface, elliptical or surface semi-elliptical) the SIC determination procedure is used.

METHOD ACCORDING TO VERLIFE

Following the VERLIFE recommendations [6] a coefficient of stress intensity K_I is determined from the relationship:

$$K_I = \sigma_K Y \sqrt{a}, \quad (10)$$

where σ_K are the stresses brought to uniform, MPa; Y is the coefficient of crack shape; a is the small semi-axis of crack.

The coefficient of crack shape Y is determined depending on crack type and location of point Q on its con-

tour. For a subsurface elliptical crack the following expressions are typical:

$$Y_A = \frac{1.79 - 0.66 \cdot a/c}{[1 - \beta^{1.8}(1 - 0.4(a/c) - \gamma^2)]^{0.54}},$$

$$Y_C = \frac{1.79 - 0.66 \cdot a/c}{[1 - \beta^{1.8}(1 - 0.4(a/c) - 0.8\gamma^{0.4})]^{0.54}}, \quad (11)$$

where $\beta = \frac{a}{b+a}$; $\gamma = 0.5 - \frac{b+a}{s}$ s is the base metal thickness, mm.

For surface semi-elliptical crack the shape coefficients are determined in accordance to the following expressions:

$$Y_A = \frac{2 - 0.82 \cdot a/c}{\left\{1 - \left[0.89 - 0.57(a/c)^{1/2}\right]^3 (a/s)^{1.5}\right\}^{3.25}},$$

$$Y_B = \left[1.1 + 0.35 (a/s)^2\right] (a/c)^{1/2} \cdot Y_A. \quad (12)$$

For subsurface elliptical crack the stresses, being brought to uniform, were determined from the following relationships, which describe their distribution by parabolic law:

$$\sigma_{KB} = \frac{\sigma_B + \sigma_C}{2} + \frac{a}{c} \cdot \frac{4\sigma_B - 3\sigma_C - \sigma_A}{30},$$

$$\sigma_{KB} = \frac{\sigma_B + \sigma_C}{2} + \frac{a}{c} \cdot \frac{4\sigma_B - 3\sigma_C - \sigma_A}{30}. \quad (13)$$

When postulating a surface semi-elliptical crack in section 4 the stresses on wall thickness are distributed by linear dependence:

$$\sigma_{KB} = 0.18 \sigma_A + 0.82 \sigma_B. \quad (14)$$

It is necessary to note that the VERLIFE procedure of determination of the stress intensity coefficients for a subsurface elliptical crack includes no methods to set a complex law of distribution of stresses and as a result of description of a random distribution of stresses by parabolic law the K_I values can be determined with the significant errors.

METHOD ACCORDING TO RD EO

The method for SIC determination according to RD EO 1.1.2.05.0330–2012 [9] is similar to procedure VERLIFE [6], however, proposes the expressions for SIC calculation at more complex law of stress distribution. Such crack shape coefficients are determined by the following dependencies:

$$Y = \left[1 - \left(\frac{a}{h+a}\right)^{1.8} \left(1 - 0.4 \frac{a}{c} - \gamma\right)\right]^{-0.54} \times$$

$$\times \left[\frac{\pi}{1 + 1.464(a/c)^{1.65}}\right]^{0.5}, \quad (15)$$

at $a \leq c$; $a \leq 9h$; $h + a \leq s/2$:

$$\gamma_A = \left(0.5 - \frac{h+a}{s}\right)^2 \quad \gamma_C = 0.8 \left(0.5 - \frac{h+a}{s}\right)^{0.4}. \quad (16)$$

$x_j = h + a/10$, where $j = 0, 1, 2, \dots, 20$ coordinate is calculated for the stress distribution set in the arbitrary form (in form of approximation function). Stresses $\sigma_j = \sigma_K(x_j)$ are determined in each x_j point. The values of $\sigma_K(A)$ and $\sigma_K(C)$ brought to uniform are calculated by formulas:

$$\sigma_{eq}(A) = \sum_{j=0}^{20} \left(A_j + \frac{a}{c} B_j\right) \sigma_j,$$

$$\sigma_{eq}(C) = \sum_{j=0}^{20} \left(A_{20-j} + \frac{a}{c} B_{20-j}\right) \sigma_j, \quad (17)$$

where A_j and B_j are the table values.

Among the three methods for SIC determination considered above the latter one, described in RD EO 1.1.2.05.0330–2019 [9], is the most accurate. It takes into account the depth of crack occurrence and the stresses can be described by an arbitrary shape law (in form of approximation function). The procedure, described in VERLIFE [6], is good to use for express-evaluations to brittle fracture resistance as well as for the cracks which are postulated in the zones with linear and parabolic stress distribution.

RESULTS OF CALCULATED EVALUATION OF BFR

As it was mentioned above, there were considered two variants of accumulated damaging dose. Therefore, mechanical properties of baffle material and corresponding SIC critical values will be different for each of the variants. Figure 9 shows the distributions between material yield limit of the baffle in its sixtieth year of operation as well as SIC critical values for different input data.

As can be seen from Figure 9, the level of material yield limit is changed depending on the accumulated damaging dose. Thus, the yield limit is in 438–873 MPa range at the maximum value of accumulated damaging dose 95 dpa and at 118 dpa it becomes 673–838 MPa (Figure 9, *a, b*) that, respectively, effect the SIC critical value (Figure 9, *c, d*).

It was determined as a result of mathematical modeling of the processes of welding, heat treatment and further operation of RI elements in course of 60 years that the maximum tensile stresses are formed in the axial direction. Therefore, from point of view of conservatism

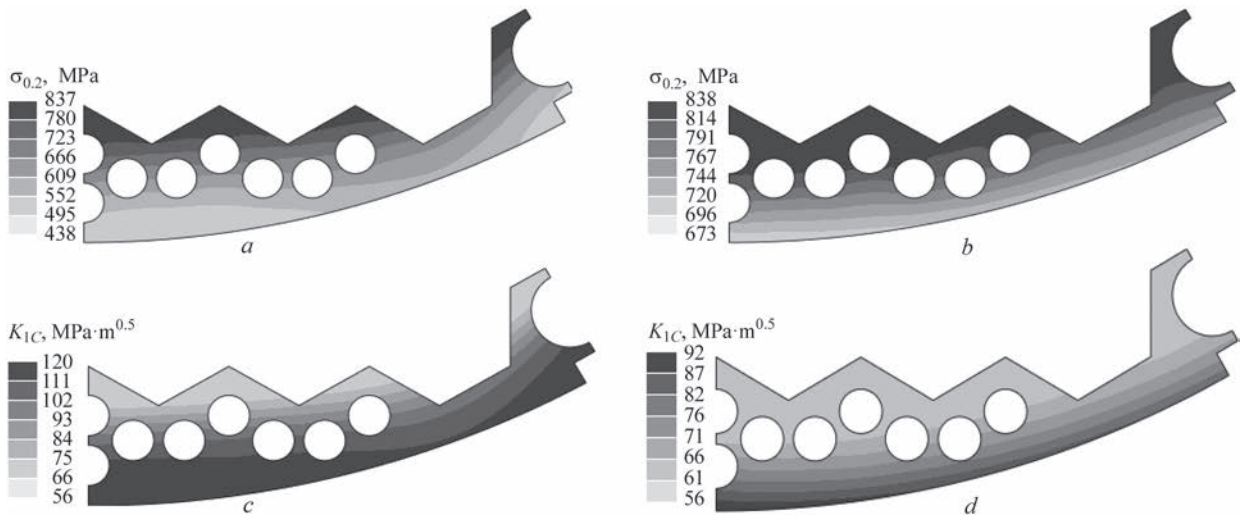


Figure 9. Distributions of yield limit $\sigma_{0.2}$ of baffle material at accumulation of damaging dose of 95 dpa (a) and 118 dpa (b) and critical value K_{Ic} at 95 dpa (c) and 118 dpa (d)

the subsurface elliptical cracks located in circumferential direction were considered in SIC determination. A scheme of location of the baffle sections, in which the defects were postulated, is shown in Figure 5.

Table 1 presents the results of comparison of SIC values without RTS consideration and Table 2 with RTS consideration for section No. 5 (Figure 5), which is located in a zone of the biggest effect of RTS on SSS of baffle structure. They were obtained according to three procedures described above [8, 9] after 30 and 60 years

of operation for two variants of a level of accumulated damaging dose and cracks with various a/c .

The most conservative are the SIC values obtained using RD EO procedure [9] which is reasonable for application for BFR analysis with arbitrary distribution of stresses in the crack location zone. The methods, described in PNAE [8] and VERLIFE [6], should be used for evaluation of SIC in the less loaded areas with linear or parabolic law of stress distribution. The maximum SIC values in most of the cases are located in point A of

Table 1. SIC for cracks with different a/c in section No.5 without RTS consideration

a/c	Max. accum. dose, dpa	$K_A, \text{MPa}\cdot\text{m}^{0.5}$		$K_C, \text{MPa}\cdot\text{m}^{0.5}$		$K_D, \text{MPa}\cdot\text{m}^{0.5}$		$K, \text{MPa}\cdot\text{m}^{0.5}$
		RD EO	VERLIFE	RD EO	VERLIFE	RD EO	VERLIFE	PNAE
30 years of operation								
1/3	47.5	25	24.7	6.5	7.7	16.5	16.2	25.7
	59	15.3	15.1	4.4	5.5	10.5	10.3	14.9
2/3	47.5	20.6	20.8	4.6	5.9	14.9	13.3	21.7
	59	19.8	19.6	4.6	6.1	15.4	12.9	16.0
60 years of operation								
1/3	95	24.1	23.8	6.6	8.0	16.1	15.5	24.5
	118	15.5	15.3	5.6	7.4	11.3	11.4	13.8
2/3	95	19.8	20.0	4.7	6.1	14.5	12.4	20.7
	118	19.9	19.7	5.9	8.5	16.5	14.1	14.7

Table 2. SIC for cracks with different a/c in section No.5 with RTS consideration

a/c	Max. accum. dose, dpa	$K_A, \text{MPa}\cdot\text{m}^{0.5}$		$K_C, \text{MPa}\cdot\text{m}^{0.5}$		$K_D, \text{MPa}\cdot\text{m}^{0.5}$		$K, \text{MPa}\cdot\text{m}^{0.5}$
		RD EO	VERLIFE	RD EO	VERLIFE	RD EO	VERLIFE	PNAE
30 years of operation								
1/3	47.5	39.5	38.8	25.1	34.7	30.9	36.7	37.2
	59	19.8	19.3	10.2	15.8	14.2	17.6	16.0
2/3	47.5	44.7	44.0	22.0	28.7	39.3	36.3	40.7
	59	16.7	16.4	7.8	13.2	13.7	14.8	11.7
60 years of operation								
1/3	95	34.6	33.9	21.3	29.7	26.7	31.6	32.4
	118	11.5	11.1	5.0	8.2	7.9	9.6	11.0
2/3	95	39.3	31.5	17.6	25.6	33.4	29.1	35.4
	118	14.7	14.1	5.5	9.8	11.7	11.9	11.7

a contour of postulated crack (Figure 8) and their values are correlated with the results of each procedure.

RTS consideration in one section can have positive as well as negative effect according to the results of SIC determination in section No. 5. For example, consideration of RTS rises conservativeness of SIC calculation in the 30th year of operation by 2.2 times (from 20.6 to 44.7 MPa·m^{0.5}).

Baffle sections Nos 1–4 were also examined (Figure 5). SIC calculation was performed in accordance with RD EO [9]. A comparative analysis in the sections was carried out for postulated defects in form of subsurface elliptical cracks depending on operation period, accumulated damaging dose and RTS consideration. Geometry dimensions of the cracks (semi-axes a and c) were chosen depending on dimensions of the zones of tensile stresses and can be changed for one and the same section depending on the level of accumulated damaging dose and RTS consideration. A depth of defect location h was determined depending on its allowable limits.

In section No.1 there were obtained lower values of SIC in RTS consideration than in the model without RTS consideration. For comparison it was considered a calculation variant in the 30th year of operation for higher level of accumulated damaging dose, where relationship between small and large semi-axes of the postulated crack is taken equal $a/c = 1/3$ and their dimensions due to large zone of tensile stresses correspond to the maximum allowable according to PNAE [8] values $a = 9$ mm; $c = 27$ mm at base metal thickness $S = 36$ mm, crack occurrence depth $h = 3$ mm. It was determined based on all indicated above input parameters that the maximum value without RTS consideration made $K_I = 17.2$ MPa·m^{0.5} and with RTS consideration $K_I = 12.6$ MPa·m^{0.5}, thus in this case RTS consideration allows reducing conservativeness of BFR evaluation by 27 %. However, the largest decrease of SIC (by 58 %) at RTS consideration was determined in section No.4 with $K_I = 41.4$ MPa·m^{0.5} up to 17.5 MPa·m^{0.5}.

Following the calculation results the SIC increase can also be observed with increase of size of the postulated defect. Calculation case of section No. 2 in the 60th year of operation with the maximum accumulated dose 118 dpa and RTS consideration with different relationships $a/c = 1/3$ [4] and $a/c = 2/3$ [8] was considered for comparison. Their dimensions due to large tensile stress area according to PNAE [8] correspond to the maximum allowable values $a = 19.5$ mm; $c = 58.5$ mm (at $a/c = 1/3$) and $c = 29.25$ mm (at $a/c = 2/3$) at base metal thickness in section $S = 78$, depth of crack occurrence $h = 2$ mm. On the grounds of all input parameters it was determined that in calculation case, where $a/c = 1/3$ $K_I = 21.4$ MPa·m^{0.5} and at $a/c = 2/3$ $K_I = 17.5$ MPa·m^{0.5}, that is consideration of the existing requirements [4] in this

case allows increase conservativeness of SIC evaluation in section No. 2 by 18 % in comparison with PNAE requirements [8]. However, in case when geometry of the baffle section is limited by the size of large semi-axis, increase of area of the postulated defect takes place due to increase of the small semi-axis a . It was determined by the example of section No. 5 that the most conservative SIC evaluation is carried out by the requirements of relationships of semi-axes $a/c = 2/3$ according to PNAE [8].

The results of calculation showed that the level of SIC value is affected by postulated crack size, selection of which is determined by dimensions of tensile stress zone, which in turn can depend on RTS consideration. Also higher level of radiation (accumulated dose) of the baffle material reduces effect of RTS on stressed state and, respectively, BFR evaluation of structure.

In addition to the subsurface elliptical crack there was also considered a surface semi-elliptical crack. Since in RTS consideration the maximum level of stresses is observed not on the baffle surface, as in the case without RTS consideration, but in its volume, then the SIC values for the surface defect will be lower. Therefore, the crack in only one section with the largest value of axial stresses in the indicated area was examined. Following the data in Figure 3, the highest stresses in axial direction without RTS consideration are in a zone of section No. 4 (Figure 5), and, respectively to the obtained data the highest SIC values are determined in the 30th year of operation for a variant of lower level of damaging dose accumulation. The procedure in accordance with VERLIFE document was used for determination of the maximum SIC for the case without RTS consideration ($K_I = 26.6$ MPa·m^{0.5}) and with RTS consideration the value reduces ($K_I = 7.1$ MPa·m^{0.5}). Thus, RTS consideration allows significantly reducing conservativeness in determination of SIC for the defect on baffle outer surface.

NOC in addition to steady operation mode includes the modes of heating and cooling during an operation mode setting and reactor stops as well as hydraulic testing. Taking into account low rate of heating and cooling under NOC these processes do not have negative effect on BFR of the baffle. The level of stresses in the baffle significantly decreases in a cold status due to absence of a temperature gradient in relation to a heated status in the operation mode. Increase of pressure of coolant on all baffle surfaces during hydraulic testing promotes additional uniform compression (by 8 MPa), and, respectively, decrease of tensile stresses in the baffle volume in comparison with the conditions of loading in the operation mode, that also promotes fulfillment of BFR condition.

Therefore, the calculation results allowed determining significant effect of RTS on evaluation of BFR of WWER-1000 reactor baffle under NOC. Under emergency conditions the level of J -integral for

surface semi-elliptical cracks can reach values close to the critical ones [1]. However, the work does not consider RTS that can significantly affect the results of BFR evaluation. Thus, the next relevant problem is calculation evaluation of BFR of WWER-1000 reactor baffle under conditions of emergency with consideration of determined RTS [1].

CONCLUSIONS

1. Consideration of RTS significantly affect the distribution of stresses in WWER-1000 reactor baffle in operation mode under NOC, namely, there is formation of zones of high axial tensile stresses (up to 180 MPa). At that, the axial stresses are significantly higher in the baffle inner volume, whereas in the inner and outer surfaces they become lower in comparison with a calculation case, where RTS were not considered. Circumferential stresses are relatively low (up to 50 MPa) and consideration of RTS does not promote significant effect on their distribution.

2. Subsurface elliptical cracks located in a circumferential direction under effect of high axial tensile stresses were considered in performance of calculation BFR evaluation of the baffle under NOC as a postulated defect from point of view of maximum conservatism. The results of calculations in various sections of the baffle showed that conservativeness of BFR evaluation at RTS consideration can rise, but K_{Ic} SIC values for the postulated cracks do not exceed K_{Ic} critical value taking into account safety factor $n_k = 2$, i.e. BFR condition is fulfilled and in course of long-term operation the values of BFR safety factor $\eta = K_{Ic} / [K_{Ic}]_1$ increases at the expense of stress relaxation in a process of radiation creep.

3. The most dangerous from point of view of BFR under NOC is the section No. 5 of the baffle (in zone of large cooling channel), where the SIC maximum values for circumferential elliptical crack reach in the 30th year of operation $K_{Ic} = 45 \text{ MPa}\cdot\text{m}^{0.5}$ and in the 60th year it is $K_{Ic} = 39 \text{ MPa}\cdot\text{m}^{0.5}$ at allowable SIC values $[K_{Ic}]_1 = 58 \text{ MPa}\cdot\text{m}^{0.5}$ and $[K_{Ic}]_1 = 53 \text{ MPa}$, respectively. In other words, the minimum value of BFR safety factor during operation rises to $\eta = 1.36$.

4. The higher level of accumulated damaging zone of the baffle material in process of operation promotes decrease of a level of the maximum stresses in the baffle due to effect of radiation creep. Effect of RTS on stressed state decreases, respectively, and BFR evaluation of the structure becomes less conservative.

5. Consideration of RTS allows dramatically decrease the conservativeness in evaluation of baffle BFR under NOC for the surface semi-elliptical

cracks, located on outer surface of the baffle, where residual compression stresses are formed in the process of manufacture.

REFERENCES

1. Pištora, V., Švrček, M., Ferko, P., Mirzov, I. (2018). Fracture Mechanical Assessment of VVER Reactor Internals. *Proceedings of the ASME. 2018 10.1115/PVP2018-84589*
2. Oryniak, A.I. (2021) *Methods of calculation of stress intensity coefficient taking into account geometrical nonlinearity and arbitrary shape of crack*: Syn. of Thesis for Cand. of Tech. Sci. Degree, 05.02.09, Kyiv [in Ukrainian].
3. Makhnenko, O., Kandala, S., Basistyuk, N. (2021) Influence of the heat transfer coefficient on the level of residual stress after heat treatment of the VVER-1000 reactor baffle. *Mechanics and Advanced Technologies*, 5(2), 254–259. DOI: <https://doi.org/10.20535/2521-1943.2021.5.2.245074>
4. PM-T.0.03.333–15: *Standard program for assessing of technical condition and extension of service life of WWER-1000 internals*.
5. Makhnenko, O.V., Kandala, S.M., Savytska, O.M. (2021) Comparative analysis of models of irradiation-induced swelling for calculated determination of SSS of WWER-1000 baffle. *Problemy Mitsnosti*, 5, 13–22 [in Ukrainian].
6. (2013) *Guidelines for integrity and lifetime assessment of components and piping in WWER nuclear power plants (VERLIFE)*. Vienna: Int. At. Energy Agency.
7. Chirkov, A.Yu., Kharchenko, V.V. (2020) Special features of computational assessment of the change in shape of WWER-1000 reactor core baffle in view of irradiation-induced swelling. *Strength Mater.*, 52, 339–352.
8. PNAE G-7-002–86 (1989): *Norms for strength calculation of equipment and pipelines of nuclear power plants*. Moscow, Energoatomizdat [in Russian].
9. RD EO 1.1.2.05.0330–2012: *Guidelines for strength calculation of equipment and pipelines of RBMK, WWER and EPG reactor plants at the stage of service beyond the design life*.

ORCID

O.V. Makhnenko: 0000-0002-8583-0163,
S.M. Kandala: 0000-0002-2036-0498

CONFLICT OF INTEREST

The Authors declare no conflict of interest

CORRESPONDING AUTHOR

O.V. Makhnenko
E.O. Paton Electric Welding Institute of the NASU
11 Kazymyr Malevych Str., 03150, Kyiv, Ukraine.
E-mail: makhnenko@paton.kiev.ua

SUGGESTED CITATION

O.V. Makhnenko, S.M. Kandala (2022) Evaluation of brittle fracture resistance of WWER-1000 reactor baffle during long-term service, taking into account the residual technological stresses. *The Paton Welding J.*, 8, 46–54.

JOURNAL HOME PAGE

<https://pwj.com.ua/en>

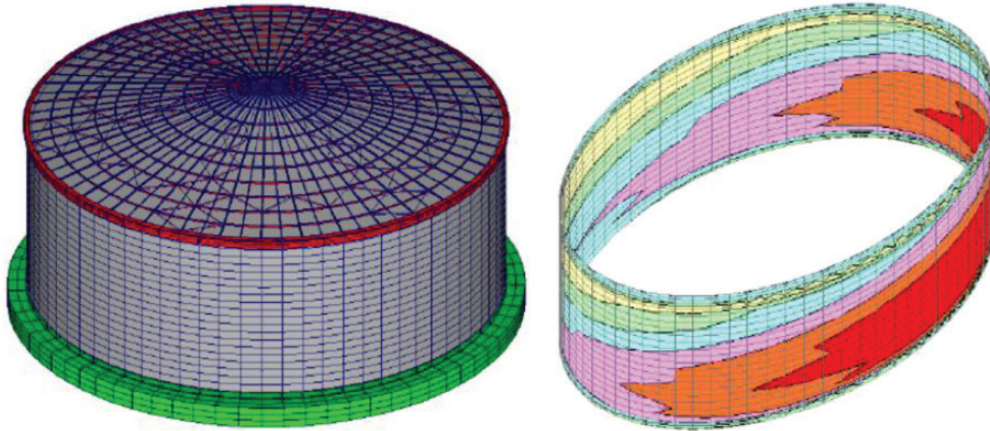
Received: 30.05.2022
Accepted: 17.10.2022

Design and repair of vertical cylindrical above ground welded steel tanks

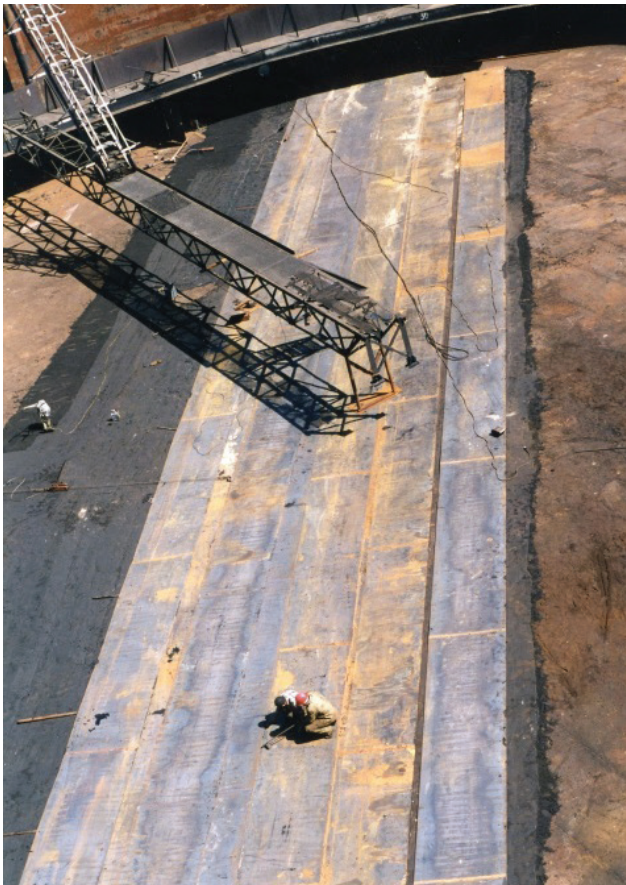
The E.O. Paton Electric Welding Institute of the NAS of Ukraine has worked for more than 74 years in the field of development of the technology of plant fabrication, erection and improvement of the design of vertical cylindrical steel tanks and renders the following services:

- development of design tanks documentation for storage of all kinds of fluids (crude oil, petroleum products, sunflower oil, sugar syrup, bagasse, etc.) in keeping with the requirements of EN 14015, API 650 standards;

Development of design documentation



Design of two cylindrical tanks with a conical roof in UBC-97.4 seismic zone, location class *D*, with volume $V = 10000 \text{ m}^3$, $D = 36.6 \text{ m}$, $H = 12.0 \text{ m}$ in keeping with API-650 requirements



Tank with volume $V = 50000 \text{ m}^3$ ($D = 60.7 \text{ m}$, $H = 18.0 \text{ m}$), replacement of the bottom and single deck of floating roof



Tank with volume $V = 10000 \text{ m}^3$ ($D = 34.2 \text{ m}$, $H = 12.0 \text{ m}$) for oil storage after repair



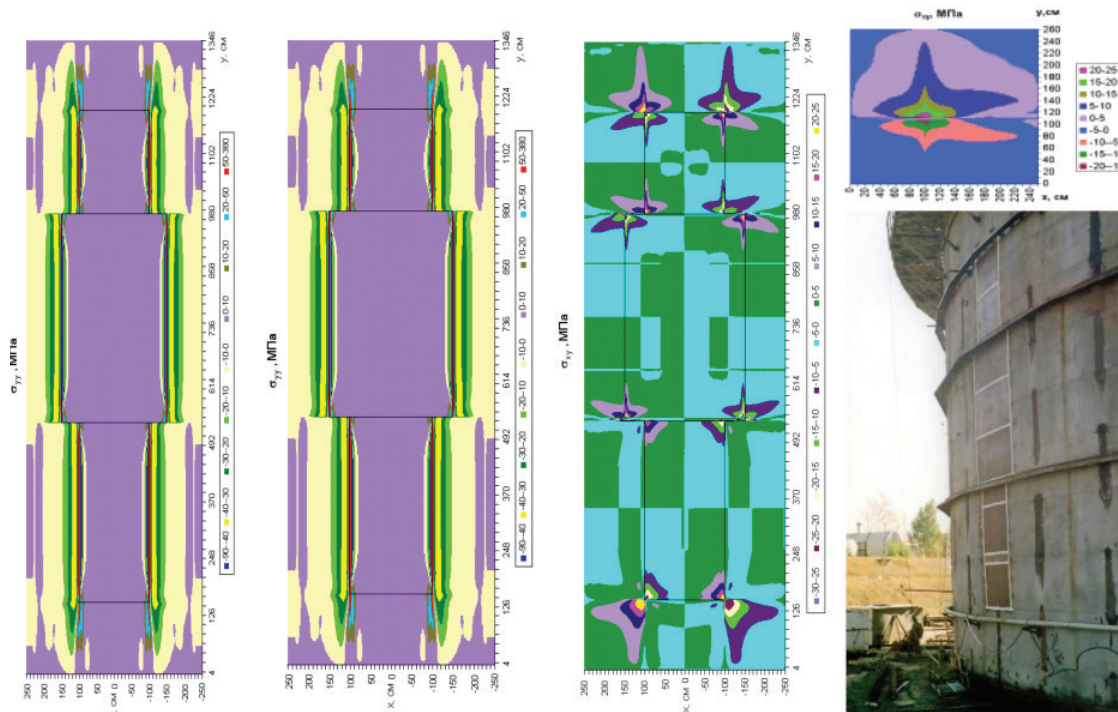
Repair of riveted tank with volume $V = 5000 \text{ m}^3$ built in 1895 year



Tank with volume $V = 50000 \text{ m}^3$ ($D = 60.7 \text{ m}$, $H = 20.0 \text{ m}$) with double shell: erection the double deck steel floating roof

Calculation of residual stress fields after welding individual sheets in the rigid contour

During welding-in of individual sheets the cylindrical shell lost its stability. Based on computer calculations a new technology of repair welding taking into account rigid contour at replacement of extended sections of the shell was developed to prevent the loss of its stability.



Tank with floating roof with volume $V = 50000 \text{ m}^3$, $D = 60.7 \text{ m}$, $H = 18.0 \text{ m}$ for crude oil storage: calculation of residual welding stresses in the presence a rigid contour for the shell at replacement of a section to the entire height of the tank at its repair.

- development of design documentation for tanks repair in keeping with the requirements of API 653 or national standards;
- determination of the causes for failures and accidents of tanks;
- welding engineering and supervision on site/fabrication.

Starting from 1994, inspection of more than 273 tanks from 1000 up to 50000 m³ volume has

been performed; 66 tanks of 5000 to 50000 m³ volume have been successfully repaired, based on the results of documentation development and author's supervision. During the last six years PWI experts designed six tanks of 50000 m³ volume with a double shell, double-bottom and doubledeck floating cover. The Institute has successful experience of tank design in regions with up to 0.4 g seismic activity.

Tank Design, Inspection & Repair
 E-mail: tanksweld@gmail.com
 Phone: +38(067) 502-75 54